

MULTIMODE INTERFERENCE BASED OPTICAL SENSORS  
FOR STRUCTURAL HEALTH MONITORING APPLICATION

NUR HOTIMAH BINTI YUSOF

DEPARTMENT OF CIVIL ENGINEERING  
FACULTY OF ENGINEERING  
UNIVERSITY OF MALAYA  
KUALA LUMPUR

2019

**MULTIMODE INTERFERENCE BASED OPTICAL  
SENSORS FOR STRUCTURAL HEALTH MONITORING  
APPLICATION**

**NUR HOTIMAH BINTI YUSOF**

**THESIS SUBMITTED IN FULFILMENT OF THE  
REQUIREMENTS FOR THE DEGREE OF DOCTOR  
OF PHILOSOPHY**

**DEPARTMENT OF CIVIL ENGINEERING  
FACULTY OF ENGINEERING  
UNIVERSITY OF MALAYA  
KUALA LUMPUR**

**2019**

UNIVERSITI MALAYA

ORIGINAL LITERARY WORK DECLARATION

Name of Candidate: Nur Hotimah binti Yusof

Registration/Matric No: KHA130025

Name of Degree: Doctor of Philosophy

Title of project Paper/Research Report/Dissertation/Thesis (“this work”):

“Multimode Interference Based Optical Sensor for Structural Health Monitoring Application”

Field of Study: Structural Engineering & Material

I do solemnly and sincerely declare that:

- (1) I am the sole author/writer of this Work;
- (2) This work is original
- (3) Any use of any work in which copyright exists was done by way of fair dealing and for permitted purposes and any excerpt or extract from, or reference to or reproduction of any copyright work has been disclosed expressly and sufficiently and the title of the Work and its authorship have been acknowledged in this Work;
- (4) I do not have any actual knowledge nor do I ought reasonably to know that the making of this work constitutes an infringement of any copyright work;
- (5) I hereby assign all and every rights in the copyright to this Work to the of University Malaya (“UM”), who henceforth shall be owner of the copyright in this Work and that any reproduction or use in any form by any means whatsoever is prohibited without the written consent of UM having been first had and obtained;
- (6) I am fully aware that if in the course of making this Work I have infringed any copyright whether intentionally or otherwise, I may be subject to legal action or any other action as may be determined by UM.

Candidate’s Signature

Date

Subscribed and solemnly declared before,

Witness’s Signature

Date

Name:

Designation:

## ABSTRACT

This research work focuses on developing new optical fiber sensing probes for structural health monitoring (SHM). Two types of optical sensor probes; microfiber and single mode-multimode-single mode fiber (SMS) structure were successfully fabricated using a flame brushing and fusion splicing, respectively. The non-adiabatic type of microfiber produced a periodic behavior at the output spectrum due to the oscillations as a result of back and forth coupling between core and cladding modes. On the other hand, the SMS structure generates a sufficient bandpass spectral response for a given wavelength range. Both non-adiabatic microfiber and SMS device are capable to be used to demonstrate both temperature and strain sensors. Temperature and strain sensors were successfully demonstrated using non-adiabatic microfiber and SMS structure as a probe. The proposed microfiber and SMS sensors were shown to be able to measure temperature stably up to 400°C with sensitivities of 6.0 pm/°C and 11.1 pm/°C, respectively. Both probes were also established for strain measurements. The strain sensitivities originate from the difference of the effective refractive index of the core and the cladding modes, which induces resonant wavelength shift against the strain. The strain sensitivity of the microfiber and SMS sensor was -1.36 nm/n and -2.06 nm/n with a linearity of more than 0.99 and 0.97, respectively. Both sensor designs are simple and thus they can be mass-produced with a relatively low cost. Finally, both microfiber and SMS sensor probes were successfully employed for measurements of compression strain in both steel and concrete beam structures. For instance, the microfiber sensor exhibits linear sensitivity of 0.0094 nm/kN for the compression strain measurement. The optical sensor was also able to detect the elastic limit of the steel beam by its significant change of the peak center wavelength. On the other hand, the SMS sensor exhibits linear sensitivity of 0.0323 nm/kN for the compression strain measurement.

The steel beam achieved its elastic mode limit at a compressive load of 130 kN, which agrees well with the conventional electrical resistance (ER) strain gauge measurement. The microfiber sensor was also successfully demonstrated for measuring compression strain and to the breaking point of a concrete beam. It exhibits linear sensitivity of 0.0454 nm/kN for the compression strain measurement. The concrete beam achieved its modulus of rupture limit at compressive load of 8.0 kN, which agrees well with the conventional ER strain gauge measurement.

**Keywords:** microfiber, non-adiabatic, strain, elastic limit, modulus of rupture

University of Malaya

## ABSTRAK

Kajian ini memberi tumpuan kepada membangunkan sensor peranti gentian optik baharu untuk pemantauan kesihatan struktur (SHM). Dua jenis peranti sensor optik; *microfiber* dan *single mode-multimode-single mode fiber (SMS)* telah berjaya direka cipta dengan menggunakan *flame brushing* dan *fusion splicing*. *Non-adiabatic microfiber* berupaya menjana spektrum keluaran berkala disebabkan oleh gandingan tindak balas selang-seli antara mod teras dan mod lajur. Manakala, sensor SMS menjana spektrum gelombang yang mencukupi untuk julat panjang gelombang tertentu. Kedua-dua peranti *non-adiabatic microfiber* dan peranti SMS boleh digunakan untuk mengukur suhu dan mengukur ketegangan. Sensor suhu dan sensor ketegangan telah berjaya dibuktikan dengan menggunakan gentian optik *microfiber non-adiabatic* dan peranti SMS. Sensor *microfiber* dan SMS yang dicadangkan berupaya mengukur suhu sehingga  $400\text{ }^{\circ}\text{C}$  dengan sensitiviti  $6.0\text{ pm}/^{\circ}\text{C}$  dan  $11.1\text{ pm}/^{\circ}\text{C}$ , masing-masing. Kedua-dua peranti juga diuji untuk pengukuran ketegangan rasuk. Sensitiviti ketegangan berasal dari perbezaan indeks biasan berkesan oleh mod teras dan mod lajur, yang mendorong berlakunya resonan antara panjang gelombang dan ketegangan. Sensitiviti ketegangan oleh sensor *microfiber* dan SMS adalah  $-1.36\text{ nm}/\text{n}$  dan  $-2.06\text{ nm}/\text{n}$  dengan graf garis lurus lebih daripada 0.99 dan 0.97, masing-masing. Reka bentuk kedua-dua sensor adalah mudah dan oleh itu ia boleh dihasilkan secara besar-besaran dengan kos yang rendah. Kemudian, kedua-dua sensor, *microfiber* dan SMS juga telah berjaya digunakan untuk mengukur tekanan mampatan dalam kedua-dua rasuk keluli dan rasuk konkrit. Sebagai contoh, sensor *microfiber* mempamerkan sensitiviti linear  $0.0094\text{ nm}/\text{kN}$  untuk pengukuran ketegangan mampatan. Sensor optik juga dapat mengesan *elastic limit* keluli dengan perubahan ketara pada pusat puncak panjang gelombang.

Sebaliknya, sensor SMS mempamerkan sensitiviti linear 0.0323 nm / kN untuk pengukuran ketegangan mampatan. Rasuk keluli mencapai had anjal pada 130 kN, yang selari dengan pengukuran *strain gauge* (ER) konvensional. Sensor *microfiber* juga telah berjaya mengukur tekanan mampatan sehingga rasuk konkrit gagal. Ia mempamerkan sensitiviti linear 0.0454 nm / kN untuk pengukuran ketegangan mampatan. Rasuk konkrit gagal pada 8.0 kN, yang selari dengan pengukuran *strain gauge* (ER) konvensional.

**Kata Kunci:** *microfiber, non-adiabatic, strain, elastic limit, modulus of rupture*

University of Malaya

## ACKNOWLEDGEMENT

I would like to say my deepest gratitude to the Almighty Allah S.W.T. for giving me good health and unexpected strength to complete this study. This thesis represents the dedicated efforts of numerous people, many of whom deserve special mention:

I would like to express my utmost thanks and deepest appreciation to my supervisor, Professor Ir. Dr. Sulaiman Wadi bin Harun and Professor Dr. Hashim Abdul Razak who has made this research journey a smooth passage. I am indeed very fortunate to have a very responsible supervisor to turn for suggestions, guidance, invaluable encouragement and support. Definitely this research broadened my experience and knowledge.

I would also like to express my gratitude to Photonic Engineering Laboratory team members, Structural Light Concrete Laboratory staffs and Structural Heavy Concrete Laboratory staffs for helping me out in experimental work, providing facilities and also for their guidance. Additionally, I would like to express my gratitude to my family and friends for their continuous support and kindly assistance in my research. Lastly, I offer my regards and blessings to all others who supported me in any other way during this study.

## TABLE OF CONTENTS

	Page
Title Page	i
Original Literary Work Declaration	ii
Abstract	iii
Abstrak	v
Acknowledgement	vii
Table of Contents	viii
List of Figures	x
List of Tables	xiv
List of Symbol and Abbreviations	xv
<b>Chapter 1 Introduction</b>	
1.1 Background of the study	1
1.2 Problem Statement	4
1.3 Objectives of the research	6
1.4 Thesis outline	6
<b>Chapter 2 Literature Review</b>	
2.1 Introduction	8
2.2 Structural Health Monitoring (SHM)	8
2.3 Fiber sensors	11
2.3.1 Fiber Bragg Grating	12
2.3.2 Microfiber	16
2.3.3 SMS sensors	18
2.4 Fabrication of optical microfiber and adiabatic criterion	23
2.5 Evanescent field	28
2.6 Summary	32
<b>Chapter 3 Fabrication and Characterization of Sensor Probes</b>	
3.1 Introduction	33
3.2 Fabrication of microfiber	35
3.3 Microfiber characteristics	38
3.4 Single mode multimode single mode fiber(SMS) based interferometer	45

3.4.1	Design and construction of the SMS structure	46
3.4.2	Characteristic of SMS	53
3.4.3	Simple load sensor using the SMS probe	57
3.5	Summary	65

#### **Chapter 4 High Temperature and Strain Measurements**

4.1	Introduction	66
4.2	High temperature sensor	67
4.3	Strain measurement	72
4.3.1	Strain measurement with non-adiabatic microfiber	76
4.3.2	Strain measurement with SMS sensor	79
4.3.3	Performance comparison	81
4.4	Summary	82

#### **Chapter 5 Steel Beam and Concrete Beam Compressive Strain Measurements**

5.1	Introduction	83
5.2	Optical non-adiabatic silica microfiber for steel beam compressive strain measurements	84
5.2.1	Experimental arrangement	85
5.2.2	Non-adiabatic silica microfiber sensor performance with steel beam	88
5.3	SMS sensor for steel beam compressive strain measurement	93
5.4	Optical non-adiabatic silica microfiber for concrete beam compressive strain measurement	98
5.4.1	Experimental arrangement for concrete beam strain measurement	99
5.4.2	Result and discussion	102
5.5	SMS sensor for concrete beam compressive strain measurement	107
5.6	Summary	109

#### **Chapter 6 Conclusion and Future Outlook**

6.1	Conclusion	111
6.2	Future Outlook	114

<b>References</b>		116
-------------------	--	-----

## LIST OF FIGURES

Figure 2.1	FBG structure showing an index modulation	13
Figure 2.2	Spectral response of FBG (Ma, Li, Mu, Jiang, & Luo, 2014)	13
Figure 2.3	Effect of strain on the FBG's spectral response	15
Figure 2.4	Schematic configuration of the SMS fiber structure	19
Figure 2.5	Light propagation within the MMF in SMS structure (Wang, Farrell, & Yan, 2008)	22
Figure 2.6	Schematic diagram of an optical silica microfiber	23
Figure 2.7	Schematic diagram of tapered fiber fabrication using flame-brushing method.	25
Figure 2.8	Schematic diagram of adiabatic transition region.(Gilberto Brambilla et al., 2009)	26
Figure 2.9	Modes progression in an optical microfiber	27
Figure 2.10	HE <sub>11</sub> mode intensity profile at different diameter microfiber (Talataisong et al., 2018).	28
Figure 2.11	The optical fiber cross-section profile along the long axis.	31
Figure 2.12	Schematic diagram of microfiber evanescent region.	31
Figure 3.1	Microfiber fabrication setup (a) schematic diagram (b) actual picture. Inset shows the size of the flame	36
Figure 3.2	Silica fiber (a) beforehand tapering and (b) afterward tapering	38
Figure 3.3	The fabricated adiabatic microfiber profile at transition region.	40
Figure 3.4	The output spectrum before and after tapering process when the ASE light was launched into the fiber/microfiber	41
Figure 3.5	Comparison of tapering angle between (a) adiabatic and (b) non-adiabatic microfiber	42

Figure 3.6	The bend and non-uniform tapering in the microfiber's transition region.	42
Figure 3.7	Non-adiabatic microfiber's transmission spectrum output.	43
Figure 3.8	Schematic diagram of the SMS fiber structure	47
Figure 3.9	Materials, tools and equipment used for construction of SMS structure probe (a) raw optical fiber (b) fiber stripper (c) alcohol for cleansing process (d) cleaver (e) Ericson FSU-975 fusion splicer.	48
Figure 3.10	The cleaving process procedure (a) cutting the optical fiber (b) stripping (c) cleaning (d) cleaving	49
Figure 3.11	Illustration of fiber cut with 90-degree flat-end.	49
Figure 3.12	Description of the Ericson FSU-975 fusion splicer.	51
Figure 3.13	Images of the splicing operation	52
Figure 3.14	Alignment of the fibers during splicing	53
Figure 3.15	Splicing defects	53
Figure 3.16	Refractive index profile for SMF and MMF structure	54
Figure 3.17	Output spectrum for SMS Fiber structure with different MMF length	56
Figure 3.18	Illustrative drawing of the recommended load sensor experimental arrangement. Inset displays the portrait of the SMSF structure.	58
Figure 3.19	The SMSF's spectral response at various vertical load at different length (a) L=1 cm, (b) L=3 cm, (c) L=5cm, (d) L=7cm, (e) L=9cm, and (f) L=11 cm.	60
Figure 3.20	Different load versus to the center crest wavelength of the impedance spectrum for variety L, (a) L=1 cm, (b) L=3 cm, (c) L=5cm, (d) L=7cm, (e) L=9cm, and (f) L=11 cm.	63
Figure 3.21	Impedance spectrum of the 3dB bandwidth versus the load volume for (a) L=5cm, (b) L=7cm, (c) L=9cm and (d) L=11cm	64
Figure 4.1	(a)The non-adiabatic microfiber sensor (b) The SMS fiber sensor structure.	68
Figure 4.2	Experimental setup for temperature measurement	69

Figure 4.3	Output spectra of the non-adiabatic microfiber at various hot plate temperatures	70
Figure 4.4	Output spectra of the SMS structure at various hot plate temperature.	71
Figure 4.5	Relationship of the interference spectrum output against the temperature for SMS fiber and non-adiabatic silica microfiber.	72
Figure 4.6	Strain measurement of the structure	73
Figure 4.7	Schematic diagram of the strain test	76
Figure 4.8	Spectral response output from the microfiber structure at different strain.	78
Figure 4.9	Central wavelength and displacement of microfiber against strain.	79
Figure 4.10	Spectral response output from the SMS fiber structure at different strain values.	80
Figure 4.11	Central wavelength and displacement of microfiber against	80
Figure 4.12	Wavelength interference spectrum relationship between non-adiabatic microfiber and SMS fiber against the strain.	82
Figure 5.1	Schematic diagram of the compressive test (a) Schematic illustration (b) Image (c) image of the steel beam after failure test.	88
Figure 5.2	Non-adiabatic silica microfiber bandpass output spectrum at 20kN compressive load.	89
Figure 5.3	Spectral response output from the non-adiabatic silica microfiber structure at different compressive load within a span of 3.5 nm. Inset shows the spectra within a larger span of 30 nm.	90
Figure 5.4	Compressive strain and peak center wavelength at different amount of compressive load.	91
Figure 5.5	Spectral wavelength shift with the compressive strain.	92
Figure 5.6	SMS bandpass output spectrum at 40 kN compressive load.	95

Figure 5.7	Transmission spectra at different compressive loads within a span of 14 nm. The inset shows the spectra within a larger span of 40 nm.	96
Figure 5.8	Compressive strain and transmission dip wavelength at different amount of compressive load.	97
Figure 5.9	Spectral wavelength shift with the compressive strain.	98
Figure 5.10	Schematic diagram of the compressive strain's testing setup (a) Schematic illustration (b) Image of laboratory setup (c) Left and right view of the crack comb of concrete beam at breaking point.	102
Figure 5.11	Non-adiabatic silica microfiber bandpass output spectrum at 0.5kN compressive load.	104
Figure 5.12	Spectral response output from the non-adiabatic silica microfiber structure at different compressive load within a span of 5.0 nm. Inset shows the spectra within a larger span of 40 nm.	105
Figure 5.13	Compressive strain and peak center wavelength at different amount of compressive load.	106
Figure 5.14	Spectral wavelength shift with the compressive strain.	107
Figure 5.15	Spectral response output from the SMS structure at different compressive loads	108

## LIST OF TABLES

Table 5.1	Comparison result between SMS and microfiber.	110
-----------	---	-----

University of Malaya

## LIST OF SYAMBOLS AND ABBREVIATIONS

ASE	:	Amplified Spontaneous Emission
CDMA	:	Code Division Multiple Access
DGM	:	Digital Ground Model
EMI	:	Electromagnetic Interference
EM	:	Electromagnetic
ER	:	Electrical Resistance
FBGs	:	Fiber Bragg Gratings
LVDT	:	Linear Variable Differential Transform
MMF	:	Multimode Fiber
$LP_{01}$ ,	:	Fundamental Mode
$LP_{02}$	:	Higher Mode
MMI	:	Multimode Interference
RI	:	Refractive Index
SDM	:	Spatial Division Multiplexing
SMS	:	Singlemode-Multimode-Singlemode
SMF	:	Single-mode Fiber
SPR	:	Surface Plasmon Resonance
TDM	:	Time Division Multiplexing
VBDD	:	Vibration-based Damage Detection
WDM	:	Wavelength Division Multiplexing

# CHAPTER 1

## INTRODUCTION

### 1.1 Background of the Study

In past several decades, optical fibers have been broadly assigned in optical communications due its capability to function as a transmission fiber of waveguide light. Beyond telecommunication, they can also be used to construct excellent sensors because of tons advantages inclusive of high sensitivity with insensitivity to electromagnetic (EM) interference and erosion-less (Xu, Kou, Luo, & Lu, 2012). Other than that, they also have an extraordinary characteristics such as multiplexing and remote sensing abilities, superior flexibility, lower propagating loss, economical manufacturing cost and small form factor (Lee et al., 2012). Furthermore, they can be used in explosive environment and hazardous places. Thus, optical fiber sensors can provide simultaneous sensing ability with high accuracy.

Up to date, countless optical fiber devices have been demonstrated to measure temperature, , displacement, strain, rotation, pressure, refractive index (RI), and others (Rivero, Goicoechea, & Arregui, 2018; Talataisong, Ismaeel, & Brambilla, 2018; Tong & Sumetsky, 2011; X. Wu & Tong, 2013; Kou et al., 2012; Brambilla.G, 2010; Gilberto Brambilla et al., 2009). The sensing abilities of the optical fibers can be considerably enhanced by utilizing innovative various optical technologies such as fiber interferometers, fiber gratings, nanorods, surface plasmon resonance (SPR), microfibers, Brillouin/Raman scattering, and others (Emami & Goodarzi, 2018; Kumar & Kumar, 2018; Ghasemi et al., 2017; Ascorbe, Corres, Arregui, & Matias, 2017; Ji et al., 2016; Di Sante, 2015).

Recently, optical fiber sensors are also deployed for real time deformation monitoring of aircrafts, bridges, constructions and ships (Chew et al., 2018; Soga & Luo, 2018; Bremer et al., 2016; Tennyson et al., 2000). One of the interesting applications of fiber sensors is for structural health monitoring (SHM). The development of fiber optic sensors for SHM has been assisted by the rapid growth of microtechnology in composite materials (Yazdizadeh, Marzouk, & Hadianfard, 2017), vast structural designing structures (Metje, Chapman, Rogers, Henderson, & Beth, 2008), and quantitative substance process (Chang & Mehta, 2009). In principle, SHM is the process of detecting the response of a structure under observation to detect anomalies, identify deterioration and recognize existing damage for further action (Lopez-higuera, Jose MiguelCobo, Incera, & Cobo, 2011; Glisic, Inaudi, & Casanova, 2010; Li, Li, & Song, 2004). To date, fiber Bragg gratings (FBGs) sensors were widely used for the SHM application (Torres, Payá-Zaforteza Ignacio, Calderón, & Adam, 2011). However, the construction of FBG sensors requires photosensitive fibers or hydrogen loading facility and a cumbersome fabrication setup (Gunawardena, 2016). It also involves working with hazardous gases and annealing treatment after fabrication. Furthermore, the grating gets destroyed as the temperature increases beyond 300°C (Gunawardena et al., 2016).

On the other hand, fiber inline interferometric sensors have gained attention in recent years due to their ease of fabrication, compactness, and high sensitivity for the measurement of various physical parameters such as temperature and strain. Recently, optical microfibers have been proposed and utilized in many sensing applications (Irawati et al., 2017; Sulaiman Wadi Harun et al., 2016; Tong, 2010 Gilberto Brambilla et al., 2009).

Besides adiabatic microfiber, a non-adiabatic type with an abrupt change in taper angle which promotes the coupling between the core modes and higher order modes is also useful for sensing application. Principally, the coupling arises between the un-tapered fiber's core mode and the first two modes of the microfiber waveguides ( $LP_{01}$ ,  $LP_{02}$ ). Similarly, microfiber will aid beyond than single mode because air and glass have huge refractive indices difference. In that account, the single-mode fiber is transformed to a multimode fiber once the light circulates inside the air-cladding interface of the microfiber's waist. Hence, transmission power versus a wavelength graph shown oscillation in the microfiber's spectral output in periodic behavior from the back and forth coupling activities between single mode fiber and the two or more modes of the tapered-fiber (Brambilla et al., 2009; Muhammad, Jasim, Ahmad, Arof, & Harun, 2013).

Another fiber inline interferometer based on a SMF-MMF-SMF (SMS) fiber structure can also be used for sensing as it generates a similar bandpass spectral response (Zhang et al., 2014). It was introduced for various sensing purposes (Frazao et al., 2011; Ian et al., 2017; Wang, Farrell, & Yan, 2008). For instance, Zhang et al. reported a theoretical and experimental results on refractive index (RI) sensing based on the multimode interference in SMS structure (Zhang et al., 2014). In another work, Wu et al. demonstrated the use of the SMS sensor for simultaneous measurement of displacement and temperature (Q. Wu et al., 2010). The SMS structure is simpler and relatively cheaper to be fabricated compared to the FBG.

In this thesis, both non-adiabatic microfiber and SMS structure probes are proposed and demonstrated for SHM application in monitoring temperature and strain. The microfiber and SMS devices are fabricated using a flame brushing technique and fusion splicing, respectively.

## 1.2 Problem Statement

The growth of technology today has made our lives easier and effortless with existence of tunnels, railways, roads, bridges, dams, high-rise buildings and nuclear power plants. These infrastructures become the most important asset of any country and thus they have normally long service life compared with other industrial products. Nevertheless, with time their structural health conditions become worsening and falling. The deterioration mostly is the result of overload, aging, decay process, construction error, lack of maintenance, environmental degradation and aggressive exposure conditions such as earthquakes or vehicle impact (Lopez-higuera, Jose MiguelCobo et al., 2011).

For instance, the recent collapses I-35 Bridge in Minneapolis in 2007 and De La Concorde Overpass in Quebec, Canada in 2006 have raised structural health monitoring (SHM) field (Mosavi Khandan Haghghi, 2010). The incident become strong motivation for SHM to evolve and grow rapidly (Chang & Mehta, 2009). Therefore, an accurate diagnostic structural health condition should be placed to ensure structural integrity and public safe is on guard (Aktan & Tsikos, 2000).

Recently, there is an increasing insistence for structural health monitoring enquiry. Malaysian government has invested a billion of ringgit every year to substantially enhance the current structure conditions. SHM can be deliberated as a promising technology for an excellent monitoring for various structures like building, bridges and airplanes (Brownjohn, Tjin, Tan, Tan, & Chakraboorty, 2004; Malekzadeh, Gul, Kwon, & Catbas, 2014; Sohn, Farrar, Hemez, & Czarnecki, 2004).

Initial stage in SHM are monitoring and collecting data regard the circumstances and characteristic of the structure. The valuable data is significant for structural justification and to make engineering decision. Hence, providing proper design and well-distributed devices network to generate data is crucial. On that account, it can be achieved by engaging advance accurate tools measurement devices containing an exceptional sensors and data acquisition systems such as optical sensors.

To be updated, various types of sensors have been used for SHM. The conventional methods of SHM are often impractical, as they required specialized operators and the measurements can be affected by the weather. The conventional sensors have suffered from major deficiencies including sensitivity to electrical noise and heavy cabling labor. Strain gauges are widely used in the conventional SHM system to measure and monitor the strain condition of the structure. The strain gauge detects an electrical signal and thus the sensor system requires huge numbers of an electrical wiring system and complicated data acquisition system.

Recently, optical fiber sensors have also gained interest among researchers for structural health condition enquiry in a long periodic of time application due to their immunity to electromagnetic interference, durability and stability (Chang & Mehta, 2009; Ferdinand, 2014). Most of the optical fiber monitoring systems are not invented to measure structure's displacement, nonetheless to gauge strain the structure.

For instance, FBGs can be attached to the civil structure for long-term strain and temperature monitoring (Perry et al., 2014). Though, FBGs suffers because of a narrow measurement range particularly for strain sensing application. Hence, FBGs structure desperately need an appropriate and new mechanical design or layout to enhance its dimension limitation and a sophisticated acquisition framework to accomplish a greater wavelength resolution (Zulkifli et al., 2016).

Similarly (Fernandez-Valdivielso, Matias, & Arregui, 2002) has demonstrated a FBG wavelength change within 1557.8 nm to 1560.87 nm as the strain is varied from 0  $\mu\epsilon$  to 5000  $\mu\epsilon$ . In this work, silica microfiber and SMS structure will be explored for both temperature and strain measurement for SHM application.

### **1.3 Objectives of the Research**

This study aims to propose a simple, affordable and feasible temperature and strain sensors for structural health monitoring purposes that established on optical approaches. The subsequent objectives are sketched out to navigate this research work to achieve its aim;

- i. To fabricate and characterize two types of optical sensor probes; microfiber and single mode-multimode-single mode fiber (SMS) structure.
- ii. To propose and demonstrate temperature and strain sensors using non-adiabatic microfiber and SMS structure as a probe.
- iii. To employ both non-adiabatic silica microfiber and SMS based on optical sensor for measurements of a compressive strain in both steel and concrete beam structures.

### **1.4 Thesis Outlines**

This thesis is made up of six chapters counting this introductory chapter. For Chapter 2, it discusses a literature review in which the recent progress on SHM, measurement method in SHM, fibre optic sensors and microfibers are presented.

Chapter 3 presents the fabrication and characterization of both microfiber and SMS sensor probes. The silica microfiber sensor is fabricated from a bare silica SMF by employing the flame brushing method while the SMSF structure is obtained by splicing a silica MMF between two silica SMFs. The non-adiabatic microfiber is used in this study since it produces a periodic behavior at the output spectrum due to the oscillations as a result of back and forth coupling between core and cladding modes. SMS structure also engender an adequate bandpass spectral response for a given wavelength spectrum subjected to multimode interference effect. The performance of the SMS based load sensor is also demonstrated in this chapter.

In Chapter 4, temperature and strain sensors are proposed and demonstrated using non-adiabatic microfiber and SMS structure as a probe. The temperature and strain change the effective refractive indices of the fundamental mode and the higher order modes, and thus tempt the resonant spectrum to shift based on the multimode interference effect.

In Chapter 5, non-adiabatic microfiber and SMS structures are proposed to measure compressive strain of both steel and concrete beams. Both techniques offer the advantages of a much simpler configuration, ease of fabrication, wide measurement range and high resolution compared to the conventional optical sensor based on fiber Bragg grating. Moreover, to validate the experimental data, parallel measurements are also made along the beam with an electrical resistance (ER) based strain gauge for comparison. As for Chapter 6, it summarizes and concludes the findings of this work. The future work is also being discussed in Chapter 6.

## CHAPTER 2

### LITERATURE REVIEW

#### 2.1 Introduction

This chapter deliberates some literatures relevant to structural health monitoring (SHM) and current growth in silica microfiber innovation along with the detail of its properties argument and also single mode-multimode-single mode fiber. Variety approaches to manufacture microfibers are discoursed in this section as well as flaming, drawing from bulk glass, and heating for fabrications of the tapered fiber. It then further discusses the applications of the microfiber. The following part delivers a brief view of microfiber-based sensors, the applications and also the functionalities.

#### 2.2 Structural Health Monitoring (SHM)

In recent decades, SHM has fascinated a huge researcher's devotion. This is attributed to the continuous deterioration of civil structure either beam, column, truss or any others member throughout the world (Glossop et al., 1990). For instance, long-length spans have alarmed a great number of specialists to the perils of overlooking legitimate checking of these civil structure. A considerable measure of these structures was being worked during the 1950s with just 40-to-50-year planned life expectancy. The sudden collapses of these structure and reach plastic limit condition without any warning cause growing awareness to implement for long-term structural health monitoring to observe the structural integrity, durability and reliability (H. N. Li, Li, & Song, 2004).

The SHM term can be described as the utilization of in-situ, endless or typical periodic evaluation and investigation to discover crucial structural and environmental constant during working phase condition purposely for earlier safety warning to the public to prevent disaster inclusive of bestowing maintenance and rehabilitation guidance (H.-N. Li, Yi, Ren, Li, & Huo, 2014; W. Housner et al., 1997). These characterizations emphasize on the significant of the SHM at earlier stage. SHM is as well characterized as following the reactions of a structure alongside data sources, if conceivable, over an adequately long term to identify anomalies, to recognize decay and to distinguish damage for decision making by (Aktan & Tsikos, 2000). Additionally, the precise working evaluation condition and the crucial responses of a structure are compulsory to have the capability to assess the signs of operational occurrences, anomalies as well as the deterioration indications that possibly will influence serviceability and reliability of a civil structure.

Farrar and Worden categorized the progression of executing a damage recognition approach that is designed for mechanical engineering, aerospace and civil infrastructure as a SHM (Farrar & Worden, 2007). Furthermore, damage is characterized as the material or geometrical structural changes, as well as the boundary conditions and connectivity mechanism changes, where consequently influence the performance of the structural in current situation or in future (Guemes, Fernandez-Lopez, Díaz-Maroto, Lozano, & Sierra-Perez, 2018). Essentially, SHM system consists of three key mechanisms: device mechanism, input system processing together with data acquirement system, transmission and storage, and also health assessment scheme that contain diagnostic theorem and data administration (H.-N. Li et al., 2014).

In detail SHM requires: alterations to an existing structure, evaluate the structural condition and performance affected by external work either in long-term or short term, specialist care during demolition, assessing the fatigue life, unique construction inspection mechanism and structural integrity of post-earthquake monitoring (Brownjohn, 2007; Mita, 1999). Hence, for that reason the sensors exploited in structural health monitoring are compulsory to screen not just the local changes material's properties nevertheless also significant environmental restriction, for example moisture, temperature and wind speed.

Many types of equipment and methodologies have been used to evaluate the structural condition or structural performance. For instance, Doebling et. al used accelerometers to estimate the structural mode shape and also the natural frequencies by utilized vibration-based damage detection (VBDD) method (S. W. Doebling C. R. Farrar M. B. Prime, 1998). Strain gauges were widely used in many SHM systems to evaluate load paths and recognize aging for structural components (O'Connell & Dexter, 2001). Despite all, the real load precision carried by particular members is exceptionally ambiguous because of the net residual pieces of the tremendously deteriorated members.

Linear variable differential transform (LDVT) was used to estimate displacement of the bridges and to get in-situ static displacement (Sung et al., 2016). The LVDT principle operation is to transform the displacement to an equivalent electrical sign (Pack, March, & Lvdt, 1997). Though, LVDT not suitable for in-situ work because the electric sign possibly will affect the electromagnetic interference (EMI), LVDT is compulsory to install with data loggers together with electrical power supply and wires, where may cause troublesomeness and additional cost for intensive care of huge structure.

Furthermore, the structural evaluation used on LVDT is established on acceleration output, which is an easy technique, cause it governs the displacement by just double integrating the acceleration output, thus, the biased initial conditions possibly will generate ambiguous outcomes (Jo, Lee, Jo, & Khan, 2018).

Land surveying is a technique to measure the position level in 3D positions of points which denoted in analogue features or digital form as contoured map or digital ground model(DGM) (W.Schofield & M.Breach, 2007). The bridges displacement can be determined by the elevation variation. Nevertheless, skilled surveyor is needed to conduct the field work manually. Furthermore, this method is not suitable to be used in measuring the displacement of dynamic bridges, because of the horizontal wind load and congestion traffic. Beyond all, every now and then to install a stationary reference for the evaluations is absurd. Not to mention, this technique requires a free sight from any barrier of more than two spot with known coordinates. Plus, the assessment is troubled by the surrounding atmospheric condition, for example storm, fog and rain.

In conclusion, the conventional methods of SHM are often impractical, as they required specialized operators and the measurements can be affected by weather. The conventional sensors have suffered from major deficiencies including sensitivity to electrical noise and heavy cabling labor, etc.

### **2.3 Fiber Sensors**

In the past few years, electrical sensor has been controlled and played important roles in sensor industry. Nonetheless, there are several features in which conventional sensors need significant improvements including bulky in size, sensitivity to electrical noise, a lot of cabling and erosion (Ye, Su, & Han, 2014).

Due to these deficiencies, many efforts have been devoted by scientists worldwide to enhance the devices. Therefore, today fiber optic sensors have grown tremendous interest to replace the conventional electrical based sensors. The endeavours for structural deficiency used fiber optic started at 1990, underneath the headline "structures with nerves of glass", by investigating the fiber optic's persistence and durability (Crane, Macander, & Gagorik, 1983). They have focal points, for example, light and little scale weight/size, invulnerability to electric noise (EMI), high sensitivity, and ease in signal light transmission. To date, impressive endeavours have been driven to investigation of fiber optic devices, and almost achieved perfection. In this section, three categories of optical fiber sensors are described.

### **2.3.1 Fiber Bragg Grating**

Fiber Bragg grating (FBG) is a reflective type of optical filter created in a small portion of optical fiber that mirrors certain wavelengths of light and conveys others completely. Fiber Bragg grating is made by laterally revealing the core of a photosensitive single-mode fiber (SMF) to an intense ultraviolet light through a phase mask or interferometer to form a periodic pattern. The exposure generates a last-lasting increment in the refractive indices of the core of the fiber, forming a rigid indices modulation corresponding to the exposure design. These rigid indices modulation is referred to a grating as presented in Figure 2.1.

A small light volume is reflected at every periodic refraction shift. Then these reflected signals integrate coherently at a particular wavelength under the Bragg condition. Alternate signs at wavelengths other than the Bragg wavelength, that not pair with the phase, consequently they are allowed to be transmitted through the core. Figure 2.2 shows the spectral response of FBG.

Underneath phase matching environments, the FBG couples the advancing circulating core mode toward the rear circulating core mode. A light signal manages to circulate through the FBG with insignificant loss or signal variation.

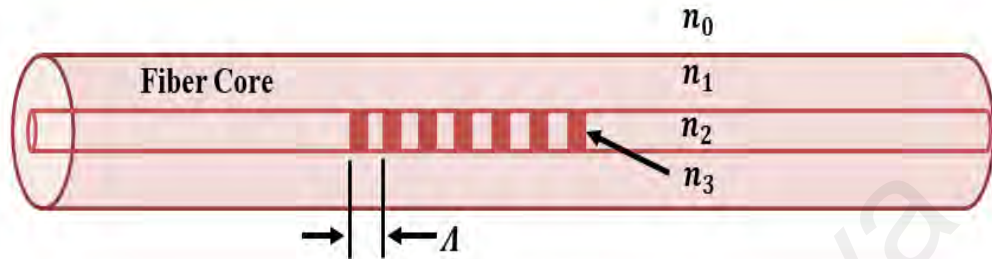


Figure 2.1: FBG structure showing an index modulation.

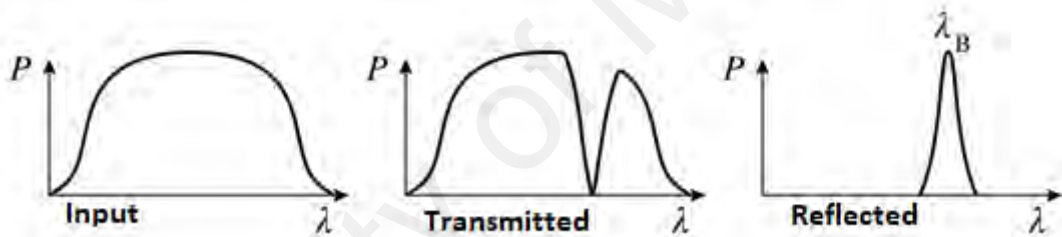


Figure 2.2: Spectral response of FBG (Ma, Li, Mu, Jiang, & Luo, 2014).

In a FBG the Bragg wavelength  $\lambda_B$ , or the light wavelength reflected, is shown as follow (Othonos & Kalli, 1999)

$$\lambda_B = 2n_{eff} \Lambda \quad (2.1)$$

And that  $n_{eff}$  is the fiber's core effective refractive index while  $\Lambda$  is the grating period. Equation (2.1) indicates that the Bragg wavelength can be reformed by varying the grating period or the effective refractive index. It is just that those wavelengths that achieve the Bragg condition are influenced and powerfully back-reflected.

The capacity to precisely pre-set and keep up the grating wavelength is an essential component and preferred standpoint of FBGs.

Due to the temperature and strain necessity of the effective refractive indices and grating phase, the wavelength of the reflected element will also shift as function of temperature and strain. Thus, temperature or strain can be determined from the reflected FBG wavelength. Figure 2.3 illustrates the effect of strain on the spectral response of FBG. The Bragg wavelength output usually changes to strain around  $1.2 \text{ pm}/\mu\epsilon$  at 1550 nm (Venkatesan & Ramalingam, 2017). It is a comparative theory, on the occasion that, 1m long fiber is elongated by  $1 \mu\text{m}$ , the strain is  $1 \mu\text{m}/1 \text{ m} = 1 \mu\epsilon$ . The temperature variation changes the effective refractive index. However, the grating time frame can likewise be altered with thermal variation, nonetheless about the impact at room temperature on refractive indices is one order of magnitude higher than the temperature expansion or contraction. The temperature output normally is approximate to  $3 \text{ pm}/^\circ\text{C}$  at 1550 nm region. To further, FBGs characteristic of the wavelength-encoded measure and information is an exceptional properties and advantage. Further, this wavelength-encoded uniqueness attempts robustness to noise or power fluctuation and permit wavelength division multiplexing (WDM) action beyond to the typical fiber devices. On that account, multi-point sensors can be appreciated consuming this method. Occasionally, WDM is joined with spatial division multiplexing (SDM), time division multiplexing (TDM) and code division multiple access (CDMA) methods.

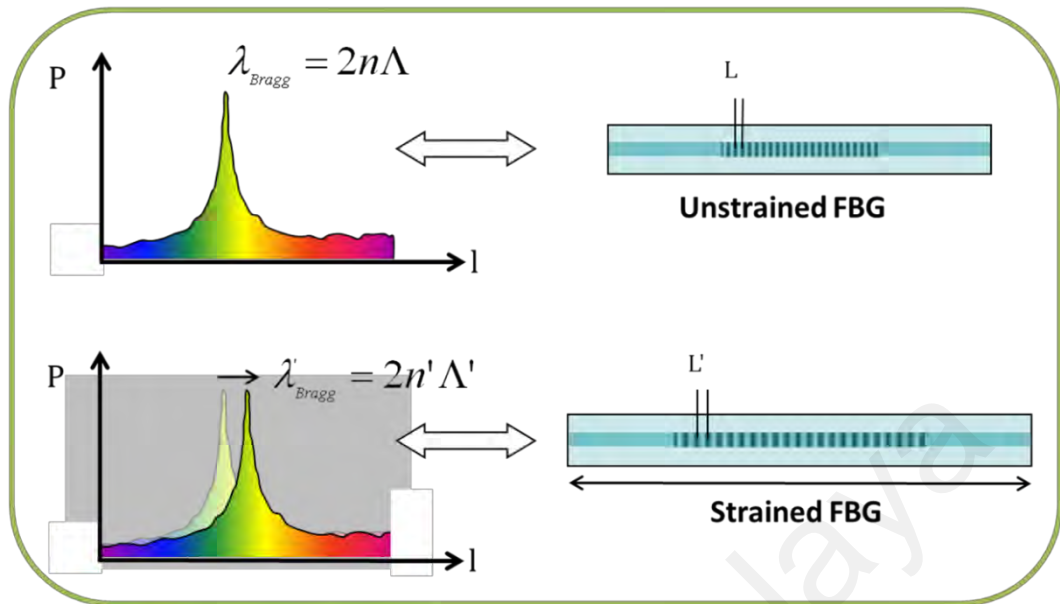


**Figure 2.3: Effect of strain on the FBG's spectral response.**

(<https://www.fbgs.com/technology/fbg-principle/>)

FBG sensors have been used and verified in countless disciplines like dams, bridges, mines, composite laminates, generators, airplanes, railway systems, ship waterjets and geotechnical areas (Childers et al., 2001; Deng & Cai, 2007; Di Sante, 2015; Ferdinand, 2014; Ko & Ni, 2005; Sohn, Farrar, Hemez, & Czarnecki, 2004; Willsch, Ecke, & Bartelt, 2002). Several FBG devices have been used and applied in industrial field and commercialized such as in structural health monitoring area (Udd et al., 2002) and oil/gas reservoir monitoring (Gysling & Bostick, 2002). For instance, CiDRA's FBG pressure or temperature device was disclosed exceptional functionality at 150 °C, 5000 psi for over two years with output drift within 0.015% full scale/year (Gysling & Bostick, 2002). Others than that, this sensors also have been installed in oil/gas wells for in a 15,000-feet downhole(Gysling & Bostick, 2002).

### 2.3.2 Microfiber

Optical microfibers with diameters on the order of few micrometer or less have attracted much attention during the last few years (Belal, Song, Jung, Brambilla, & Newson, 2010; Gilberto Brambilla et al., 2009; Guan, Li, Jin, & Ran, 2013; Rivero, Goicoechea, & Arregui, 2018; Xu, Lu, Chen, & Bao, 2017). This is accredited to their exceptional optical properties such as strong evanescent field. Evanescent field refers to the portion of light guided by the microfiber but propagating in the surrounding medium. Around 50% of power guided inside the microfiber circulates outside the physical boundary of the waveguide due to its small cross-section. This field can be accessed rather easily for sensing applications because of the strong spatial confinement. Microfibers also named by different researchers' group as an optical fibre microwires, subwavelength-diameter wires, nanofiber, ultrathin optical fiber, nanotaper, photonic microwires, nanowire, or fiber taper. It is defined as a circular waveguide with diameter nearest to or narrower than the carried light wavelength (Tong, 2010).

Optical microfibers have applications in many areas including spectroscopy (Degrandpre & Burgess, 1990; Mignani, Falciai, & Ciaccheri, 1998; O'Keeffe, Fitzpatrick, & Lewis, 2007), non-linear optics like generation of higher harmonics (Coillet & Grellu, 2012) or the use of microfibers as interferometers in which the two paths are represented by two transverse fiber modes (Liu, Zhao, Floreani, Zhang, & Bennion, 2002; Tan, Sun, Jin, Li, & Guan, 2013). The microfiber can also be used to create optical traps for ultra-cold atoms with the help of a standing light wave inside the microfiber (Das et al., 2010). For all the different applications mentioned here, the microfiber must have suitable properties in terms of geometry and eventually the light guidance.

Silica microfiber was fabricated using top-down techniques like fiber pulling (Gilberto Brambilla, Finazzi, & Richardson, 2004; G.Brambilla, F.Xu, & X.Feng, 2006; Tong et al., 2003) or direct draw from bulk materials (Tong et al., 2006). Silica nanowires, on the other hand, have previously been formed via a variety of method such as an electron beam lithography (Chen, Reed, Rawlett, & Tour, 1999), laser ablation (Morales & Lieber, 1998), template-based methods (Lakshmi, Patrissi, & Martin, 1997), bottom-up methods such as vapor–liquid– solid techniques (Westwater, 1997), chemical and physical vapor deposition (Zhang, Zhang, Li, Wang, & Zhu, 2000) , sol-gel methods (Miao et al., 2002) The overwhelming device properties such as superlative sensitivity, fast response, small power consumption and superior spatial resolution, which can be utilized to manufacture economical optical sensor, scaled down and all-fiber grounded optical sensors for different purpose (Birks & Li, 1992). For example, a great numbers of research endeavors have concentrated on the improvement of microfiber that establishing optical resonators which may fill in as optical channels that consist numerous promising employments in optical correspondence and devices.

Formerly, numerous microfiber sensors have been stated including coil resonators and microfiber loop or knot or coil, recent the device classified by the function such as biconical tapers, optical grating, coupler silica microfiber sensor, circular cavities, Mach-Zehnder interferometers and functionally coated/doped microfibers (Talataisong, Ismaeel, & Brambilla, 2018). These sensors are extremely delicate to an adjustment in the encompassing refractive list because of the evanescent region that spreads exterior the microfiber, because of that they manage to discover numerous appliances in different optical sensors. The nonlinear properties of the miniaturized scale transmitted into the silica optical fiber can likewise be utilized in fiber laser exploitations (Lim, Harun, Arof, & Ahmad, 2012).

### 2.3.3 SMS Sensors

The multimode interference (MMI) effect has been widely explored for various applications especially in developing various optical components such as combiner, beam splitters, and multiplexers for optical communications (Paiam & Macdonald, 1997; Rahman, Somasiri, Themistos, & Grattan, 2001; Soldano & Pennings, 1995). The multimode interference experiencing in a single-mode–multimode–single-mode (SMS) fiber structure has also been employed to develop novel optical devices like sensors or filters (Mehta, Mohammed, & Johnson, 2003; Mohammed, Mehta, & Johnson, 2004a; Mohammed, Smith, & Gu, 2006; Wang & Farrell, 2006a, 2006b). This optical device based on an SMS fiber structure attempts a whole-fiber resolution for optical communication and optical sensing with the favours of simple of packaging and connection to optical fiber mechanism. In short, they are advantageous due to high compactness, low cost, broad wavelength spectrum and ease construction.

The SMSF structure is diagrammatically illustrated in Figure 2.4. The multimode fiber (MMF) segment consumes a step-index profile. The single-mode fiber (SMF) and MMF are regulated over the similar axis so that there is no offset among SMF and MMF at the two intersections. However, there is typically a mismatch of the refractive indices between the SMF and MMF that may motivate a reflection at the intersection. Right after the light was coupled from the SMF into the MMF, the higher order modes are energized in the MMF and impedance between various modes arises. The relation between the longitudinal propagation coefficients for the  $m$  and  $n$  order mode may reported (Gong, Zhao, Rao, & Wu, 2011; Yong Zhao, Li, Meng, & Zhao, 2014):

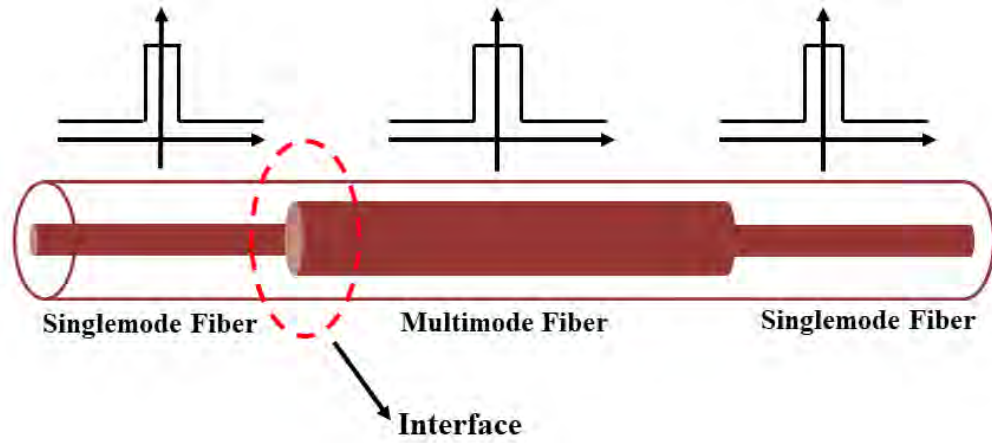


Figure 2.4: Schematic configuration of the SMS fiber structure.

$$\beta_m - \beta_n = \frac{u_m^2 - u_n^2}{2k_0 a^2 n_{core}} \quad (2.2)$$

Where  $\beta_m$  and  $\beta_n$  are the longitudinal propagation constant for m and n order mode.

And

$$k_0 = 2\pi/\lambda \quad (2.3)$$

where  $\lambda$  is the operating wavelength,  $a$  is the MMF's core radius,  $n_{core}$  is the core MMF's refractive indices,  $u_m$  and  $u_n$  are the normalized propagation coefficients:  $u_m = \pi(m - 1/4)$  and  $u_n = \pi(n - 1/4)$ .

After the phase variance of two modes at the integer of multiple  $2\pi$ , impedance between these both modes arise once,

$$(\beta_m - \beta_n)L = 2N\pi \quad (2.4)$$

where  $L$  is the MMF's length, and  $N$  is a natural number. The constructive interference wavelength may acquire;

$$\lambda = \frac{8(2N + 1)n_{core}a^2}{(m - n)[2(m + n) - 1]L} \quad (2.5)$$

As soon as the MMF is strained, the refractive index profile shifted due to the photo-elastic consequence and the crest of interference pattern will switch, hence

$$\Delta\lambda = \lambda_N - \lambda_{N-1} = \frac{16n_{core}a^2}{(m - n)[2(m + n) - 1]L} \quad (2.6)$$

Where  $\Delta\lambda$  is the wavelength difference of adjacent extreme. and the response of light intensity will shift as needed because the deformation of the MMF will prompt to the power loss of the considerable number of modes as the higher-order modes encounter bigger power loss compare to the lower-order (Dong, Wei, Zhou, Liu, & Lit, 2009; Yong Zhao et al., 2014).

Because of the circular symmetric properties of SMF core mode, the input light  $E(r, 0)$  is presumed to have a circular symmetric region dispersal. The minute the light is projected inside the multimode fiber, the input region can be disintegrated by the eigenmodes ( $LP_{nm}$ ) of the multimode fiber. Due to perfect configuration presumed, solitary the modes  $LP_{0m}$  can be thrilled (Mohammed, Mehta, & Johnson, 2004b; Yu Zhao, Jin, Liang, & Dong, 2011).

The profile of  $LP_{0m}$  is denoted as  $F_m(r)$  while the eigenmodes of the MMF are normalized as  $\int_0^\infty |E(r, 0)|^2 r dr = \int_0^\infty |F_m(r)|^2 r dr, (m = 1, 2 \dots)$ . As the small amount of the radiation from MMF is neglected, the input light is given as;

$$E(r, 0) = \sum_{m=1}^M c_m F_m(r) \quad (2.7)$$

where  $c_m$  is the excitation constant of every mode. This coefficient can be estimated by the overlap integral among  $E(r, 0)$  and  $F_m(r)$ .

$$c_m = \frac{\int_0^\infty E(r, 0) F_m(r) r dr}{\int_0^\infty F_m(r) F_m(r) r dr} \quad (2.8)$$

The enthusiastic mode number of the  $LP_{0m}$  of a MMF is estimated as  $M \cong V/\pi(V = \left\{\frac{2\pi}{\lambda}\right\} a \sqrt{n_{co}^2 - n_{cl}^2})$ , where  $a$  is the MMF's radius,  $n_{co}$  and  $n_{cl}$  are the core and cladding MMF refractive indices correspondingly and  $\lambda$  is the free area of wavelength.

As per light transmits inside MMF, the propagating light region at the spacing  $z$  will be estimated as (Mohammed et al., 2004a, 2006; Soldano & Pennings, 1995)

$$E(r, z) = \sum_{m=1}^M c_m F_m(r) \exp(i\beta_m z) \quad (2.9)$$

Figure 2.5 shows the amplitude of the calculated light region propagating at wavelength of 1550 nm along the MMF as presented by reference (Paiani & Macdonald, 1997). In the numerical calculation, the MMF and SMF used to have a core diameter of 105  $\mu\text{m}$  and 9  $\mu\text{m}$ , correspondingly. As shown in Figure 2.5, the light field circulates and unites during proliferating along the MMF, and it is reimaged within the range of about 4.5 cm of the propagation distance. It is also showed in Figure 2.5 that various circulation distances resemble to different region profiles at the cross-section. Therefore, coupling coefficient to the output of SMF depends on the MMF dimension.

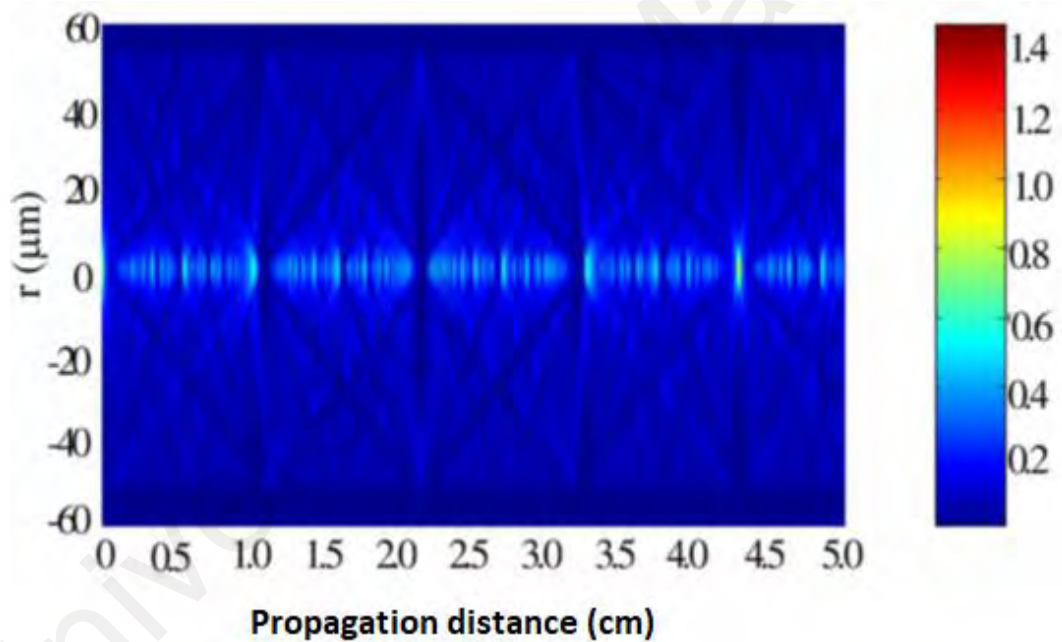
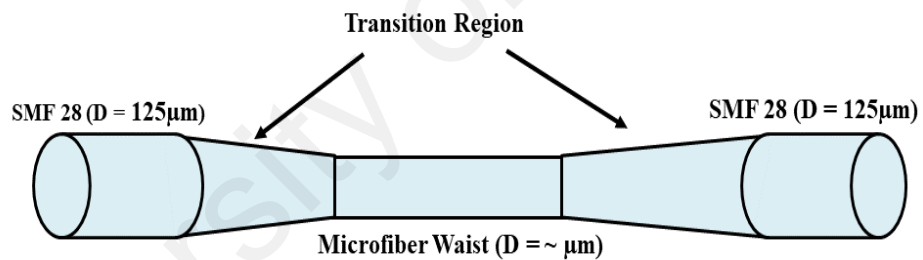


Figure 2.5: Light circulation inside the MMF in SMS structure (Wang, Farrell, & Yan, 2008).

## 2.4 Fabrication of Optical Silica Microfiber and Adiabatic Criterion

Optical silica microfiber is normally made by using heating and pulling process to convert an ordinary optical fiber to micro or nanoscale size (Gilberto Brambilla et al., 2004). Figure 2.6 shows the basic structure of an optical microfiber, which consists of a thin uniform waist in between two transition regions (Gilberto Brambilla, 2010). Light field from a SMF can be transmitted through the microfiber device with small losses (Gilberto Brambilla et al., 2009). Huge waveguide dispersion, rapid reaction time, high fraction evanescent area, tiny mode area, minimization and custom-made modular zone are essential properties for microfibers to be utilized effectively in sensing field (Black, Lacroix, Gonthier, & Love, 1991). An extensive number of literatures have been reported on applications of microfiber in various areas (Talataisong et al., 2018).



**Figure 2.6: Schematic diagram of an optical silica microfiber.**

Recently, at least four important techniques have been used in fabricating optical glass microfiber; the ‘self-modulated taper-drawing’ (Tong, Lou, Ye, Svacha, & Mazur, 2005), the flame-brushing technique (Tong et al., 2005), the modified flame-brushing technique (Gilberto Brambilla et al., 2009) and direct drawing from the bulk (Tong et al., 2005). The flame brushing method uses a flame to soften the optical fiber together with a mechanical setup for stretching the fiber (Ji et al., 2016). The flame-brushing modified a type of approach that employs an alternate heat resource instead of flame.

There are two kinds of heat resource that have been utilized, such as, a sapphire capillary tube heated by a CO<sub>2</sub> laser beam (Sumetsky, 2004), and a microheater (G. Brambilla, Koizumi, Feng, Richardson, & A, 2005). This method can also be utilized to other glasses including lead silicates (G. Brambilla et al., 2005), bismuth silicate (G. Brambilla et al., 2005), and chalcogenides (Yeom et al., 2008).

The flame-brushing technique (Bilodeau, Hill, Faucher, & Johnson, 1988) was initially established to fabricate fiber couplers and tapering a fiber tip. This technique has a high adaptability in monitoring the flame size, fiber pulling dimension and speediness (Lim et al., 2012). Figure 2.7 shows a typical setup for the flame brushing technique.

As shown in the figure, this approach uses a small flame, which is moving along a small section of a fiber while it is being stretching. Prior fabrication, the coating of the SMF is removed before it is placed at the transition stage. The fiber is held by two fiber holders. While it is being pulled, the flame moves and heats the uncoated length of the fiber. The flame can be acquired from a gas burner, which the gas being blended with oxygen to generate a flame without pollutant. The moving flame gives an even fire to the fiber and the fiber is tapered with great consistency across the heated area. To observe the microfiber propagation spectral output, a broadband light from an ASE source is projected inside microfiber fiber sensor via the SMF input while the opposite end of the SMF is associated to an optical range analyzer (OSA). By precisely controlling the pulling and flame condition, high quality microfiber can be fabricated.

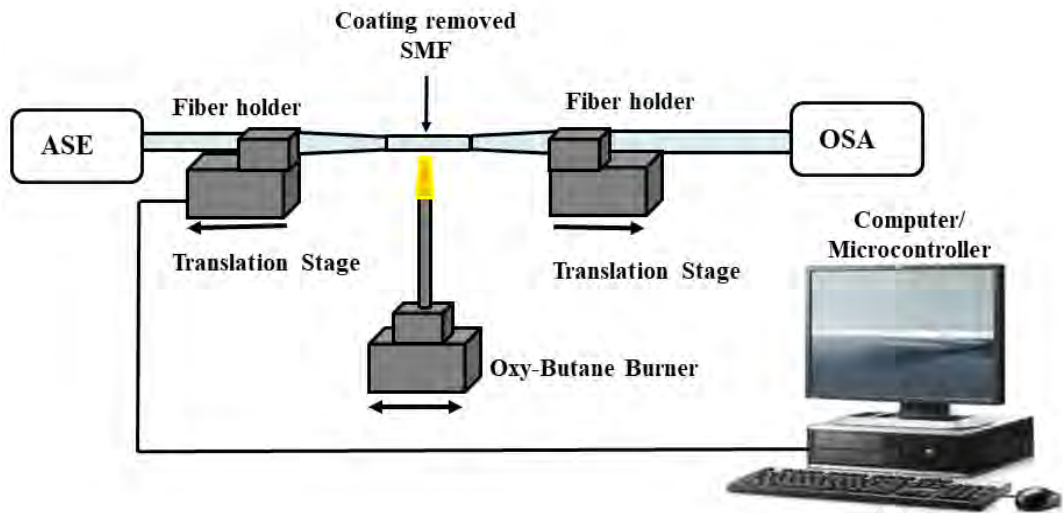


**Figure 2.7. Schematic diagram of microfiber fabrication setup using flame-brushing method.**

Adiabaticity is one of the essential conditions to manufacture superiority optical microfiber. This microfiber can be classified into two types; adiabatic and non-adiabatic. In adiabatic case, as guided light propagates along the fiber, the power stays in the fundamental mode and does not converted to the high-order modes as shown in Figure 2.8. For this situation, the adjustment in the transition region (decrease span) must be exceptionally slow. The adiabatic microfiber was used to transfer light in the demonstration of surface plasmon based on refractive index sensor (Yadav, Narayanaswamy, Abu Bakar, Kamil, & Mahdi, 2014).

On the other hand, some portion of power from higher order modes that continues circulating inside the microfiber may reintegrate and impede with core mode. This circumstance can be viewed as impedance between core mode  $HE_{11}$  and its nearest higher order mode  $HE_{12}$ . This consequences to a propagation spectrum with interference fringes with higher insertion loss. This type of microfiber is referred to non-adiabatic microfiber. Several studies propose that the coupling from core mode to the higher order modes can be diminished by enhancing the tapers pattern.

In real case, adiabaticity can be effortlessly attained by consuming adequately slow dimension of decreasing rate when manufacturing microfibers. It is meaning to fabricate microfibers with adequate long taper transition dimension (Lim et al., 2012).

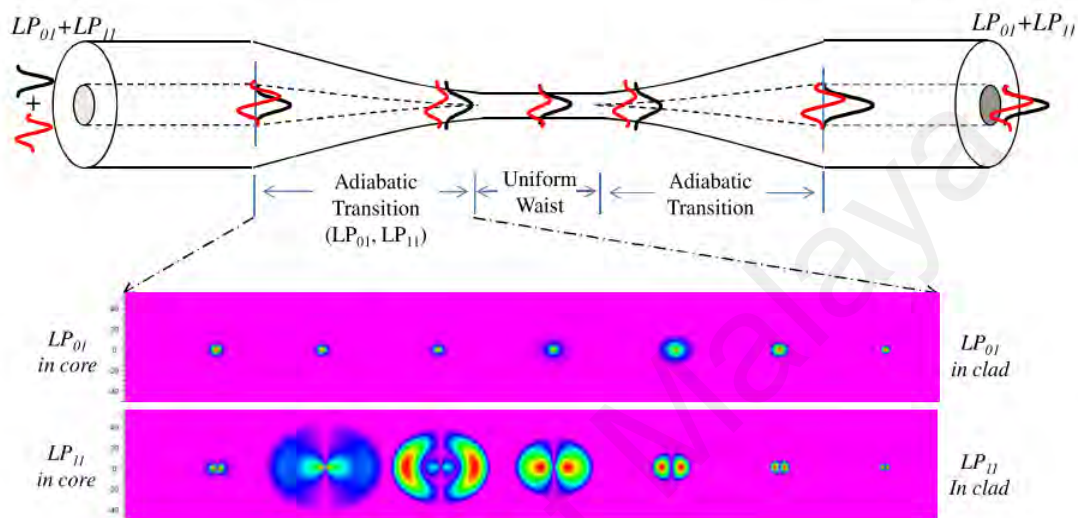


**Figure 2.8. Schematic diagram of adiabatic transition region.(Gilberto Brambilla et al., 2009).**

Utilization of microfiber can be organized into three by their essential property; transient field, confinement and transition regions. Figure 2.9 demonstrates the progression mode along the transition region of the microfiber. Though in un-tapered fiber at position **(1)**, the light modes are bounded by the fundamental intersection, at position **(2)** in the diminishing area, the light is at first engaged in the diminishing size center until the center direction winds up powerless. At position **(3)**, the mode is extended before it is navigated by the cladding or air interface. At position **(4)**, the mode is at the point that bounded by the cladding or air intersection and uncovers the greatest confinement, which causes this fascinating region intriguing for nonlinear exploitations.

For narrow breadths at position (5), the greater part of the light spreads at evanescent of exterior area of the air or silica intersection. This locale area is especially imperative for detecting applications as it permits most extreme collaboration with the encircling.

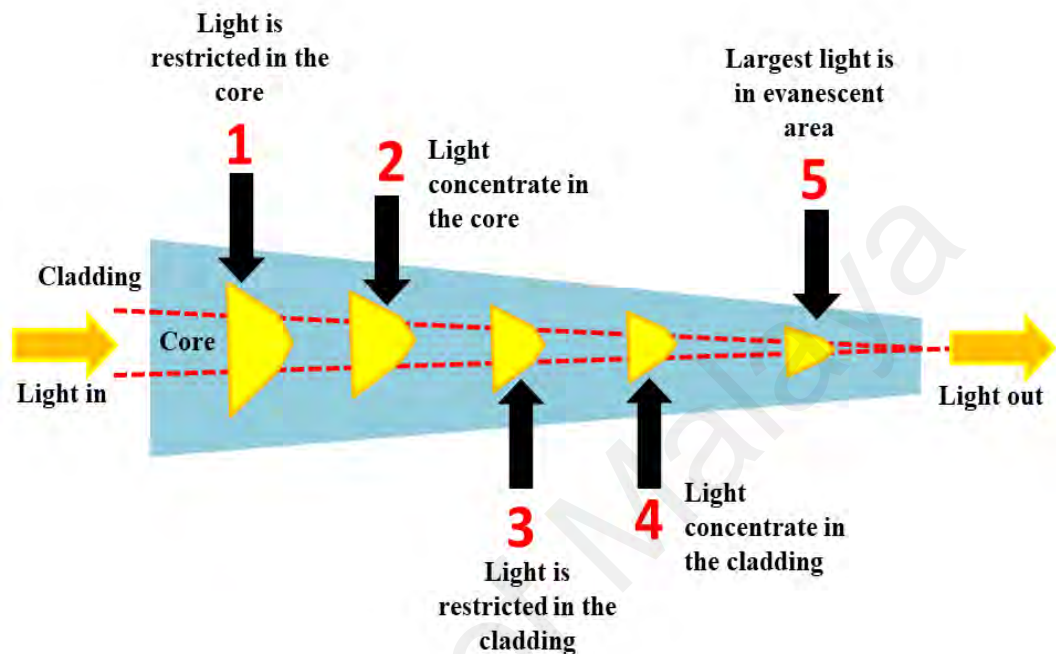


**Figure 2.9: Modes progression in an optical microfiber.**

In summary, microfiber with small optical loss, exceptional mechanical flexibility, tight optical confinement and huge evanescent field makes the optical microfiber device competent in numerous fields (Xu et al., 2017). The execution of the microfiber in detecting depends on changing of microfiber transmission qualities which subjected to the geometrical properties and also the adjoining condition coupling to the evanescent field. A standout amongst the most intriguing microfiber characteristic is the tailorability of its propagation to the requisite applications. It is conceivable to upgrade the device affectability, location farthest point and dynamic range by essentially enhance the microfiber.

## 2.5 Evanescent Field

Evanescent field is the partial power transmission farther the microfiber as shown in Figure 2.10. It is a vital characteristic for sensing devices because of the powerful interaction between the propagating light and the surrounding. As the microfiber breadth diminishing, the governing evolves into powerless and the mode extends till it is restricted by the cladding or air intersection. The greater evanescent field propagating at the microfiber inner cladding, the larger the delicate of the microfiber interacts with the environment. Microfiber devices are frequently covered with functionalizing materials that have the essential advantages for particular sensing exploitations. For instance, bio-identifiers can be coated onto microfiber for developing biosensors.

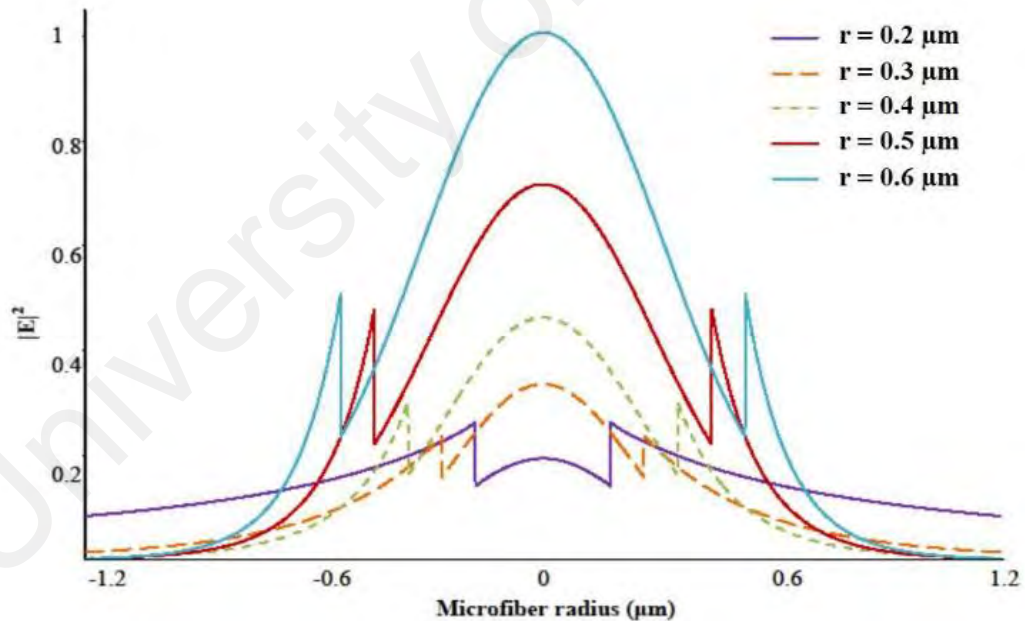


**Figure 2.10: HE<sub>11</sub> mode intensity profile at different diameter microfiber (Talataisong et al., 2018).**

Fundamentally, the silica optical fiber comprises a cylindrical core and a surrounding cladding. Normally, light propagate inside an optical fiber based on the total internal reflection (TIR), which is realized by designing the fundamental refractive indices to be slightly larger compare to the cladding refractive index (Leung, Shankar, & Mutharasan, 2007). The mode size is decisively reliant on the microfiber radius as shown in the following equation (Love, 1987):

$$v = \frac{2\pi \varphi}{\lambda} \frac{NA}{2} \quad (2.10)$$

which NA is the numerical aperture,  $\lambda$  is the wavelength, and  $\varphi$  diameter of the fiber.

Therefore, the light travelling along the optical fiber can be classified into two sections, which is the guided field in the core and the other one is an exponentially decaying evanescent field in the cladding. For a standard diameter fiber, the evanescent area deteriorates to just about nil inside the cladding. Hence, light transmission in standard diameter cladded optical fiber unable to communicate with the surrounding environment. Before optical fiber is utilized in sensing application, it was initially proposed for light engendering with low-loss only. The approach to accomplish the interaction between optical fiber and surrounding is to reveal the evanescent region of the propagated light. For instance, if the fiber cladding is detached, the evanescent region will communicate with the environment. Others than disclosures of the evanescent region to the around, tapering also escalate the evanescent region volume and penetration depth. Tapering is demonstrated to develop the optical fiber capacity as a sensor (Belal et al., 2010)(Clohessy, Healy, Murphy, & Hussey, 2005)(Tong & Sumetsky, 2011).

There is two method to taper the fiber; either eliminate the cladding and then taper the core, or preserve the core and also the cladding then taper the whole fiber (Leung et al., 2007). The length of the evanescent field from the core to the cladding interface is defined by the penetration depth as (Dybko, 2006):

$$E(x) = E_0 \exp\left(\frac{-x}{d_p}\right) \quad (2.11)$$

which  $x$  denotes as the length from the core fiber, beginning at  $x = 0$  at the core to cladding intersection,  $E_0$  is the value of the interface field, and  $d_p$  is the penetration depth described as (Dybko, 2006):

$$d_p = \frac{\lambda}{2\pi\sqrt{n_{co}^2 \sin^2\theta - n_{cl}^2}} \quad (2.12)$$

which  $\lambda$  defined as the light source wavelength,  $\theta$  is the light incidence angle inside the core to cladding feature,  $n_{co}$  and  $n_{cl}$  are the core and cladding refractive index as shows in Figure 2.11. Meanwhile, evanescent area for microfiber is shows in Figure 2.12. The figure also shown the light transmission and the area evanescent occur.

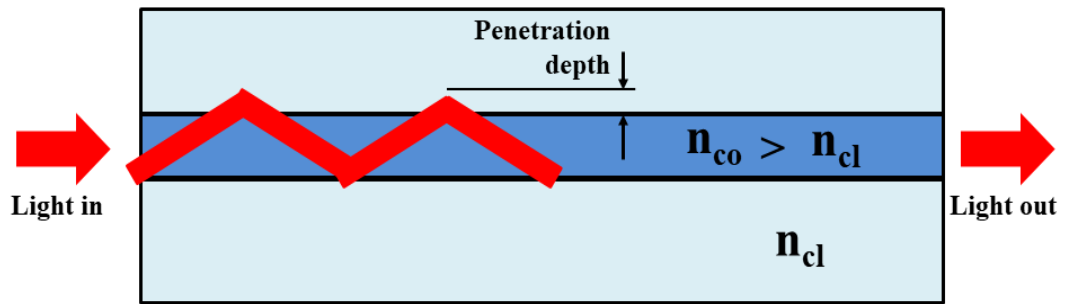


**Figure 2.11: The optical fiber cross-section profile along the long axis.**

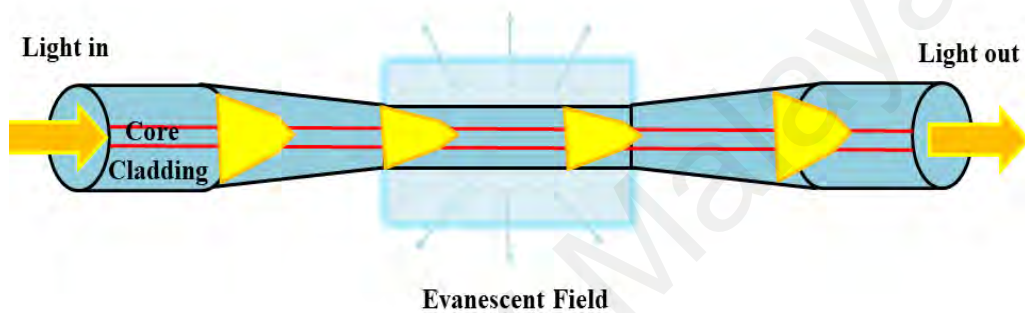


**Figure 2.12: Schematic diagram of microfiber evanescent region.**

The sensor sensitivity increases as evanescent field increase. In addition, numerous researches have endeavored to growth the penetration depth of the evanescent region and ease mode coupling by tapering (Franco & Serrão, 2017), bending (Khijwania & Gupta, 1999), increasing the wavelength (Moar et al., 1999) and altering the light launching angle (Ahmad & Hench, 2005). Silica microfiber has been utilized as a sensor for various field like in chemical (Chiam, Lim, Harun, Gan, & Phang, 2014) and biomedical subjected to the evanescent field advantages. For instance, microfiber coated with a certain polymeric nano-structure was proposed for PH sensor (Rivero et al., 2018).

In the meantime, a multi-walled carbon nanotubes (MWCNTs) coated silica microfiber sensor was used to identify magnesium ions ( $Mg^{2+}$ ) in de-ionized water (Yasin, Irawati, Isa, Harun, & Ahmad, 2018). The essential of the miniaturized scale fiber sensors over the classical devices accommodate a simple fabrication and mass-production, economical, great reproducibility and exceptional optical performance and are equipped to be commercialized and put into practice in the future.

## **2.6 Summary**

Chapter 2 discussed a literature review in which the recent progress on SHM for microfiber and SMSF. Optical fiber sensors have drawn great interest in recent years especially for application in the areas of structural health monitoring (SHM). Up to date, a number of optical fiber sensor has been proposed and demonstrated for monitoring the safety and health of composite materials, vast structural designing structures and quantitative substance process. These sensors were mostly in the forms of Mach–Zehnder interferometers (MZIs), fiber Bragg gratings and long-period gratings. In this thesis, simple, affordable and feasible temperature and strain sensors were successfully proposed and demonstrated for SHM purposes based on optical approaches.

## CHAPTER 3

### FABRICATION AND CHARACTERIZATION OF SENSOR PROBES

#### 3.1 Introduction

Optical silica microfiber is described as an optical fiber sensor that has a diameter near to the waveguide spectrum. In consequence of the miniature core breadth and great indices variance among the fiber core, which normally greater than 1.5 and the cladding like air which is 1.0, various intriguing optical advantages like large evanescent fields, tight optical confinement, huge waveguide dispersions and robust region enrichment can be attained in a microfiber (Antunes, Domingues, Granada, & André, 2012; Chen, Han, Liu, & Lü, 2015a; Dass & Jha, 2016; Tong, 2010). These properties initiate a lot of favorable circumstances for cultivating a miniaturized photonic device varying from filters, interferometers, and lasers to sensors (Pal et al., 2011). For instance, microfiber can be applied to develop miniaturized fiber optic sensors with fast response, low optical power consumption, large sensitivity, high flexibility and mini footprint, (Han, Ding, & Lv, 2014; Lou, Wang, & Tong, 2014).

Microfiber can be classified into two types; adiabatic microfiber (gradual taper) (Xu, Lu, Chen, & Bao, 2017) and non-adiabatic (abrupt taper). The fundamental distinction between these two microfibers lie on their transition region, which determines the light vitality in the center mode. In an adiabatic microfiber, there is a huge percentage of the light power linger inside the core mode ( $LP_{01}$ ) that is very persistence by not coupling with higher order mode. On the other hand, a non-adiabatic type of microfiber has rapid, rough and an unexpected shift in taper radius of the transition region, which promotes the light to couple with both core and cladding modes.

In details, the coupling appears dominantly among the un-tapered fiber's core mode and the initial dual modes of the microfiber waveguides ( $LP_{01}$ ,  $LP_{02}$ ), which because of the huge distinct of the refractive indices of silica optical fiber and air, the microfiber typically advocated exceed one mode (Muhammad, Jasim, Ahmad, Arof, & Harun, 2013).

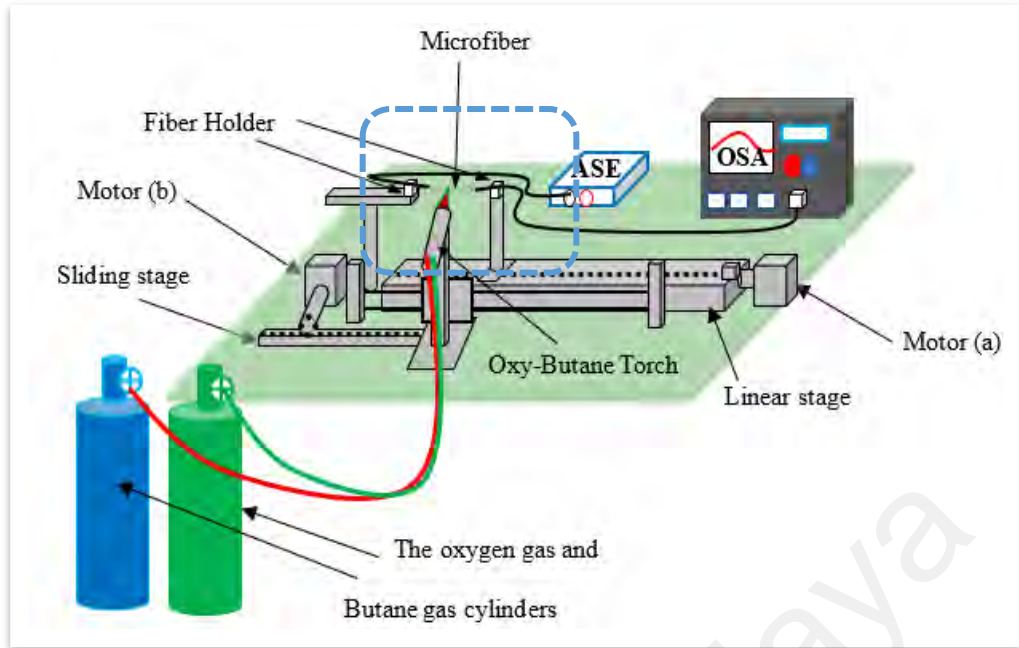
Apart from that, the multimode interference (MMI) theory has been magnificently scrutinized and anticipated numerous fiber exploitation like combiners, fiber telecommunication, beam splitters, fiber sensors multiplexers or comb filters (Paian & Macdonald, 1997; P. Wang, Zhao, Wang, Farrell, & Brambilla, 2018; Yao et al., 2012; Yin et al., 2016). Recently, the multimode interference featuring in a single mode–multimode–single mode (SMS) fiber structure has also been studied and nominated for various sensing applications such as refractometer (Frazao et al., 2011), and temperature sensors (Hatta, Semenova, Wu, & Farrell, 2010; Silva, Pachon, et al., 2012; Tripathi et al., 2009), edge filter for wavelength measurements (Q. Wang & Farrell, 2006) and a bandpass filter (Antonio-Lopez, Castillo-Guzman, May-Arrijoja, Selvas-Aguilar, & Likamwa, 2010). These optical devices grounded on an SMS fiber structure offer quite numbers fiber resolutions for optical communications and optical detecting without hardly lifting a finger of bundling and association with optical fiber framework.

In this chapter, the fabrication and characterization of both microfiber and SMS sensor probes are described. The microfiber and SMS devices are invented as of a silica single mode optical fiber (SMF) using a flame brushing and fusion splicing, respectively. The microfiber work will focus more on non-adiabatic type of microfiber where a periodic behavior is obtained at the output spectrum due to the oscillations as a result of back and forth coupling between core and cladding modes. At any rate, the SMS structure cultivates an adequate bandpass spectral response for indicating wavelength spectrum. Both sensor probes are used to demonstrate various sensing applications in the next chapters.

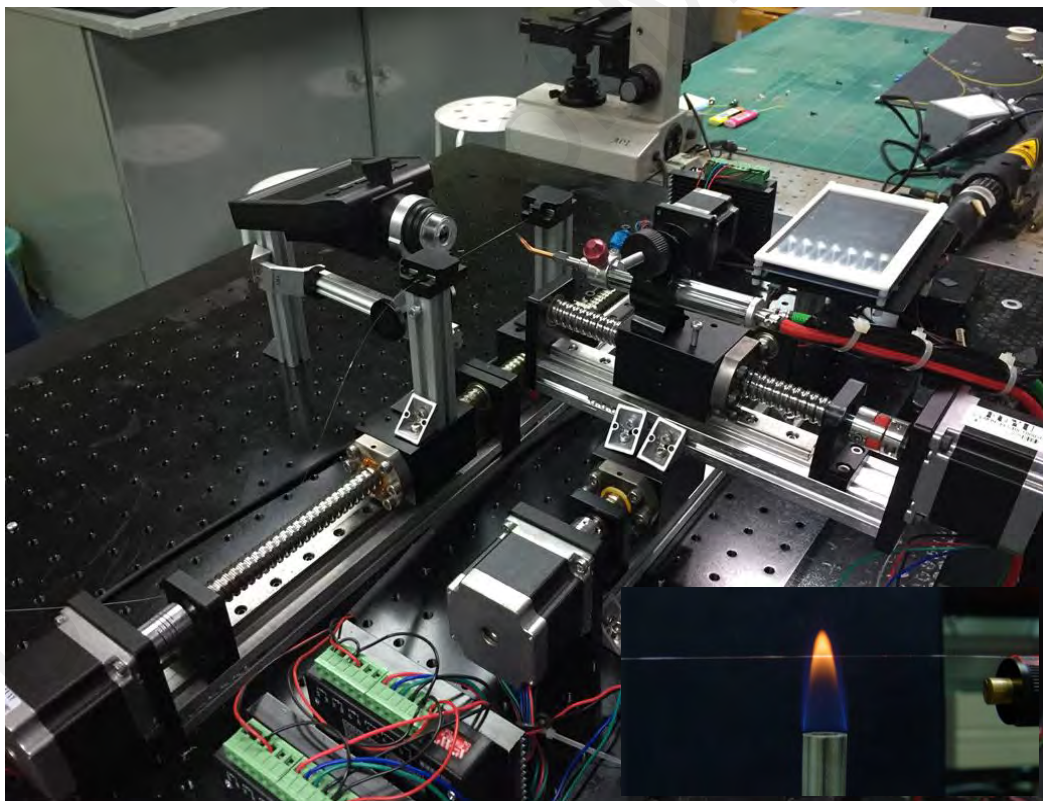
### 3.2 Fabrication of Microfiber

The microfiber or tapered fiber can be fabricated by various techniques such as flame brushing (Ji et al., 2016), electric circular segment, chemical etching via hydrofluoric acid (Haddock, Shankar, & Mutharasan, 2003) or laser technique. Among these techniques, flame brushing is the most common technique. This system utilizes a small-scale fire as a minuscule heating region to heat the optical fiber. The gas is blended with oxygen which originated out from gas burner to form flame without pollutant elements (Graf J. C. et al., 2009; Brambilla G. et al., 2010). The flame pressure can be controlled to adjust the thermal reading. The technique also has a flexibility to control the flame movement, which cause the stretching and pulling of the fiber abundant effortless to manufacture intended dimension microfiber. To continue, this method also can simply regulate the tapering dimension and the velocity of stretching. Hence, this approach produced great accuracy microfiber as per intended used.

Tapering a silica fiber includes reduction in the cross section by heating the fiber's waist and at the same time pulling the fiber's closures. The schematic experimental setup of the microfiber fabrication is shown in Figure 3.1(a) while Figure 3.1 (b) shows the real image of the experimental setup. The translation stage comprises of two stepper motors; one to control the pulling of the fiber, and another one to move the heating fire to allow the brushing process. Gas cylinders are placed near the stage that supplied oxygen gas and butane gas to the flame brushing machine. The torch chamber mixed both gases then supplied to a ~1mm estimated stick point fire at the light tip and 5 psi pressure regulated for both oxygen and butane gas.



(a)



(b)

Figure 3.1: Microfiber fabrication setup (a) schematic diagram (b) actual picture.

Inset shows the size of the flame.

The temperature range of the flame is 1100-1400°C, which can be monitored by controlling the oxygen gas volume. This temperature range is capable to heat and melt the silica fiber. But, the high temperature can cause the optical fiber bend and break easily during the tapering process and affect the amount of losses power. The pressure of the flame also can be controlled by the diameter of the tip torch. The flame become more stable with less pressure when the diameter of the torch is small. The core diameter of the torch is 0.2 mm which is appropriate to fire heat the fiber. Standard size of the flame is shown in inset of Figure 3.1 (b). Two high precision stepper motors are used to pull the silica fiber ends, which were clamped by a fiber holder. By controlling the speed of all the three translation stages, heating condition and the geometry profile of tapering region, can be acclimated to get the coveted diameter, profile, and length of waist with high efficiency devices (Lou et al., 2014). The tapered fiber shape is the essential feature which can influence the circulation of light in the microfiber and the loss which can affect the spectral output.

Tapering a silica fiber involve with heating process and at the same time pulling and stretching the fiber's closures. The minute the fiber is tapered using the flame and brushing technique, the fiber is redefined which means the light circulation privileged the core breaches to the cladding played the act of the new core, and the exterior medium is the new cladding. The fabrication of the microfiber is a tedious process, which requires diligence and persistence. Initially, a protective jacket is removed from a silica fiber by using fiber stripper, then the bare fiber is cleaned using acetone. Next, the fiber is placed and gripped by two fiber holders which are locked on two translation stages. During the tapering process, the edges of the fiber are associated to an amplified spontaneous emission (ASE) source and another end of the fiber connected to an optical spectrum analyzer (OSA) to monitor power loss and capture the spectral output changes.

In this proposed approach, without difficulty we manage to regulate the tapering dimension and the velocity of stretching dimension. Thus, the length of the microfiber can be manufactured with great precision and reproducibility. The pictures of the fiber beforehand and afterward the tapering is shown in Figure 3.2. Subsequently after tapering, the fiber waist width is decreased beginning at 125  $\mu\text{m}$  toward 1.5  $\mu\text{m}$ .

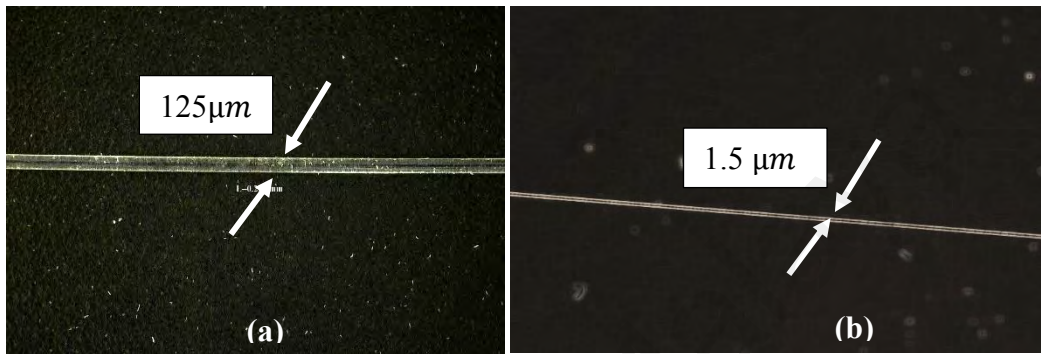


**Figure 3.2: Silica fiber (a) beforehand tapering and (b) afterward tapering**

### 3.3 Microfiber Characteristics

ASE source was utilized in real-time in conjunction with OSA to evaluate the spectral response characteristic of the fabricated microfibers. The ASE broadband light was projected through the fiber during tapering process and the output was monitored by an OSA. Microfiber is classified into adiabatic (gradual taper) and non-adiabatic (abrupt taper) types depending on the taper angle. The principle of dissimilarity between these two kinds of microfiber fit in either there is energy core mode stimulated towards the higher-order modes.

Adiabatic microfiber can be defined as if a substantial bit of the light energy stays in the core mode and avoid coupling towards cladding modes and at same time circulating across the microfiber (Zibaii et al., 2010). Accordingly, taper local span compulsory to be greater than coupling span to prevent the principle mode to couple with cladding modes.

Briefly, the local taper angle must be very small to prevent the light energy transmitted to different modes when the light circulates at the waist region (K. S. Lim et al,2012). An adiabatic microfiber should follow the adiabatic criteria (Xu et al., 2017);

$$\frac{dy}{dz} \leq \frac{r(\beta_1 - \beta_2)}{2\pi} \quad (3.1)$$

where  $\beta_1$  and  $\beta_2$  are corresponding to the local circulation coefficients in the fundamental modes and higher order modes transition, which power is most likely to be lost;  $r$  is the radius of the taper as a function of  $z$ , which is the distance along the taper longitudinal axis. To produce an adiabatic microfiber, the diameter of the tapered region must be uniform and unwrinkled with nominal exterior roughness and huge evanescent field.

With that reason, most crucial zone at both transition region of optical fiber restricted equivalent to microfiber conical shape. If the optical fiber bend, it will cause loss in light and increment in transient field and it is normally performed on a consistently de-cladded fiber (Littlejohn, Lucas, & Han, 1999). Figure 3.3 illustrated the diameter changes along 80 mm absolute distance of optical fiber taper including equable microfiber waist profile. The image demonstrated optical fiber realignment across transition region, began at 125  $\mu\text{m}$  width and managed to achieve 2 $\mu\text{m}$  at the end of the tapering process. Even so, both transition region associated with proportion almost equal 0.98.

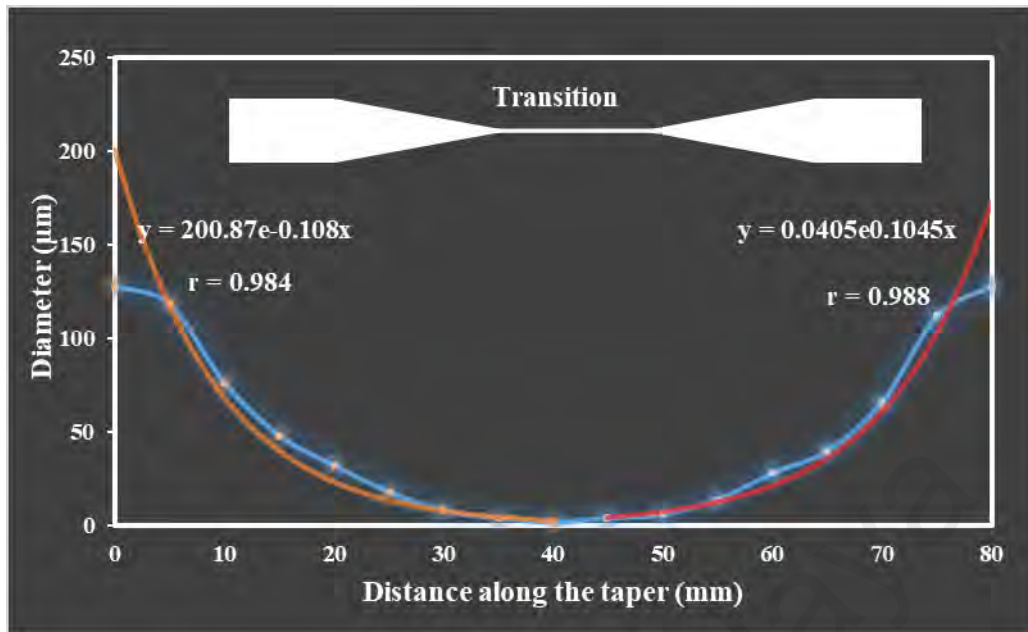


**Figure 3.3: The fabricated adiabatic microfiber profile at transition region. (Jasim, Ali Abdulhadi, 2010).**

The transmission ASE spectrum from the typical adiabatic microfiber is shown in Figure 3.4. The insertion loss after tapering was very small (less than 1dB) as amplified spontaneous emission light propagated along optical fiber beforehand and afterward the tapered process. Besides the unwrinkled conical shape at the silica microfiber transition region to obtain high efficiency adiabatic taper, the diameter tapering region also must be uniform. It is worthy to note that the output spectrum and insertion loss were strongly dependent on the tapering approach, such as, the speed of the moving burner and period of the flame applied to the fiber. The adiabatic microfiber has many potential applications in many devices such as all-fiber mode converters, multiplexers, microspheres, liquid-core optical ring-resonators, and micro-disks. It can likewise be used to fabricate a vastly sensitive surface plasmon resonance (SPR) sensing device.

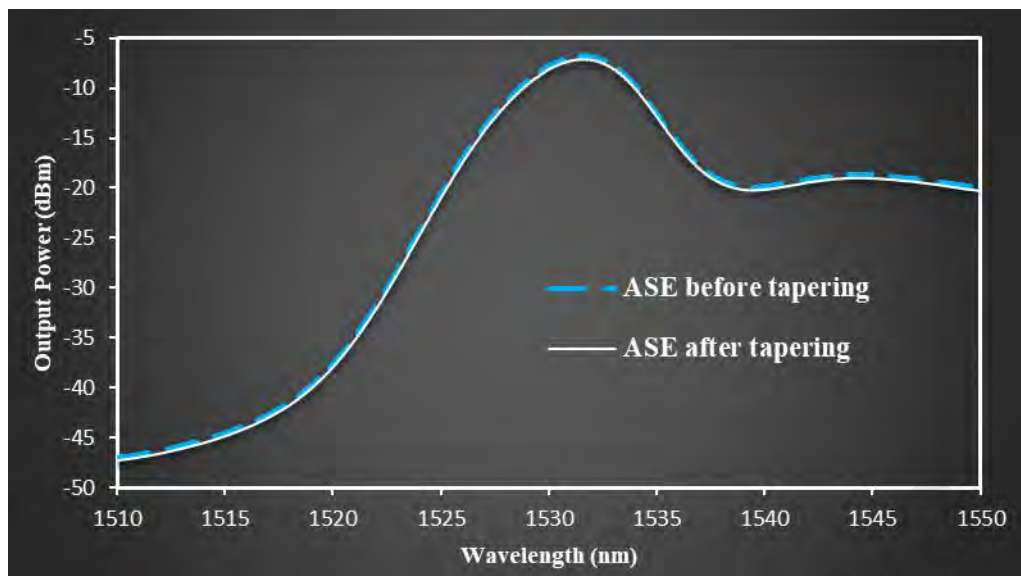


**Figure 3.4: The output spectrum before and after tapering process when the ASE light was launched into the fiber/microfiber (Jasim, Ali Abdulhadi, 2010).**

In a non-adiabatic microfiber, some lights energy travel in the cladding mode due to the coupling the power from the fundamental mode of the un-tapered fiber (Y. Xu et al., 2017). Technically, the tapering angle of the core is determined by the difference of effective refractive indices between the fundamental core mode  $HE_{11}$  and its closest higher order mode  $HE_{12}$  modes. For the non-adiabatic microfiber, the tapering angle of the core is larger compared to the adiabatic one. This causes the energy from the fundamental mode to be transferred into the higher-order modes (Muhammad et al., 2013). Figure 3.5 compares the physical properties between adiabatic and non-adiabatic microfiber. The non-adiabatic microfiber normally has a sharper tapering angle compared to that of adiabatic microfiber.

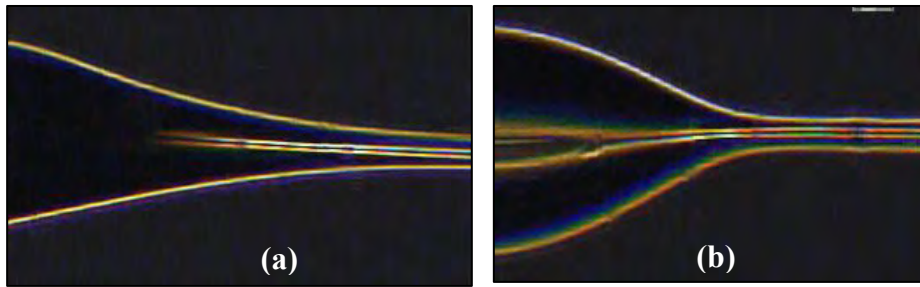


**Figure 3.5: Comparison of tapering angle between (a) Adiabatic and (b) Non-adiabatic microfiber.**

Interference will occur between the modes of light if the microfiber is bend or experience non-uniform tapering diameter in the transition region, as illustrated in Figure 3.6. The propagate light along the bend area will be separated into the two segments at the input conical area; guided and unguided modes. The guided modes continue to navigate along the core and the unguided modes circulates along the cladding. Interference between these modes produces a fringes spectrum at the output end of the conical region. The ASE spectrum taken before and after the tapering of a non-adiabatic microfiber is shown in Figure 3.7. A comb filtering effect is observed in the non-adiabatic microfiber.

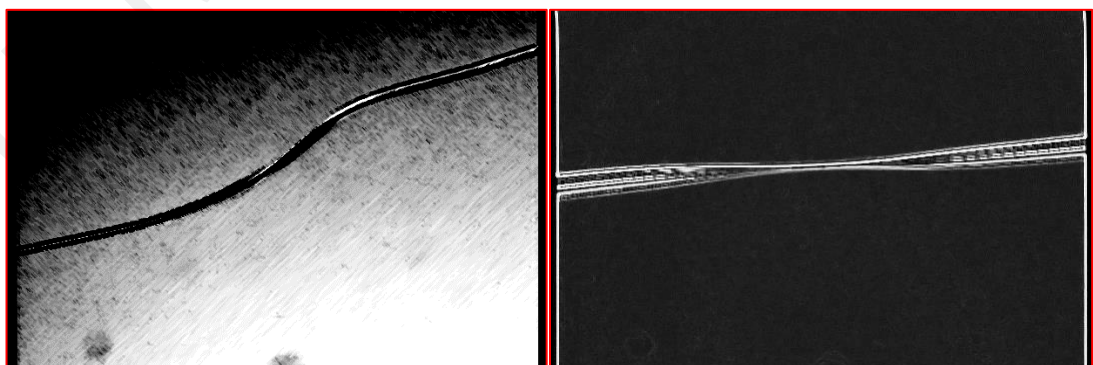


**Figure: 3.6: The bend and non-uniform tapering in the microfiber's transition region.**

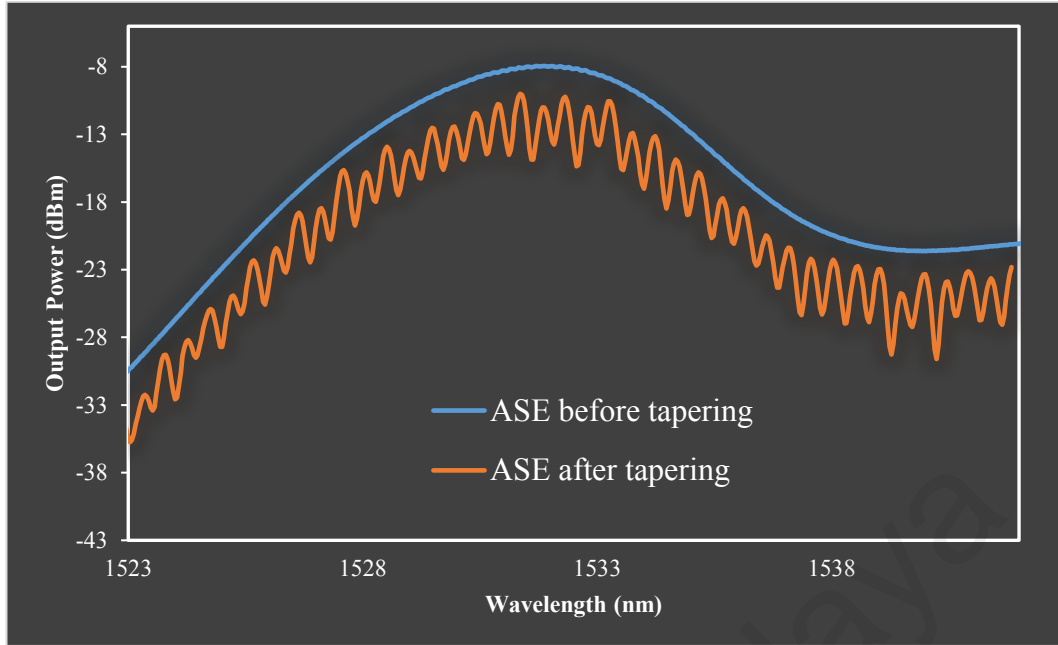


**Figure 3.7: Non-adiabatic microfiber's transmission spectrum output.**

The invented non-adiabatic microfiber is defined according to a transmission criterion of an interferometer model as (Mignani, Falciai, & Ciaccheri, 1998) :

$$I = I_1 + I_2 + 2\sqrt{I_1 I_2} \cos(\Delta\phi) \quad (3.2)$$

which  $I$  is the inference signal intensity,  $I_1$  and  $I_2$  are the intensities of the lights circulating in the fundamental mode and higher-order modes correspondingly while  $\Delta\phi$  is the phase variance between the interference modes which is relatively equivalent to:

$$\Delta\phi = \left( \frac{2\pi(\Delta n_{eff})L}{\lambda} \right) \quad (3.3)$$

where,  $L$  is the taper waist region of microfiber,  $\Delta n_{eff}$  is the variance of the effective refractive index of the fundamental modes and the higher order modes ( $n_c^{eff} - n_{cl}^{eff}$ )

while  $\lambda$  is the light source's wavelength. Configuration for the fringe among both of the inference orders is defined as

$$\Delta\lambda = \frac{\lambda_0^2}{(\Delta n_{eff})L} \quad (3.4)$$

Where  $\lambda_0$  is the initial light source's wavelength. Any variations in the  $L$  and  $\Delta n_{eff}$  would force  $\Delta\phi$  to shift as the subsequent of the shift of the output interference spectrum. For example, if the temperature of the encompassing condition of the microfiber shifted, the distinction in engendering coefficients and the relative phase between dissimilar modes will be adjusted, prompting a change in the output spectrum. It is also expected that when the light is launched into the microfiber and propagates along the air-cladding of waist of silica microfiber, the non-adiabatic fiber's mode coupling can be regulated between fiber core of un-tapered region and the initial two modes of waveguide cladding.

Thus, the intensity and the evanescent wave field's penetration depth are essentially fortified, prompting a bigger cover with the encompassing medium. The change of refractive indices of encompassing medium varies the effective refractive index,  $\Delta n_{eff}$  of the closest higher order modes. Subsequently, the transmission spectrum will react by shifting the interference spacing, which can be used for various sensing applications.

### **3.4 Single-mode Multimode Single-mode Fiber (SMS) Based Interferometer**

Proficiency to endure ruthless environments and the capability to multiplex signals have driven optical fiber application goes beyond telecommunication usage. The optical fiber was used for various measurements including strain (Li et al., 2012), temperature (Irigoyen, Sánchez-Martin, Bernabeu, & Zamora, 2017), chemical (Zhao, Huang, He, & Chen, 2010), and pressure due to their large bandwidth and low propagation attenuation (Gao, Wang, Zhao, Meng, & Qu, 2010; Shao et al., 2014; Qiang Wu, Muhammad Hatta, Semenova, & Farrell, 2009). Despite the fact that the optical fiber mechanical physical properties are critical for its utilization in sensors (Antunes et al., 2012), the challenging application of the optical fiber in aggressive environment may lead to the degradation of its physical reliability (Nosenzo, Whelan, Brunton, Kay, & Buys, 2013). Therefore, several new configurations have already been developed. For instance, a fiber Bragg grating (FBG) is founded to be the optical sensor that is generally utilized and well-known fiber optical sensors (Gunawardena, Lai, Lim, Malekmohammadi, & Ahmad, 2016). Nevertheless, FBG suffers from a narrow measurement range mostly in strain detecting application. Because of that, FBG need mechanical arrangement to enhance the measurement range and a complex interrogation system to accomplish a high wavelength resolution (Oliveira et al., 2016; Zulkifli et al., 2016).

Short while ago, the single mode-multimode-single mode fiber (SMS) structure have been employed in an extensive domain applications ranging from telecommunications to sensors, and lasers (Ian et al., 2017; Ruiz-Pérez, Basurto-Pensado, LiKamWa, Sánchez-Mondragón, & May-Arrijoja, 2011; Yaxun Zhang et al., 2014). For instance, Zhang et al. (Yaxun Zhang et al., 2014) suggested the employment of SMS structure for interferometry based refractive index detection (Yaxun Zhang et al., 2014).

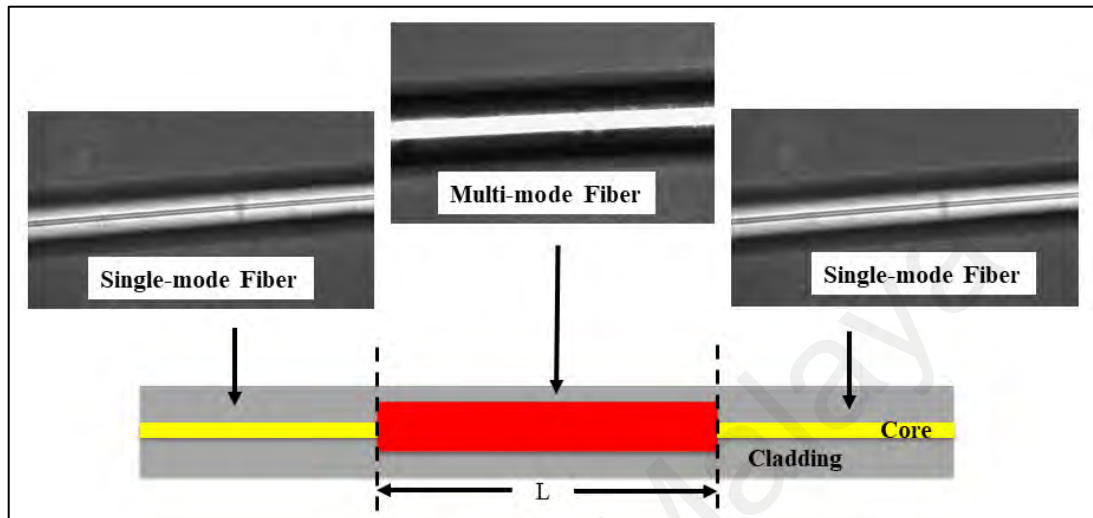
Wu et al. also proposed that a uniquely outlined SMSF structure can be utilized for a refractive index sensor through their investigation of utilizing a wide-angle beam propagation method (BPM) (Qiang Wu, Semenova, Wang, & Farrell, 2011a).

SMSF has also been recommended as a strain sensor as it engenders an ample bandpass spectral response for a specified wavelength spectrum. For that reason, SMSF can be utilized as either a stand-alone sensor or an edge filter, where grills as an optical sensor such as FBG. As a result, a sensor based on SMSF structure will be more profitable than FBG based sensor since SMSF structure is more effortless to fabricate compare to the FBG sensor. (F. Xu, Chen, Peng, Xu, & Wu, 2012; Zulkifli et al., 2016). In this section, construction, working principle, characterization and application of a SMS structure are presented. A simple SMS structure is also proposed to evaluate strain or load. This approach attempts favored circumstances of a less difficult arrangement, simplicity of manufacture, and high resolution.

#### **3.4.1 Design and Construction of the SMS Structure**

SMS structure can be fabricated based on two basic steps; cleaving and splicing. Figure 3.8 shows the schematic diagram of the SMS basic structure that comprises of three segments; single-mode fiber (SMF), multimode fiber (MMF) and another SMF. The core diameter of both SMFs is about 9  $\mu\text{m}$  while for the MMF consumes a core's diameter of 50  $\mu\text{m}$ . Both SMF and MMF have a cladding diameter of 125  $\mu\text{m}$ . The small core diameter of SMF only allows one mode of light to propagate inside the core through a process of total internal reflection. It has a cut-off wavelength of around 1200 nm and thus, 1550 nm light can propagate with a low loss and without any multimode dispersion. MMF with a bigger core enables a number of modes of light to propagate.

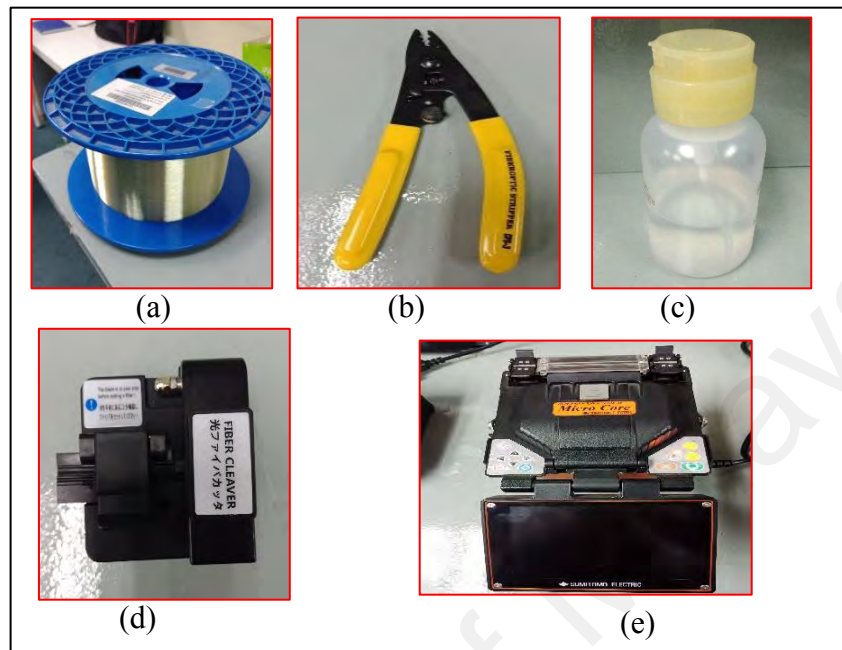
Due to the high scattering and constriction rate, the quality of the signal is diminished across long distance. Hence, in this study, only a short length of MMF in arrange of 1 to 11 cm is used.



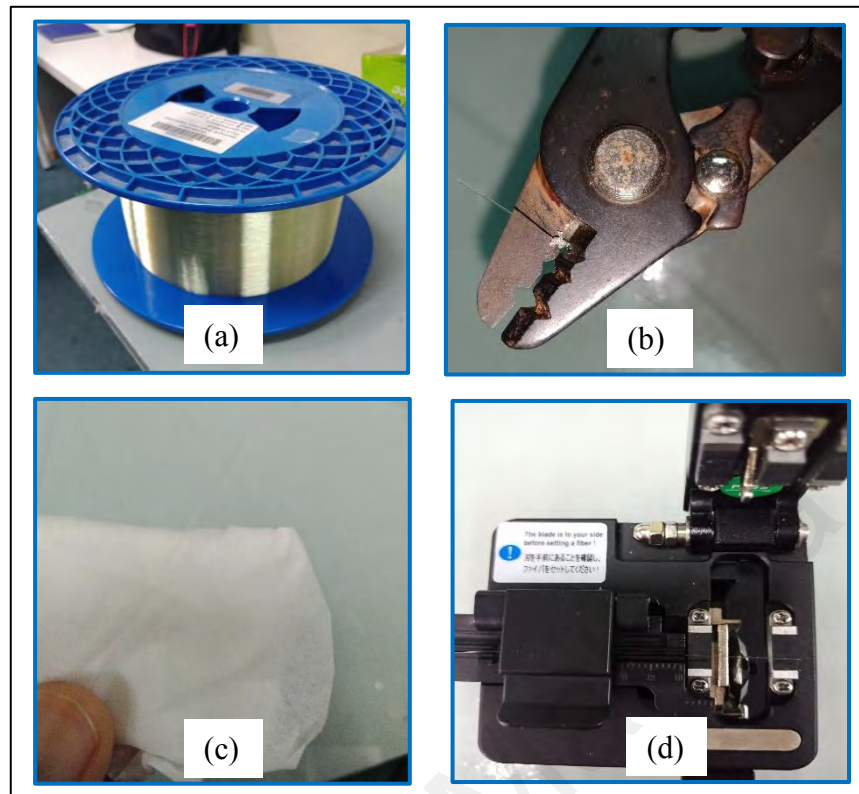
**Figure 3.8: Schematic diagram of the SMS fiber structure.**

Figure 3.9 shows materials, tools and an equipment used in the construction of SMS structure through the cleaving and splicing procedures. The splicing process begins by preparing both fiber ends for cleaving, which requires all protective coating stripped from ends of each fiber. At first, the protective coating of an optical fiber (Figure 3.9(a)) was stripped by using a fiber stripper (Figure 3.9 (b)). Then, the bare fiber was cleaned with alcohol (Figure 3.9(c)) and wiped by a lens tissue to remove residual particles as illustrated in Figure 3.10. After that, the bare fiber was cleaved by a cleaver (Figure 3.9(d)). During the cleaving process, the fiber was placed into a cleaver's fiber groove, then the cleaver's upper arm was pressed so that it mechanically released a very fine blade to cut the fiber as illustrated in Figure 3.10. The end-face of the cleaved fiber is perfectly flat and perpendicular to the axis of the fiber. The end of the fiber must be cut to a 90-degree flat-end in order to prepare the fiber for the next splicing process. If the fiber ends are not precisely cleaved, the ends will not mate properly.

Figure 3.11 compares the illustration of excellent and poor cleaving. The poor cleaving may give a significantly higher power loss after splicing.



**Figure 3.9: Materials, tools and equipment used for construction of SMS structure probe (a) raw optical fiber (b) fiber stripper (c) alcohol for cleansing process (d) cleaver (e) Ericson FSU-975 fusion splicer.**



**Figure 3.10: The cleaving process procedure (a) cutting the optical fiber (b) stripping (c) cleaning (d) cleaving.**

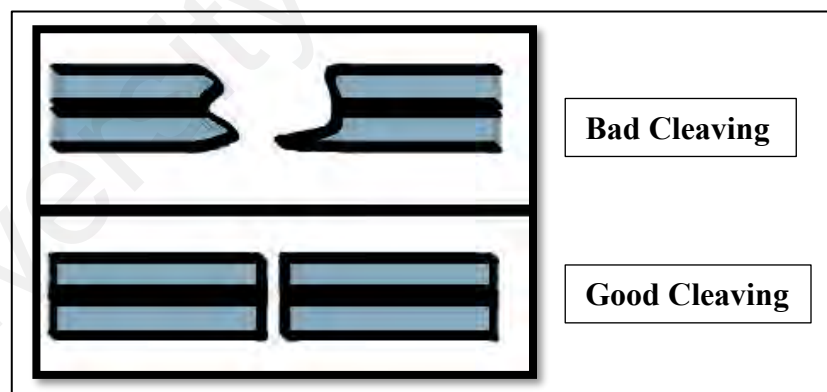


**Figure 3.11: Illustration of fiber cut with 90-degree flat-end.**

Fusion splicing is the mechanism of fusing or intertwining two optical fibers together by an electric curve as they accommodate the most minimal misfortune and minimum reflectance, and in addition of giving the most grounded and most dependable joint between two fibers. There is safety operational precaution compulsory to attend during the splicing.

When the splicer is on, never touch the electrodes, not under any condition disclose the security shield or the power supply, and not at all embed matters other than stripped and cleaned optical fiber. Figure 3.12 shows the component of Ericson FSU-975 fusion splicer and the function for each component. The Ericson FSU-975 can be executed by whether a 12 V DC battery or a 50-60 Hz power supply resources. There are basic steps to operate the splicer; first, link the splicer to the power supply, second, develop the fibers including stripping, cleaning and cleaving the optical fibers and thirdly switch on the splicer then locate the fibers. However, if re-open the security shield, the splicer will switch off immediately. Then, choose splicing mode either auto mode or manual mode and also the program. Normally, when it being switched on, the splicer constantly outset in auto mode. Fifth, push the fuse green knob to splice the fibers and finally check the fiber visually and assess the fiber quality based on an estimated splice loss was display (Ericsson Cables AB, 1999).

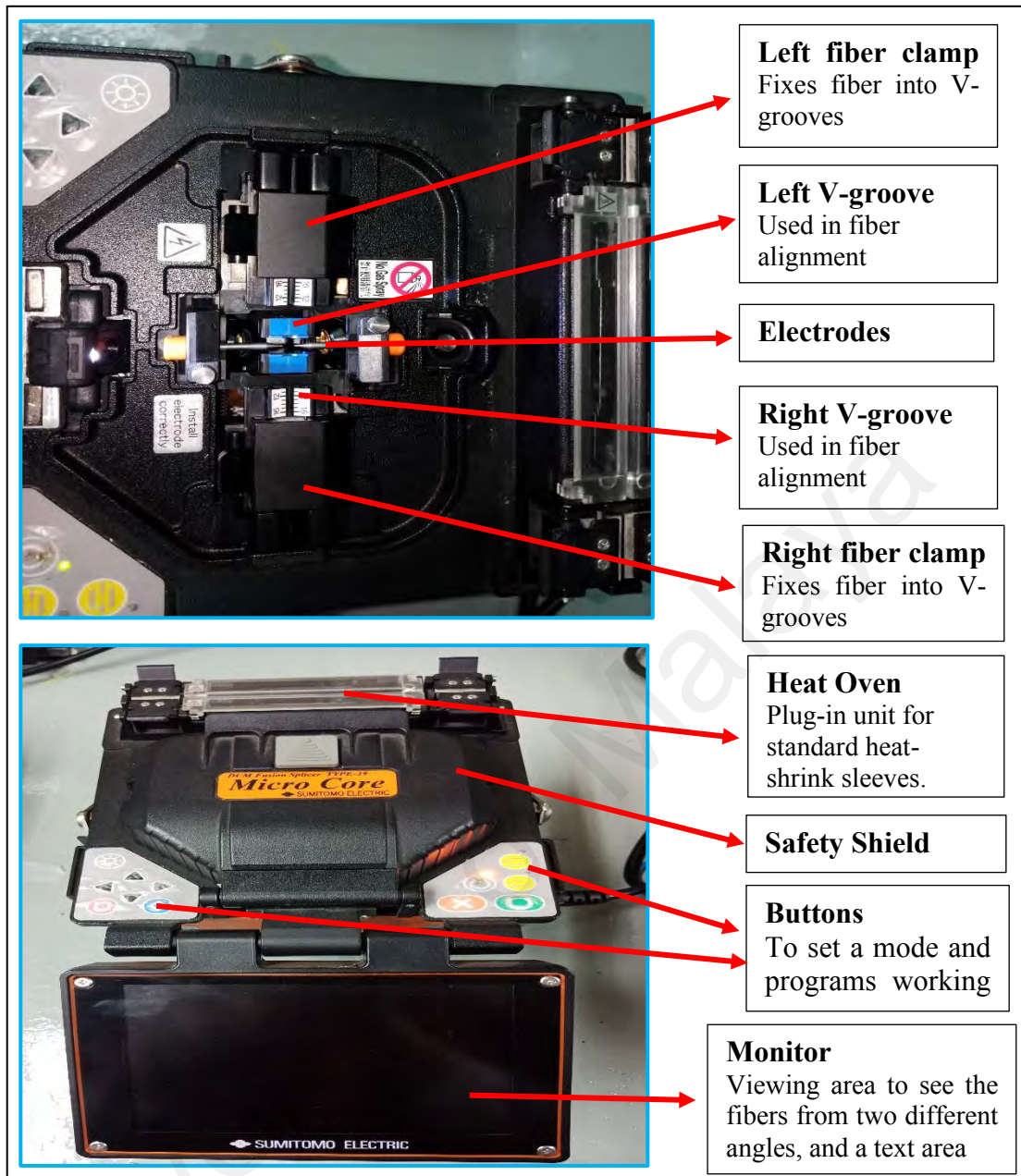


**Figure 3.12: Description of the Ericson FSU-975 fusion splicer.**

In splicing process, both SMF and MMF end fibers were placed into Ericson FSU-975 fusion splicer, facing towards each other and perpendicular to the electrodes that will generate an arc throughout the splicing process. As shown in the Figure 3.13, two cleaved fibers were regulated by bringing both fibers together close to both electrodes. Both fibers were placed into the V-grooves till they are noticeable in the screen, and afterward shutting the safety shield. The appearance of both fibers was then checked at the monitor before splicing to ensure they were clean and well-cleaved.

If there are any defects, the fibers must be taken out and re-prepared. Figure 3.14(a) shows both views at the monitor that needed to check. The fiber's alignment was adjusted or relocated till the exterior ends of the fibers aligned, and the spacing between their edges is centered on the screen as little as possible while still permitting the fiber to shift up and down as shown in Figure 3.14(b). When both fibers were aligned to the satisfaction, fuse green button was pressed. An electrical arc was formed over the electrodes to melts the fibers and completes the splicing process with loss less than 0.05 dB. Once the splicing sequence is completed, the splicing joint should be checked. If there are any defects as illustrated in Figure 3.15 and the loss is greater than 0.1dB, the fibers should be re-prepared as per discuss previously and the splicing procedure should be repeated.

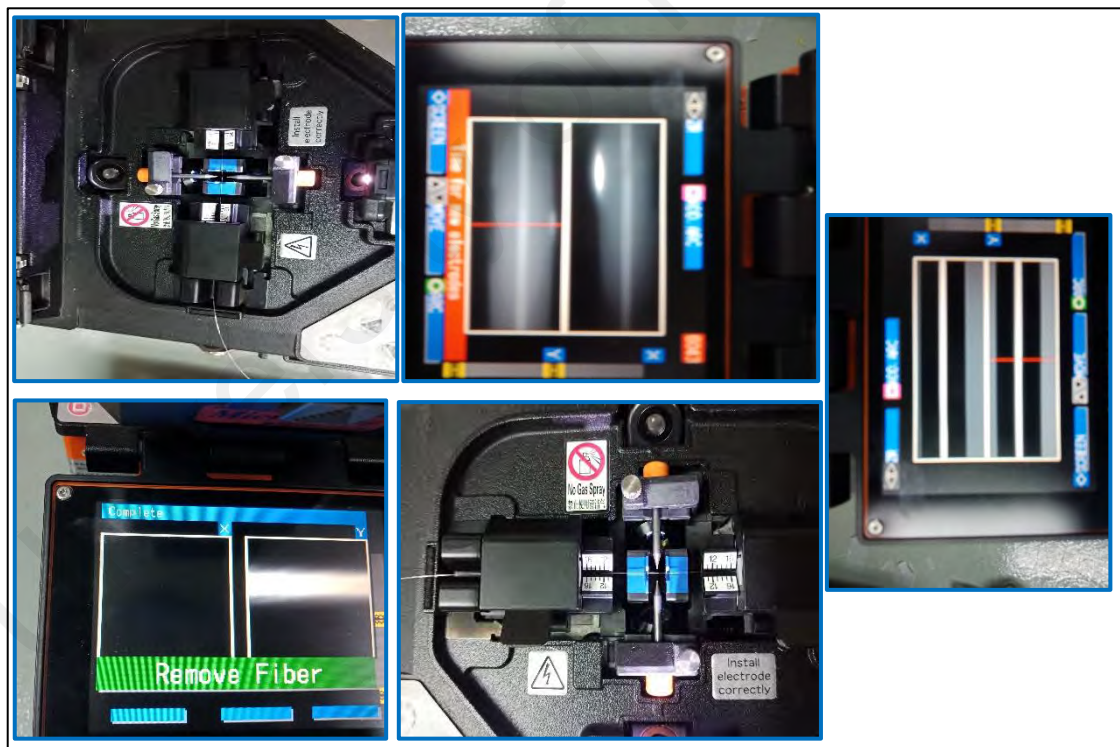


**Figure 3.13: Images of the splicing operation.**

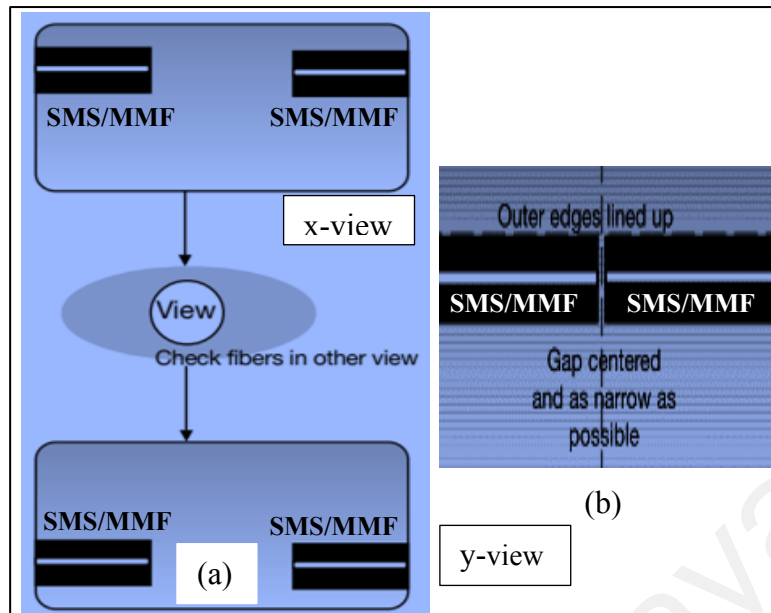


**Figure 3.14: Fiber's alignment during splicing.**

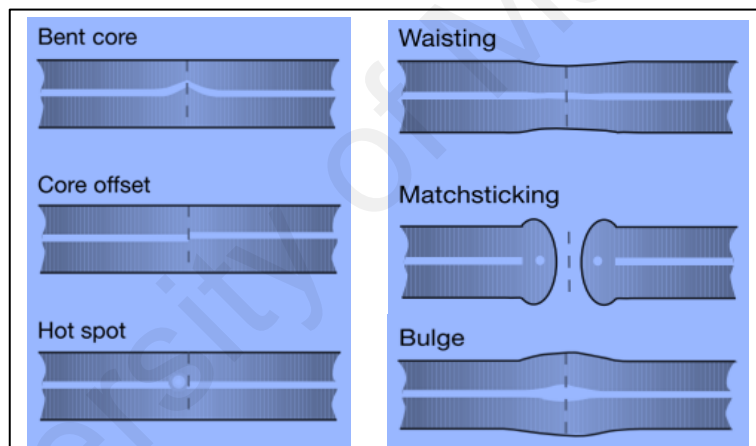


**Figure 3.15: Splicing defects.**

### 3.4.2 Characteristic of SMS

The single-mode–multimode–single-mode (SMS) operates based on multimode interference, which was excited between modes in the multimode fiber (MMF) area. It has a bandpass spectral response, which can be affected by exterior agitation (Mohammed, Mehta, & Johnson, 2004) (Q. W. Q. Wang, Farrell, & Yan, 2008). Hence, the SMS structure can be utilized as a sensor device to measure strain, refractive index, temperature, and humidity (Qiang Wu, Semenova, Wang, & Farrell, 2011b).

For instance, a compact and high sensitive refractive index (RI) sensors were reported by observing the changes of the transmission dip of the spectrum. (Chen, Han, Liu, & Lü, 2015b; Silva, Frazao, Santos, & Malcata, 2012; Wolfbeis & Wang, 2000). The multimode interference (MMI) theory has also been broadly studied and designed as a base for a lot of innovative fiber sensors likes combiners, beam splitters and multiplexers for fiber sensors ,fiber telecommunication and comb filters (Rahman, Somasiri, Themistos, & Grattan, 2001; Yin et al., 2016; Yujuan Zhang et al., 2013).

Figure 3.16 compares cross section, refractive index profile and light path between MMF and SMF. As viewed, the MMF aid numerous modes that circulate with various speeds and show different mode field profiles (Feng, Tam, Chung, & Wai, 2006). The refractive index for a straight fiber across the transmission route has a symmetrical profile, hence the light circulation in the straight MMF area is likewise symmetrically conveyed.

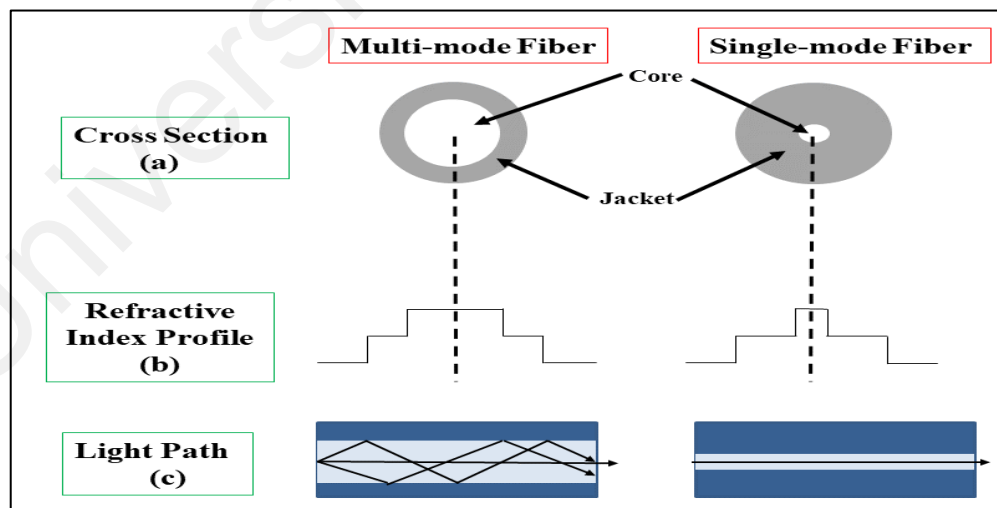


**Figure 3.16: Refractive index profile for SMF and MMF structure.**

However, for a bend MMF, the refractive indices is not symmetrical and described as (Schermer & Cole, 2007);

$$n = n_0 \left( 1 + \frac{x}{R_{eff}} \right) \quad (3.5)$$

where  $n_0(x, y)$  is the straight fiber's refractive indices while  $R_{eff}$  is the equal bend radius that act in accordance with:

$$R_{eff} = \frac{R}{1 - \left( \frac{n_0^2}{2} \right) [P_{12} - \nu(P_{11} + P_{12})]} \quad (3.6)$$

which R is the fiber's bend radius,  $P_{11}$  and  $P_{12}$  are photo-elastic tensor's mechanisms and  $\nu$  is the Poisson ratio.

Meanwhile, an in-line fiber optic Fabry-Perot interferometer (FPI) necessitates the arrangement of dual parallel isolated mirrors to partly mirror the optical signs info into various optical ways. Various approaches have been utilized to shape the reflects in the SMF, for example, splicing a stub of hollow core fiber or hollow core photonic crystal fiber among two segments of SMFs (Duan, Rao, Hou, & Zhu, 2012) (Y. J. Rao, 2007), establishing a micro-notch by utilize of femtosecond laser (Y.-J. Rao et al., 2007; Wei, Han, Li, Tsai, & Xiao, 2008), splicing (Duan et al., 2012), film coating techniques (Lee, Gibler, Atkins, & Taylor, 1992), using chemical etch (Machavaram, Badcock, & Fernando, 2007), and created by a sector of endlessly single-mode photonic crystal fiber (EPCF) and conservative SMFs (Yun Jiang Rao, Deng, Duan, & Zhu, 2008). The relative phase difference of the two beams which by the condition of the two beams reflected by the mirrors have an optical way distinction (OPD) defined by (Zhu, Wu, Liu, & Duan, 2012):

$$\phi_{FPI} = \frac{4\pi nL}{\lambda} \quad (3.7)$$

which  $\lambda$  is the wavelength of the input, and  $n$  is the FPI cavity refractive indices (RI) while  $L$  is the FPI cavity length. The phase difference  $\phi_{FPI}$  among the two beams will be affected, as a perturbation is applied to the FPI, since the cavity length is increasing. The difference of  $\phi_{FPI}$  adds to the obstruction changes, that enables the FPI to be utilized for strain and temperature detecting.

The output spectrum of the fabricated SMS structure estimated at room temperature utilizing OSA at a 0.05 nm resolution is demonstrated at Figure 3.17 at various MMF lengths. The bandpass outcome is an effect of multimode impedance and recoupling inside the SMSF sensor. Being monitored, the range of the comb wavelength got to have a various steady crest to crest formation according to the MMF length. As a length increase, number of dips increase as number of peak spacing is various. For a different MMF length, the refractive index at the circulation route is distributed. It is expected that the impedance spectrum shifts as soon as strain is enforced on the multimode fiber. The best length for MMF are 7cm and 9 cm.

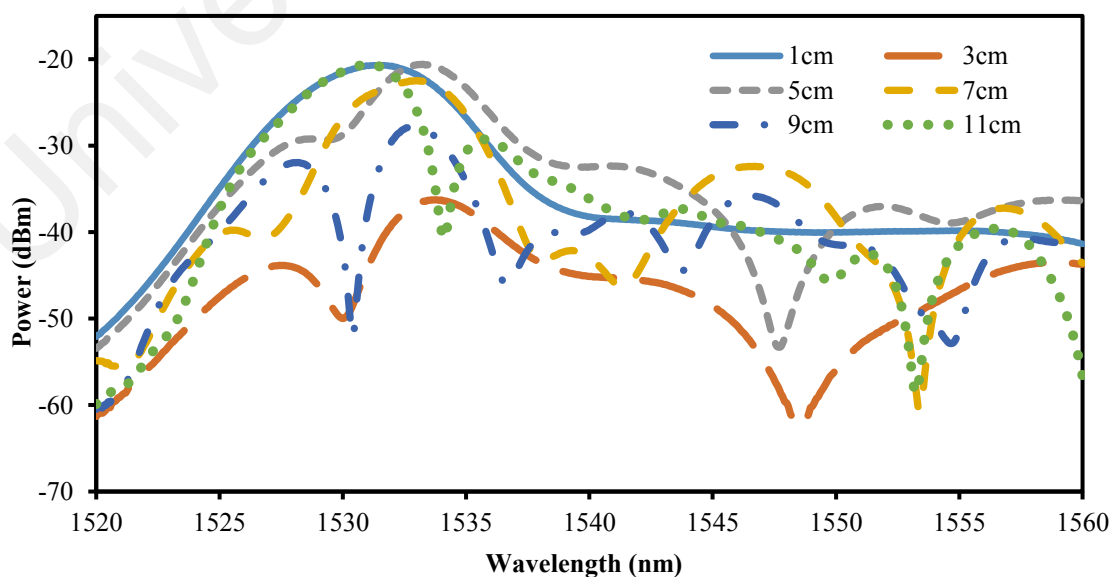


**Figure 3.17: Output spectrum for SMS fiber structure with different MMF length.**

### 3.4.3 Simple Load Sensor Using the SMS Probe

SMS structure can be utilized as a stand-alone sensor or an end filter that interrogates an optical device, for example, a fiber Bragg grating. Considering SMSF structure is significantly less demanding to manufacture compare to the FBG, a device founded on an SMSF structure will be much profitable compare to the FBG based sensor.

Earlier, the sensor based on SMS fiber has been fascinated in countless practices, for example, displacement (Qiang Wu et al., 2010), pressure (Ruiz-Pérez et al., 2011) and temperature sensors (Gao et al., 2010; Q. Wu, Semenova, Hatta, Wang, & Farrell, 2010). Besides, the optical fiber structure based on a straight SMSF sensor can be utilized as a load sensor, nonetheless simply like a FBG device, a straight SMS fiber structure also experience difficulty due to an inadequate measurement spectrum, because of the insufficient applied strain which to prevent the SMSF to break.

In this study, special fabricated SMS fiber structure is utilized like FPI device. An illustrative drawing of experimental arrangement and SMS fiber structure was shown in Figure 3.18. Both ends of MMF connection were glued to a stage while the load is hanged at the SMS fiber. The length of the MMF core diameter of 50  $\mu\text{m}$  varies from 1cm, 3cm, 5cm, 7cm, 9cm and 11cm and is labelled as L. The single mode fiber is spliced and fused to model the SMS fiber structure. Consecutively to monitor the SMS spectrum output, an interrogator system Erbium amplified spontaneous emission (ASE) was used to transmit the light along the SMS fiber structure. The MMF section from the SMSF sensor which infused by ASE light source will energize different modes proliferating in the MMF. In this experiment, the load measurement was carried out in the load range of 0.0 N – 1.5N with an increment of 0.2 N. After 1.5N the sensor output become more radical and unstable because the fiber reached the breaking point.

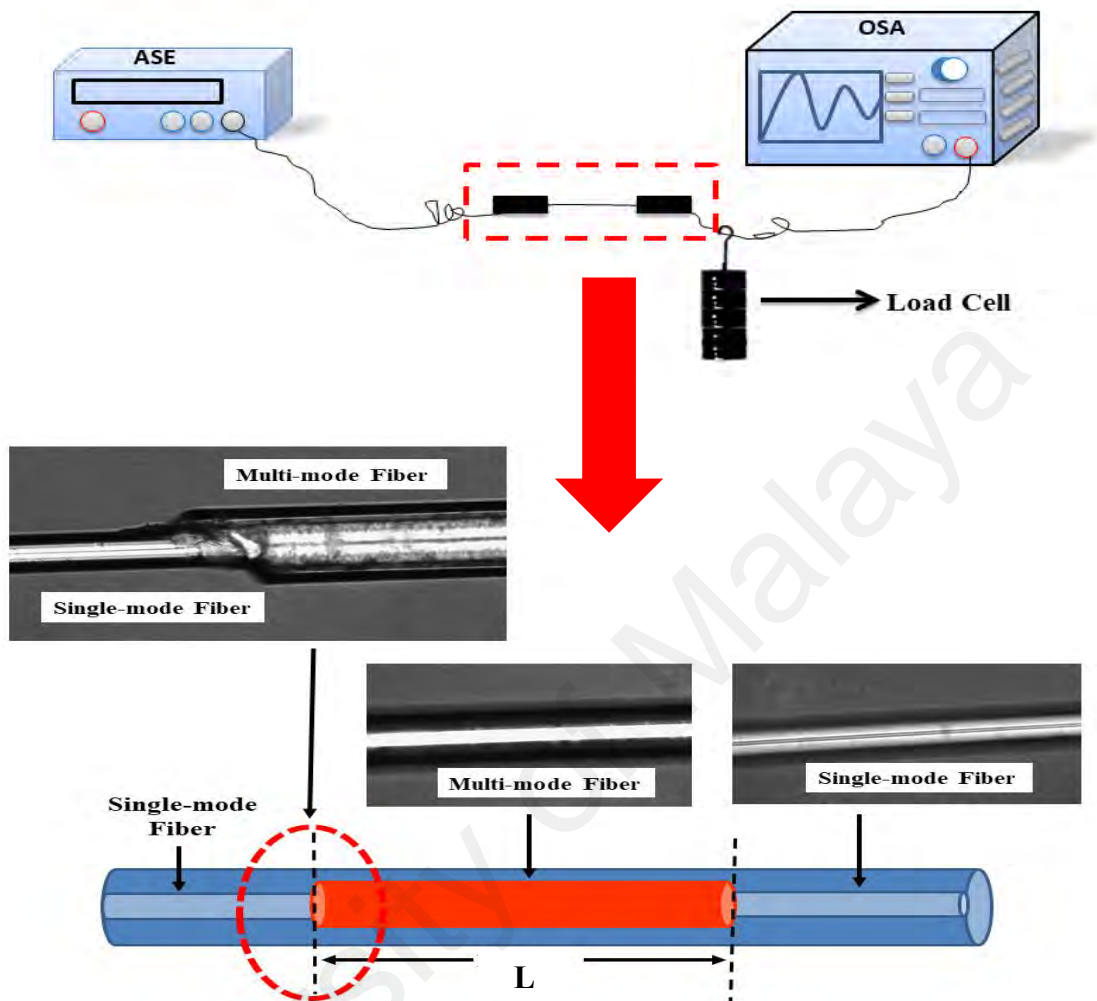


**Figure 3.18: Illustrative drawing of the recommended load sensor experimental arrangement. Inset displays the portrait of the SMSF structure.**

The focus for this study was to study the impact of vertical load on the SMS structure as appeared in Figure 3.18. This setup was intended to engender even circumstances of horizontal strain inside the MMF core. Load was enforced to the SMS fiber by dangling the load cell at the patch cord FC/UPC G652D. The test methodology is as per the following. The SMS fiber was installed by  $L = 1$  cm, output spectrum of impedance crest without load also recorded. Applied load was being increased to the maximum of 1.5N and for every 0.2N, the output spectral response is noted.

After that, the SMSF was un-loaded and the experimental was carried out for  $L= 3$  cm until  $L=11$ cm. Once the straight SMSF structure is enforced by the load cell, the MMF dimension is changed. Consequently, the multiple phases among these different modes and the spectral response of the SMSF happened to shift as well. The recorded wavelength spectral output of the SMSF at  $L = 1$  cm until  $L = 11$  cm are demonstrated in Figures 3.19, for different numbers of vertical loads or transverse strain.

University of Malaya

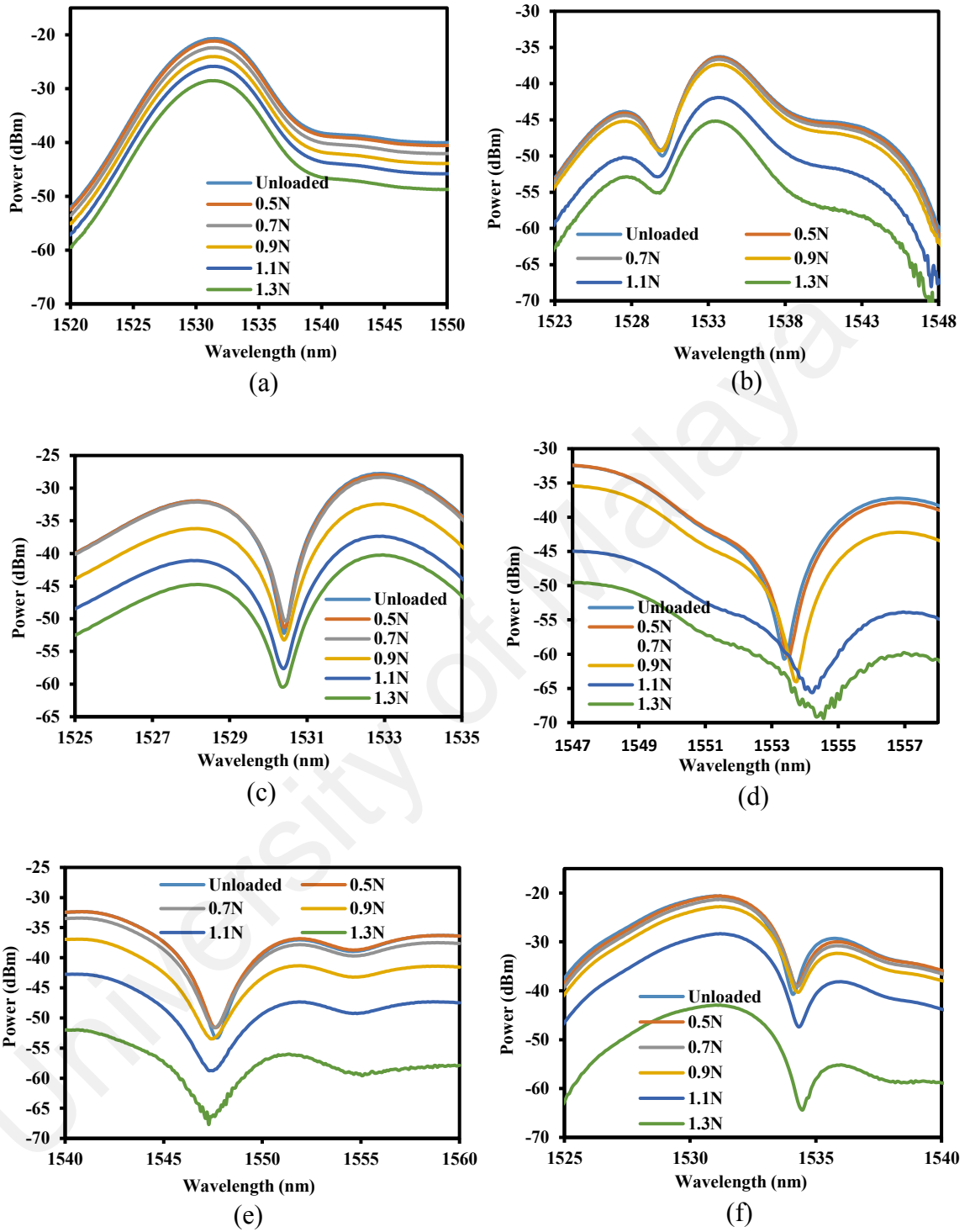


**Figure 3.19: The SMSF's spectral response at various vertical load values at different length (a) L=1 cm, (b) L=3 cm, (c) L=5cm, (d) L=7cm, (e) L=9cm, and (f) L=11 cm.**

During the laboratory work, the readings were recorded at 40 nm span length and 0.05 nm resolution. As load increased, wavelength of the crest and impedance comb bandwidth shifted as shown in Figure 3.19 and Figure 3.20. The refractive indices dissemination is never again symmetric for a bent MMF and compulsory characterized via an equivalent refractive indices dissemination as states (Qiang Wu, Semenova, Wang, Hatta, & Farrell, 2011):

$$n = n_0 \left( 1 + \frac{x}{R_{eff}} \right) \quad (3.8)$$

which  $n_0(x, y)$  defined as the straight fiber's refractive indices while  $R_{eff}$  described as the equivalent bent radius according to the below expression:

$$R_{eff} = \frac{R}{1 - \frac{n_0^2}{2} [P_{12} - \nu(P_{11} + P_{12})]} \quad (3.9)$$

And that  $R$  denotes as the fiber's bent radius and  $\nu$  is the Poisson ratio while  $P_{11}$  and  $P_{12}$  are photo-elastic tensor's mechanisms. The dissemination region inside the bent MMF segment is uneven as demonstrated in Eq. (3.8) subsequently the bent MMF efficiently has an uneven refractive indices dispersion as shown in Eq. (3.9). The MMF's bend segment devote a very powerful impact on the mode dispersion in the SMSF sensor, thus give an intense significant outcome on the whole propagation SMSF's features as proven in Figure 3.19. From these output, it can be deduced that the crest 3dB bandwidth rise and the crest spectrum of the impedance comb range changes to a shorter wavelength as the transverse strain increases. Moreover, as the vertical load increase, the power spectrum also arises. The relationship between the impedance wavelength crest and the load volume at different  $L$  is outlined in Figure 3.20.

The wavelength crest shifts linearly to a shorter wavelength spectrum with increasing load but differ for  $L=7\text{cm}$  and  $L=11\text{cm}$ . For  $L=7\text{cm}$  and  $L=11\text{cm}$  the wavelength shift to the longer wavelength as load increases as being demonstrated in the figure. As load increases, SMSF loss also increase. Shifter to longer wavelength, which have higher gain.

The slopes attained was varies with linearity more than 99 at  $-0.2698\text{ nm/N}$ ,  $-0.1803\text{ nm/N}$ ,  $-0.3736\text{ nm/N}$ ,  $0.7619\text{ nm/N}$ ,  $-0.1242\text{ nm/N}$  and  $0.2639\text{ nm/mN}$  for  $L = 1\text{ cm}$  until  $L = 11\text{ cm}$ , correspondingly. The output indicates that the highest sensitivity sensor occurs at  $L = 7\text{ cm}$ . The smallest gradient accomplished at  $L = 9\text{ cm}$ , exhibits at  $L=7\text{cm}$  and the effective horizontal strain enforced into MMF is higher contrasted to  $L = 9\text{ cm}$ . The reason for the fiber to experience this phenomena is associated to the decreased bending radius, thus shift the mode dispersion and also change the phase inside the SMS fiber structure according to the Eq. 3.8 and 3.9, respectively.

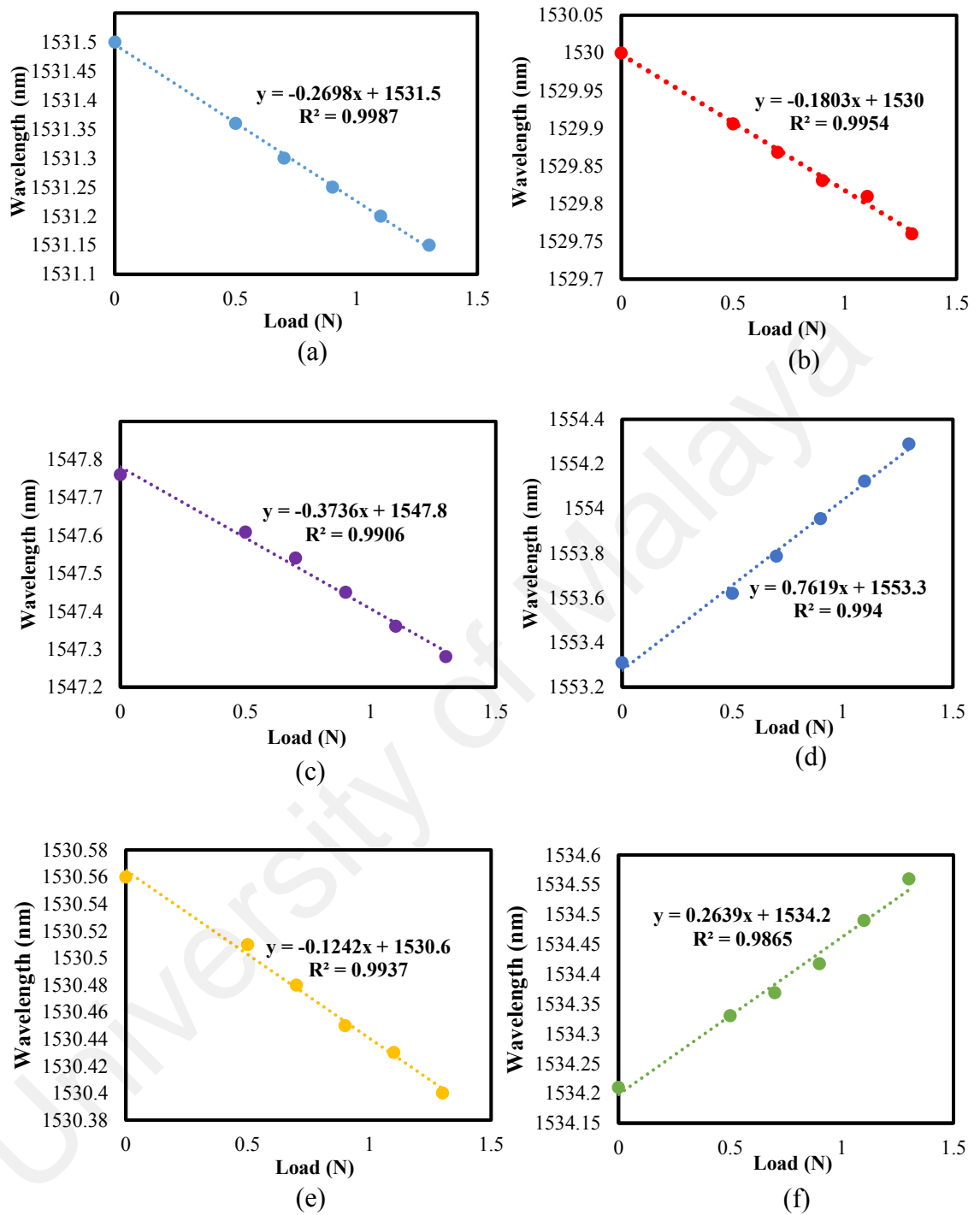


**Figure 3.20: Different load versus to the center crest wavelength of the impedance spectrum for variety L, (a) L=1 cm, (b) L=3 cm, (c) L=5cm, (d) L=7cm, (e) L=9cm, and (f) L=11 cm.**

The 3 dB output spectral bandwidth versus the load at different L length is illustrated in Figure 3.21 which L=5cm, L=7cm and L=9cm shift to a longer wavelength but L=11cm shift to a shorter wavelength. The linearity of the graph is greater than 0.80 with slopes 0.735 nm/N, 1.185 nm/N, 0.21 nm/N, and -0.215 nm/N for L = 5 cm, 7cm, 9cm and 11 cm correspondingly. The shift of the 3dB bandwidth is more obvious for greater length, where L=11cm because of the increment of the phase change.

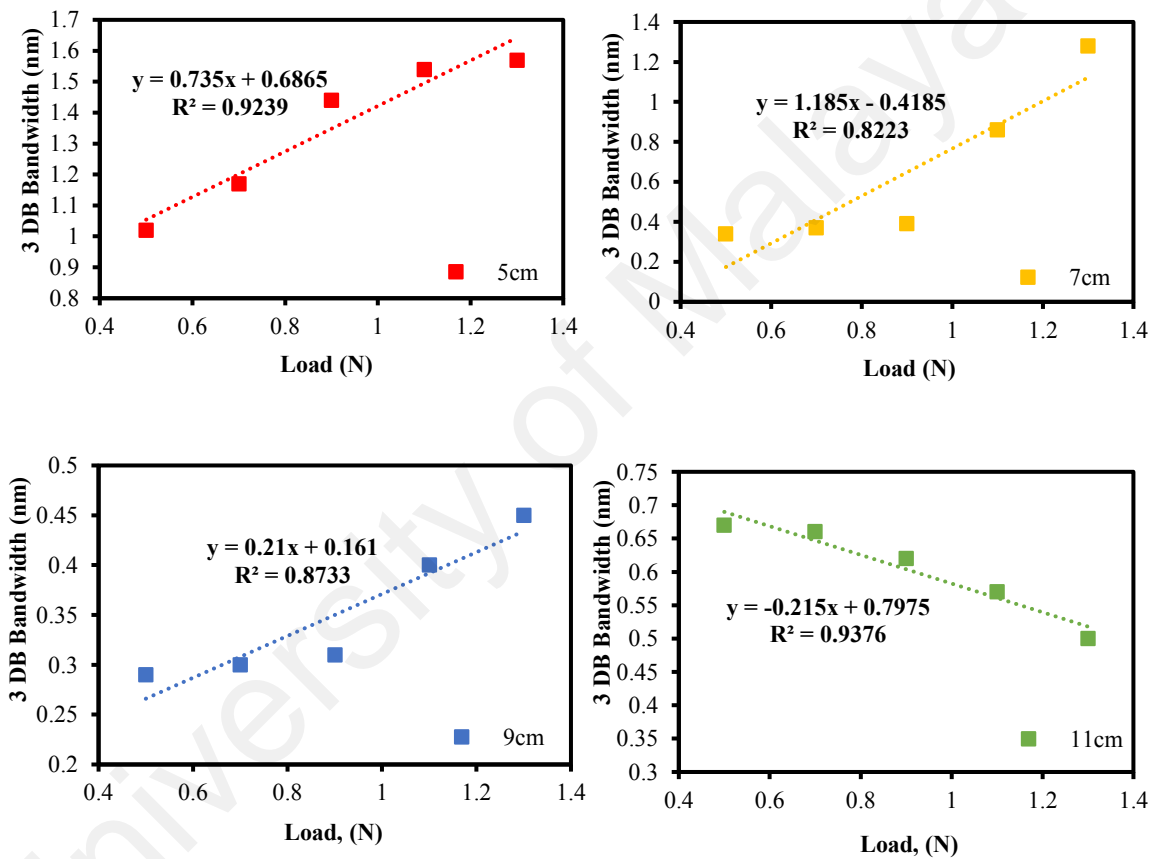


**Figure 3.21: Impedance spectrum of the 3dB bandwidth versus the load volume for (a) L=5cm, (b) L=7cm, (c) L=9cm and (d) L=11cm.**

### 3.5 Summary

In this work, two types of optical sensor probes; microfiber and single mode-multimode-single mode fiber (SMS) structure were successfully fabricated and characterized using a silica optical fiber using a flame brushing and fusion splicing respectively. The non-adiabatic type of microfiber produced a periodic behavior at the output spectrum due to the oscillations as a result of back and forth coupling between core and cladding modes. On the other hand, the SMS structure generates a sufficient bandpass spectral response for a given wavelength range. Both non-adiabatic microfiber and SMS device are capable to be used to demonstrate various sensing applications. The novelty of this research is on the application of the microfiber. This is the first demonstration for structural health monitoring (SHM) application in measurement strain and temperature for steel beam and concrete beam. The comparison for fiber Bragg grating with the conventional fiber Bragg as per (Leng & Asundi, 2003) and (Torres, Payá-Zaforteza Ignacio, Calderón, & Adam, 2011).

From discussion above, each sensing activity, the power will produce a form of graft wavelength, which are different for every trace because each object has a different density that contributes to the shape of the wavelength.

The adiabatic microfiber had perfect tapering shape. This perfect shape of tapered area like a bowl will cause the exposed air molecules in the tapering area to be insulated, which prevents the spectrum inside the fiber refracted outside the fiber. However, in order to be a sensor, the light at the tapering area must be refracted to use as a detector element. Furthermore, non-diabatic offer evanescent field advantages.

## CHAPTER 4

### HIGH TEMPERATURE AND STRAIN MEASUREMENTS

#### 4.1 Introduction

Optical fibers are mainly used as a transmission medium in optical communication. However, beyond telecommunication, they can also be used to construct excellent sensors which can be used to measure physical parameters like strain (Martin, Badcock, Nightingale, & Fernando, 1997), temperature (Barrera, Finazzi, Villatoro, Sales, & Pruneri, 2012), chemical (Ji et al., 2016), and pressure (Roriz, Frazão, Lobo-Ribeiro, Santos, & Simões, 2013). This is attributed to their large bandwidth and low propagation attenuation (Lee, 2003). Compared to conventional mechanical and electrical sensors, the fiber-optic sensors have many advantages including immunity to electromagnetic interference and erosion as well as providing a high sensitivity sensing. Therefore, they can be employed in explosive environment and hazardous places. Up to date, fiber Bragg gratings (FBGs) are widely used for both temperature and strain measurements (Chang & Mehta, 2009; Childers et al., 2001; Ukil, Braendle, & Krippner, 2012). However, the construction of FBG sensors requires photosensitive fibers or hydrogen loading facility and a cumbersome fabrication setup. It also involves working with hazardous gases and annealing treatment after fabrication.

Recently, microfibers have been used in many applications including sensing and lasers (Harun, Lim, Damanhuri, & Ahmad, 2011; Watanabe, Fujiki, & Mukai, 1994; Z. Xu, Luo, Liu, Shum, & Sun, 2017). Besides adiabatic microfibers, a non-adiabatic type with an abrupt change in tapered transition region has also been utilized for sensing applications. The non-adiabaticity promotes the mode coupling between the fundamental of the un-tapered and higher order modes of the microfiber waveguide. The coupling between these modes generate an interference spectrum.

In the microfiber waist, most of the higher order modes propagate at the interface of air-cladding. The large refractive index difference between the glass and air supports more than one mode to co-exist in the microfiber. A periodic behavior is obtained at the output spectrum due to the oscillations as a result of back and forth coupling between these modes (B. Xu et al., 2012).

On the other hand, a singlemode-multimode-singlemode (SMS) fiber structure can also be utilized for sensing as it generates a similar bandpass spectral response (Wu, Muhammad Hatta, Semenova, & Farrell, 2009). It can be employed as an edge filter that interrogates an optical sensor such as in FBG. It is simpler and relatively cheaper to be fabricated compared to the FBG. Therefore, the SMS sensors have been exploited in the past for various sensing applications (Pandey & Yadav, 2006; Wo et al., 2013; Zhao, Huang, He, & Chen, 2010).

In this chapter, temperature and strain sensors are proposed and demonstrated using non-adiabatic microfiber and SMS structure as a probe. The microfiber and SMS devices are fabricated from a silica single mode optical fiber (SMF) using a flame brushing and fusion splicing, respectively as described in the previous chapter. The temperature and strain change the effective refractive index of the core and the cladding modes, and thus induce the resonant spectrum to shift.

## **4.2 High Temperature Sensor**

Figs. 4.1(a) and (b) show the non-adiabatic microfiber and SMS sensor probes, respectively. Both probes were fabricated in house as described in the previous chapter. As shown in Fig. 4.1(a), the fabricated microfiber has a uniform waist with a diameter and length of around 8  $\mu\text{m}$  and 40 mm, respectively. The waist was connected back to the un-tapered fiber by two non-adiabatic, conical transition regions at both ends.

On the other hand, the fabricated SMS structure is shown in Fig. 4.1(b), which was obtained by splicing both ends of a 5 cm long step index multimode fiber (MMF) with standard SMFs. In case of the non-adiabatic microfiber, the incident light signal was splitted into the guided and unguided modes at the input conical region. The guided mode travels inside the core while the unguided mode propagates through the cladding. These multiple modes interfere at the microfiber's waist region to produce a comb spectrum after the conical region. In addition, in the SMS structure, the input light from the SMF excites higher-order modes together with the fundamental mode of the MMF. These modes propagate along the MMF and are subjected to the multimode interference as they recouple at the second splicing point to enter the second SMF.



**Figure 4.1:(a) The non-adiabatic microfiber sensor.**

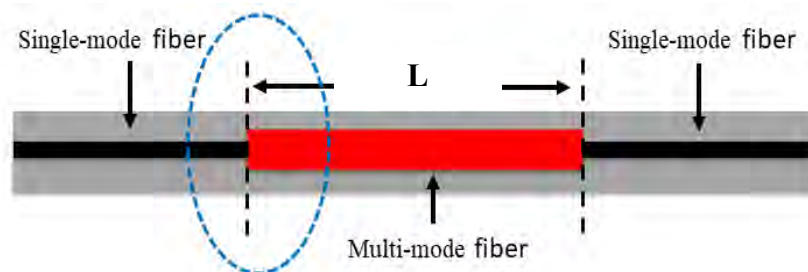


**Figure 4.1: (b) The SMS fiber sensor structure.**

To investigate the shift of the interference spectrum caused by the temperature, the experimental setup was built, as shown in Fig. 4.2. The hot plate was used to control the temperature, while an infrared thermometer was used to measure the temperature change. The fabricated non-adiabatic microfiber and SMS structure were placed onto the hot plate for direct heating with temperature varies in a range from 30°C to 400°C. In this work, the broadband light from ASE source was used in conjunction with an OSA for monitoring the change in the interference spectrum. It is injected at the input end of the sensor probe while the OSA was connected to the output end of the probe.

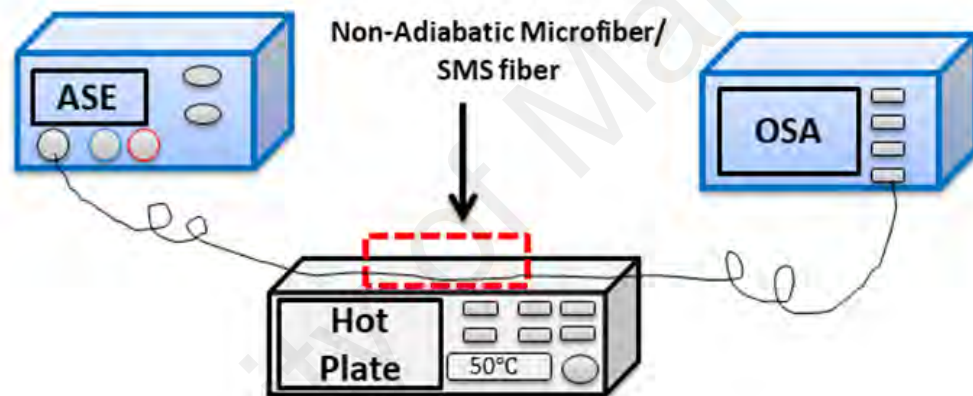


**Figure 4.2: Experimental setup for temperature measurement.**

At first, we recorded the interference spectrum of the non-adiabatic microfiber sensor as we gradually increase the temperature from 40°C to 330°C. Fig. 4.3 illustrates the spectral position of the interference dip at around 1548 nm region at various temperatures. It can be obtained that the wavelength of the interference dip shifts from 1547.12 nm to 1548.80 nm as the temperature rises from 40°C to 330°C. This is most probably due to the heat that changes the effective refractive index disparity between the guided and the unguided modes. It is also noticed that the transmitted power reduces with the rise in temperature.

This is most probably due to the increase in the insertion loss of the microfiber due to the rise in the number of unguided modes propagated through the cladding.

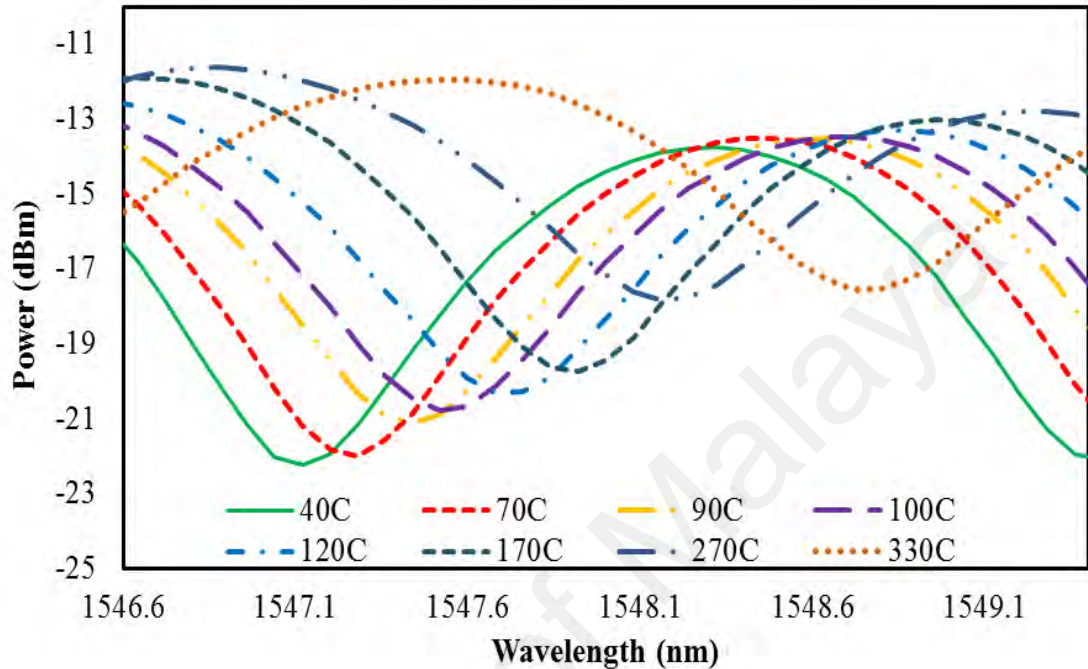


**Figure 4.3.: Output spectra of the non-adiabatic microfiber at various hot plate temperature.**

The SMS sensor sensitivity towards temperature variation was also investigated. Fig. 4.4 shows the experimental result. As expected, the interference fringes is red-shifted to a longer wavelength region as the temperature increased and vice versa. This is attributed to the amount of phase change that varies with respect to the temperature change. Each mode of the MMF propagates with a different fraction of power within the glass material and thus have different thermo-optic coefficients. Furthermore, the MMF was slightly expanded or shrink with the temperature variation. The phase change induced a shift in the transmission dip for the interference fringe as shown in Figure 4.4.

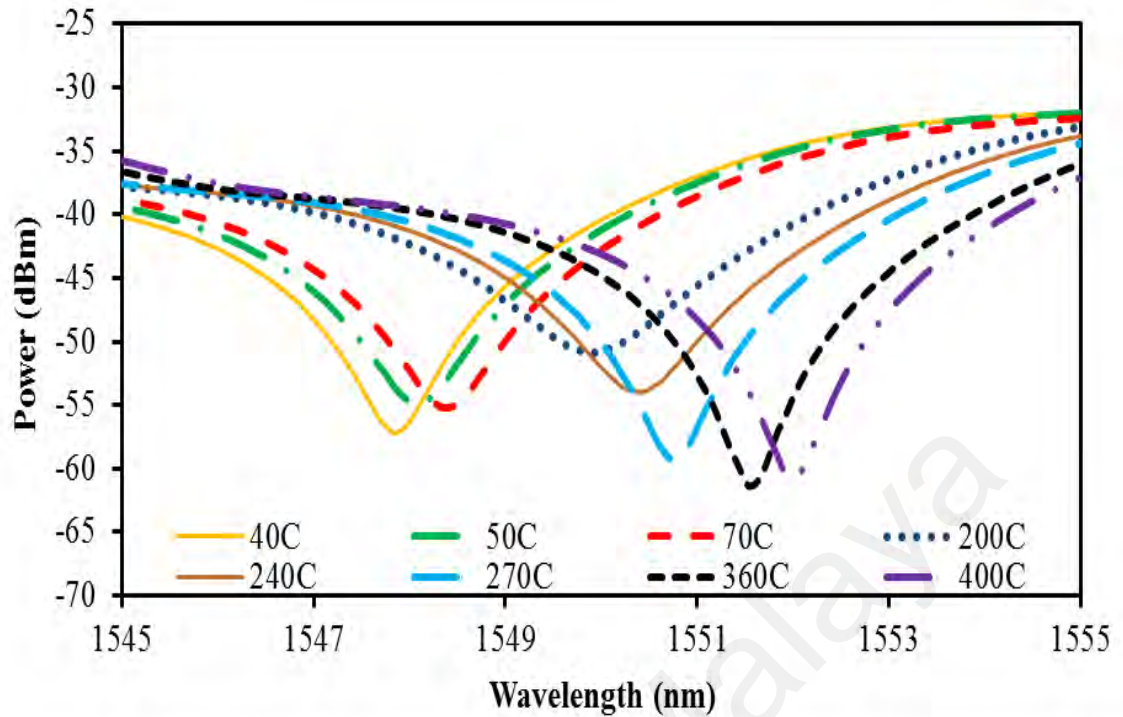


**Figure 4.4.: Output spectra of the SMS structure at various hot plate temperature.**

Figure 4.5 compares the wavelength shift against the temperature for both probes when the temperature were varied from 40°C to 400°C. It can be seen that the linear trend line can be fitted to both experimental data with a linearity of more than 90%. Based on the linear-fitting, the sensitivity of the microfiber and SMS based temperature sensors are 6.0 pm/°C and 11.1 pm/°C, respectively. For the microfiber sensor, the temperature sensitivity was due to the difference in thermo-optic characteristic of the silica core and air cladding. Thus, the effective refractive index of the core and cladding changes differently when the temperature varies. This causes a linear phase shift, which changes the interference fringe as shown in Fig. 4.3.

On the other hand, the SMS structure produces a better result with the temperature sensitivity of about 11.1 pm/°C. The temperature sensitivity was due to the linear phase shifts induced by the core modes of an MMF.

Compared to the microfiber sensor, the SMS structure produces a larger effective index difference, which results in the larger phase change with respect to temperature. The sensor probe was also tested during the ramp-up and cool-down operations. It was left at 400°C for 3 hours before the temperature was decreasing gradually. The sensitivity deviation during the temperature ramp-up and cool-down was observed to be lower than 5%. Improvement in either the determination of the interference dip and the temperature accuracy of the hot plate could further improve the temperature sensitivity result.

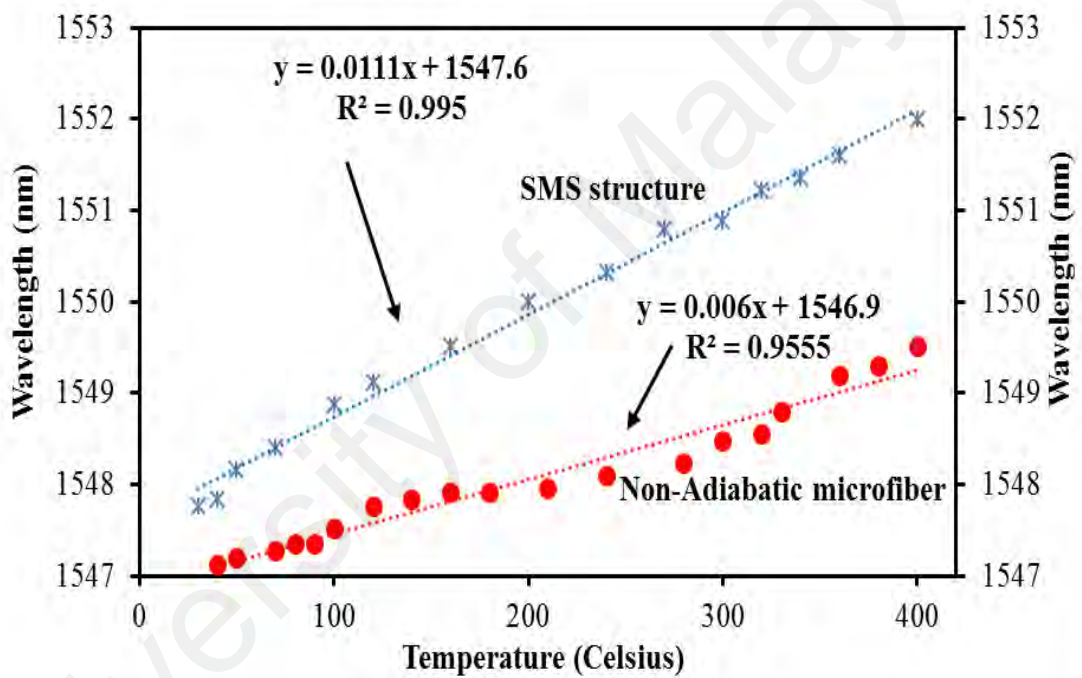
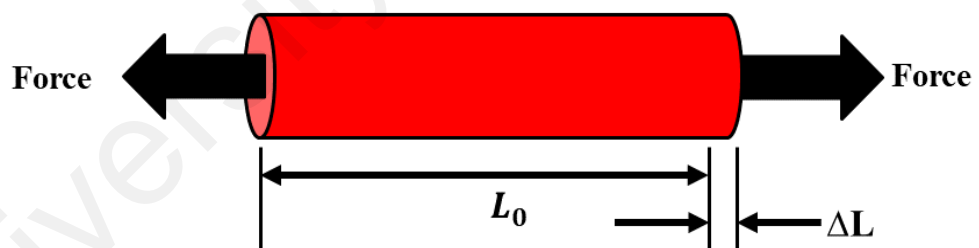


**Figure 4.5: Relationship of the interference spectrum output against the temperature for SMS fiber and non-adiabatic silica microfiber.**

### 4.3 Strain Measurement

Applied stress is significantly influenced by a strain. Once a material is applied with a force, it generates a pressure, consequently deformation occurs at that material. Hence, the value of deformation towards the applied stress that separated by the material's original length can be classified as an engineering strain.

The response towards applied force is shown in unitless digit with unsimplified form either in meter/meter or in inch/inch. In detail, as portrayed in Figure 4.6, the strain is the volume of the elongation as the bar being pulled in tension or length variation which divided by the initial length. Therefore, the strain dissemination could conceivably be uniform in a complex auxiliary component, rely upon the loading features condition. For example, with the condition of small quantity load applied, the small strain occurred at that material and it will come back to its initial size after the pressure is unforced. The changes that the material experience is named as an elastic deformation, which precisely described as elastic phenomena which means the material is going back to its original state condition. Elastic deformation only occurs in a material when stresses is lower than a critical stress called the yield strength. However, if the material is stretched beyond it's elastic limit, even the material or bar is in unstress state, it will remain in a deformed condition. This phenomena is called as a plastic deformation.



$$\textit{Strain} = \frac{\textit{Elongation}}{\textit{Original Length}} = \frac{\Delta L}{L_0}$$

**Figure 4.6: Strain measurement of the structure.**

Now days, advanced concrete and composite structures are now broadly applied in civil engineering, ships, aerospace and marine industry, and modern transportation. Subjected to the loading condition, the position and the strain's extent play significant role to interpret and recognize their characteristic.

As of late, a great deal of intrigue has been made for strain sensor which used optic fiber because it is capable to gives on-site and real-time output data. Henceforward, this advanced structure is most appropriate to utilize fiber optic technology for structural health monitoring purposes, as they are compact, responsive, sensitive, stable and resistant to electromagnetic interference (Güemes, Fernández-López, Díaz-Maroto, Lozano, & Sierra-Perez, 2018)(Bremer et al., 2016)(Di Sante, 2015)(Ansari, 1997) [1-3]. To date, various fiber optic sensors have been proposed for measuring strain in different structures and beams. For instance, FBGs have been widely employed to evaluate strain value for beams and composite structures (Guo et al., 2018)(Yazdizadeh, Marzouk, & Hadianfard, 2017)(Leng & Asundi, 2003). This is attributed to the measurements that are independent of source intensities and losses in the system. However, the grating writing is slightly complex where the proficiency relies upon the authority of centralize at optical bars. of optical beams. Fiber sensors based on Brillouin scattering have also been the focus of great attention for measuring strain distribution in cantilever beams(Drake, Sullivan, & Wilson, 2018)(Minakuchi et al., 2011)(Bernini, Minardo, Testa, & Zeni, 2010)(Zeng et al., 2002). Later, the location and strain value might be resolved for a beam to where a concentrated load is placed by investigated the Brillouin back-scattered light power spectrum.

On the other hand, the multimode interference (MMI) theory has been widely demonstrated and recommended as an essential foundation for various unique fiber sensors like beam splitters, combiners, multiplexers for optical communications, comb filters and fiber sensors (Wang, Zhao, Wang, Farrell, & Brambilla, 2018)(Hertz et al., 1994) (Ferrerias, Rodríguez, Gómez-Salas, De Miguel, & Hernández-Gil, 1993). In the previous section, the multimode interference in a non-adiabatic microfiber and SMS fiber structure have also been explored and established for high temperature sensing. In this section, the modal interference in both devices is demonstrated for measuring strain.

The non-adiabaticity promotes the mode coupling between the fundamental of the un-tapered and higher order modes of the microfiber waveguide. The coupling between these modes generates an interference spectrum. On the other hand, the SMS structure generates a sufficient bandpass spectral response for a given wavelength range. Both optical sensors dependent on multimode interference attempt all-fiber resolutions the ease of packaging and connection advantages for optical sensing purposes to the to optical fiber system.

Here, the performance of two fiber-optic based strain sensors based on non-adiabatic microfiber and SMS structure probes are compared. The microfiber and SMS devices were fabricated from a silica single mode optical fiber (SMF) using a flame brushing and fusion splicing, respectively as described in Chapter 3. The fabricated microfiber has a waist with a diameter and length of around 60  $\mu\text{m}$  and 30 mm, respectively. The waist was connected back to the un-tapered fiber by two non-adiabatic, conical transition regions at both ends. On the other hand, the SMS structure was constructed by splicing both ends of a step index multimode fiber (MMF) with standard SMFs. The experimental setup for strain measurement was built, as shown in Fig. 4.7. Both ends of the sensor probes were glued to a fixed stage to avoid slip. Then the stage is clamped to the Instron 5582 static machine clamp.

The distance between the stages where the glue was inserted was 7 cm. In order to observe the spectral response of non-adiabatic and SMS probes, an interrogator system based on Erbium amplified spontaneous emission (ASE) source was used to transmit the light along the probe. The strain value was controlled by setting the speed of the machine in millimetres per second unit. The established speed was required to avoid machine error or the fiber reached the breaking point too fast. In this setup, we applied 0.1 millimetres per second speed. The reading was measured for each 0.5 N strain.

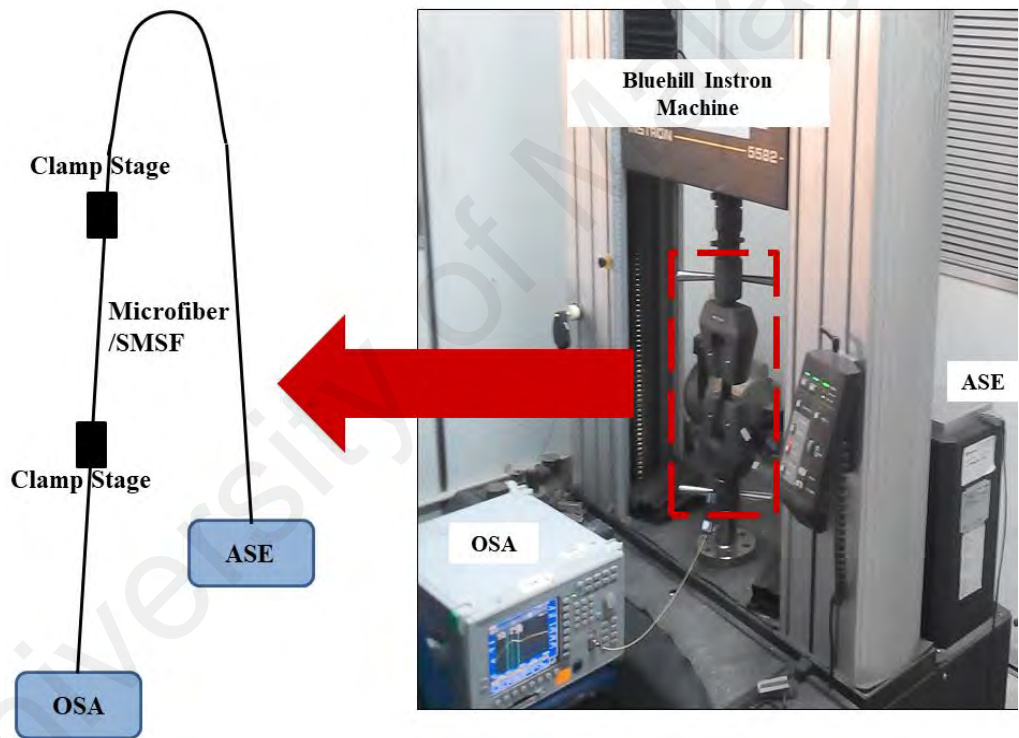


**Figure 4.7: Schematic diagram of the strain test.**

#### **4.3.1 Strain Measurement with Non-adiabatic Microfiber**

In case of the non-adiabatic microfiber, the incident light signal was being split into the guided and unguided modes at the input conical region. The guided mode travels inside the core while the unguided mode propagates through the cladding.

These multiple modes interfere at the microfiber's waist region to produce a comb spectrum after the conical region. The operation of the microfiber is based on a modal interferometer, which the transmission criterion was defined as (Mignani, Falciai, & Ciaccheri, 1998):

$$I = I_1 + I_2 + 2\sqrt{I_1 I_2} \cos(\Delta\phi) \quad (4.1)$$

where  $I$  is the intensity of the inference signal,  $I_1$  and  $I_2$  are the intensity of the light circulating in the core fundamental mode and higher-order modes respectively and  $\Delta\phi$  is the phase difference between the impedance modes which is relatively equivalent to:

$$\Delta\phi = \left( \frac{2\pi(\Delta n_{eff})L}{\lambda} \right) \quad (4.2)$$

Here,  $L$  is the taper waist region of microfiber,  $\Delta n_{eff}$  is the variance of the effective refractive indices of the core and the cladding modes and  $\lambda$  is the light source's wavelength. The fringe spacing between the two inference patterns is defined as

$$\Delta\lambda = \frac{\lambda_0^2}{(\Delta n_{eff})L} \quad (4.3)$$

Any variations in Equation (4.3) would force changes in spectral output. For example, if the strain applied to the fiber change, it would prompt a shift in the output spectrum as the distinction in engendering constants and the relative phase between different modes change. Fig. 4.8 illustrates the recorded interference spectra of silica microfiber at around 1530 nm wavelength region as strain increases up to 1.3 N. It can be observed that the peak is shifted to the shorter wavelength from 1530.2 nm to 1528.08 nm as the strain load rises from 0.0 N to 1.3 N.

This is associated to the applied strain that navigated the increase of the core's refractive index and as well as the interaction length along the microfiber. Wherefore, this led to the fringe spacing reduction of the output spectral as well as shifts the peak spectrum headed to a shorter wavelength domain. In addition, immediately upon the strain is detached from the device, the peak restored to its initial position. Figure 4.9 displays the peak wavelength and the extension against strain load, which show the linear trend line can be fitted to the experimental data with a correlation coefficient values of  $r > 93$  and  $r > 0.98$  respectively. Maximum extension at break is 1.85mm while tensile strain at break is 2.64 mm/mm.

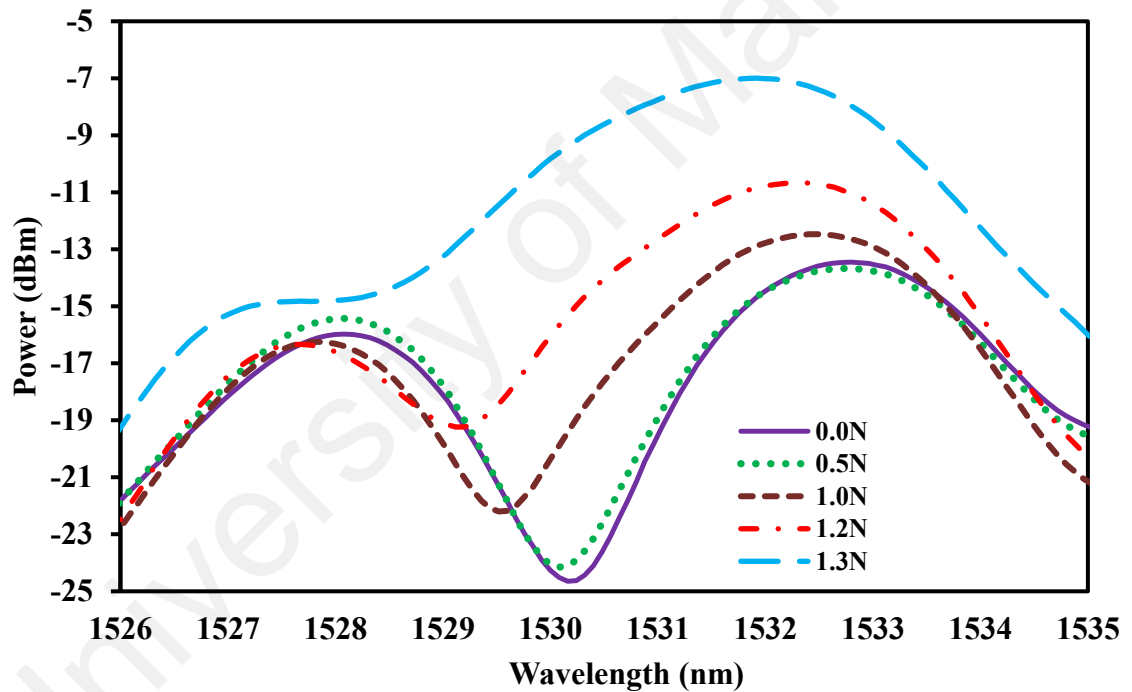


**Figure 4.8: Spectral response output from the microfiber structure at different strain.**

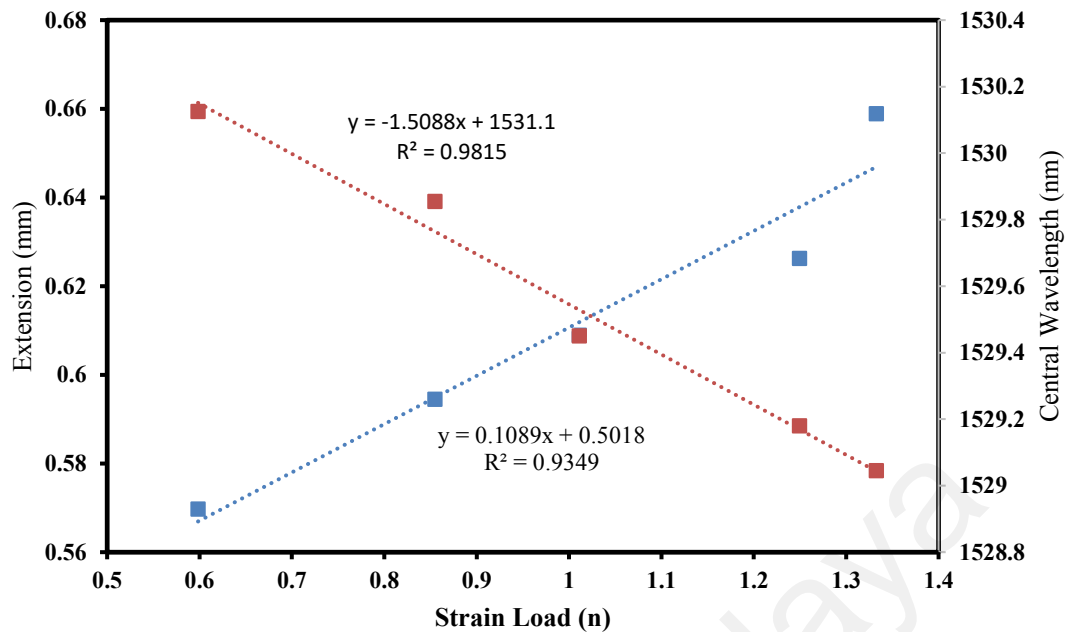


**Figure 4.9: Central wavelength and displacement of microfiber against strain.**

#### 4.3.2 Strain Measurement with SMS Sensor

Other than microfiber, the SMS structure was also utilized in this study to assess its affectability against strain deviation. Figure 4.10 shows the output spectrum of the SMS sensor configured at various strain. As shown in the figure, as well as the strain increased, the interference fringes were discovered to shift to shorter wavelengths. This is attributed to the amount of phase change that varies subjected to the strain variation. As known, every mode proliferates along MMF had different fraction of power within the glass material. In this manner, the strain coefficients will differ. Other than this, it is also due to the the fact that, the MMF expands and shrinks in small scale as strain change. Figure 4.11 shows the peak wavelength and the extension against strain load, which show the linear trend line can be fitted to the experimental data with a correlation coefficient values of  $r > 99$  and  $r > 0.97$  respectively. Maximum extension at break is 0.61 mm while tensile strain at break is 0.00869 mm/mm.

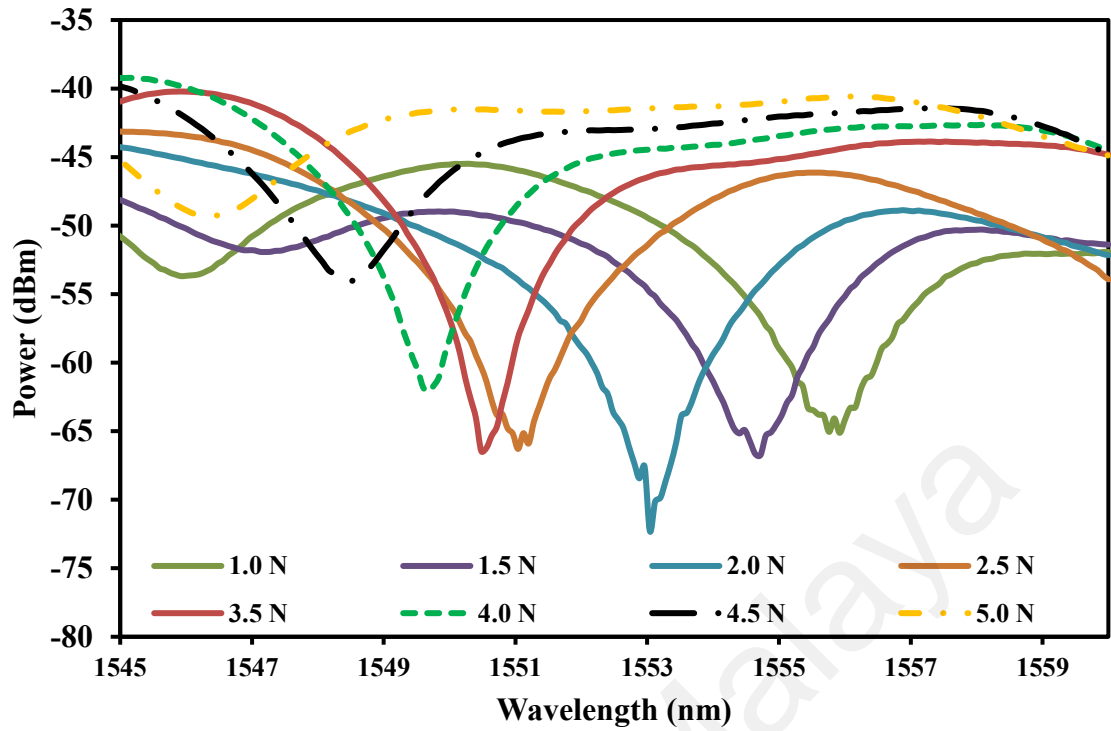


Figure 4.10: Spectral response output from the SMS fiber structure at different strain values.

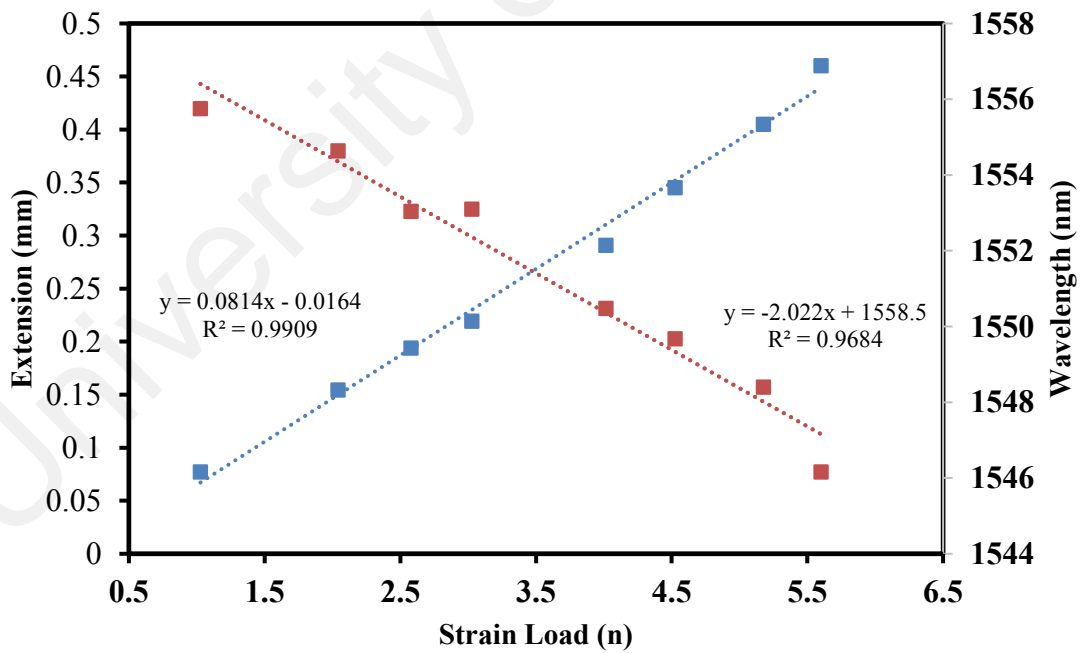
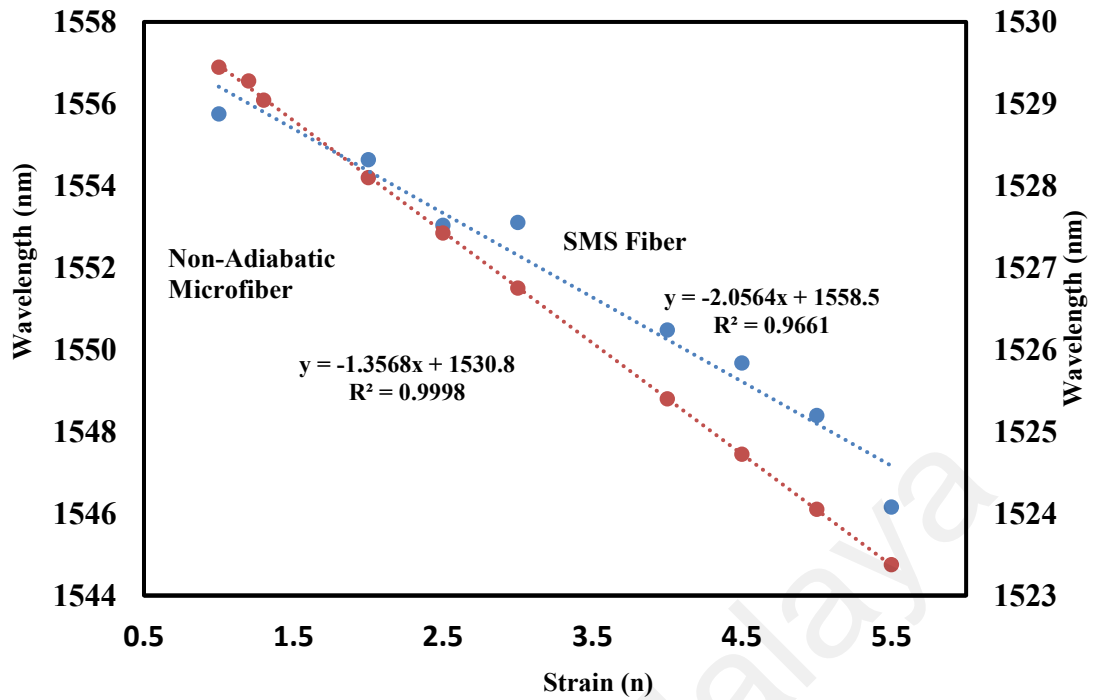


Figure 4.11: Central wavelength and displacement of microfiber against strain.

### 4.3.3 Performance Comparison

Figure 4.12 compares the wavelength shift of both probes versus the different strain. It can be seen that the linear trend line can be fitted to both experimental data with a linearity of more than 96%. Linear-fitting of the experimental data shows that the strain sensitivity of the microfiber and the SMS based sensors are -1.36 nm/n and -2.06 nm/n respectively. The strain sensitivity of the nonadiabatic microfiber sensor was ascribed to the variation in strain-optic reliance upon to the fundamental fiber and air cladding. Over and above, as the strain increase, the effective refractive index of the core and cladding change differently, which triggering a linear phase shift of the interference fringe. On the other hand, the microfiber structure produces a better result with the strain sensitivity of about -1.36 nm/n. This is a typical strain sensitivity for an interference sensor involving core modes and higher order modes. It has been shown that the sensitivity sensor influenced by the difference of effective refractive indices between fundamental core mode  $HE_{11}$  and its closest higher order mode  $HE_{12}$ .

This implies that the nonadiabatic silica microfiber sensor produces a greater effective refractive index difference, which resulting in the larger  $\Delta\theta$  phase difference with respect to strain. The outputs were relatively reproducible as the test was repeated a few times.



**Figure 4.12: Wavelength interference spectrum relationship between non-adiabatic microfiber and SMS fiber against the strain.**

#### 4.4 Summary

Temperature and strain sensors were successfully demonstrated using non-adiabatic microfiber and SMS structure as a probe. Interference fringes of the output red-shifted as the temperature increased due to the change in the effective refractive index of the multiple modes inside both structures. The proposed microfiber and SMS sensors were shown to be able to measure temperature stably up to 400°C with sensitivities of 6.0 pm/°C and 11.1 pm/°C, respectively. The non-adiabatic microfiber and the SMS optical fiber probes were also established for strain measurements. A total wavelength shift for a non-adiabatic silica microfiber and a SMS fiber device were 1.08 nm and 9.6 nm respectively. Therefore, the strain sensitivity of the microfiber measured to be -1.36 nm/n while the SMS optical fiber was -2.06 nm/n with a linearity of more than 0.99 and 0.97. Both sensor designs are simple and thus they can be mass-produced with a relatively low cost.

## CHAPTER 5

### STEEL BEAM AND CONCRETE BEAM COMPRESSIVE STRAIN MEASUREMENTS

#### 5.1 Introduction

One of the applications for fiber optic sensors that has drawn great interest is in the area of structural health monitoring (SHM). Fiber optic sensors are well known for durability, superior stability, insensitivity to electromagnetic (EM) interference, long-distance sensing operation, tolerance of high temperature operation and networking ability (Fernandez-Vallejo & Lopez-Amo, 2012) , In SHM, fiber optic sensors have been used for monitoring the safety and health of composite materials (Mehryar & Esmaili, 2011), vast structural designing structures (Bertelli et al., 2010) and quantitative substance process (Tong & Sumetsky, 2011).

A number of fiber inline interferometric sensors have already been proposed and developed in the forms of Mach–Zehnder interferometers (MZIs) based on photonic crystal fibers (PCFs) (Brambilla.G, 2010), long-period fiber gratings (LPFGs) (Brambilla et al., 2009) , and Fabry–Perot interferometers based on air cavity (Wu & Tong, 2013). Such interferometric sensors are expensive to build and large in dimension. Of late, cheaper and smaller fiber inline interferometric sensors have been demonstrated utilizing microfibers and single mode multimode single mode fiber structure (Huang et al., 2017; Kou et al., 2012; Xiang et al., 2018; Xie, Zhang, Wang, & Wang, 2018; Zhu, Wu, Liu, & Duan, 2012).

In this chapter, non-adiabatic microfiber and SMS structures are proposed to measure compressive strain of both steel and concrete beams. Both techniques offer the advantages of a much simpler configuration, ease of fabrication, wide measurement range and high resolution compared to the conventional optical sensor based on fiber Bragg grating (Jasim, Harun, Arof, & Ahmad, 2012; Li, Jiang, Wang, Mengmeng Wang, & Yang, 2012; Muhammad, Jasim, Ahmad, Arof, & Harun, 2013; Smietana, Brabant, Bock, Mikulic, & Eftimov, 2012). Moreover, to validate the experimental data, parallel measurements are made along the beam with an electrical resistance (ER) based strain gauge for comparison.

## **5.2 Optical Non-Adiabatic Silica Microfiber for Steel Beam Compressive Strain Measurement**

Microfibers have been used in a wide range of applications as well as sensing and lasers area (Bidin et al., 2016; N.Hida, N.Bidin, M.Abdullah, & M.Yasin, 2013; Sivakesava & Irudayaraj, 2001) Other than adiabatic microfiber, a non-adiabatic type with an abrupt change in taper angle that advances the coupling between the basic and higher order modes has likewise been used for sensing applications field. The coupling occurs primarily between the fundamental mode of the un-tapered fiber and the first two modes of the microfiber waveguides ( $LP_{01}$ ,  $LP_{02}$ ), where due to the large difference of the refractive indices of air and glass, the microfiber normally supports more than one mode. The light propagates at the air-cladding interface of the microfiber's waist region, in which case the single-mode fiber (SMF) is converted to a multimode fiber (MMF). The result of back and forth coupling between the single mode of the fiber and the two (or more) modes of the microfiber is oscillations in the spectral response of the microfiber, which results in the transmission versus wavelength showing a periodic behavior as described in Chapter 3.

In this section, a non-adiabatic microfiber structure is proposed and demonstrated as a sensor to measure compressive strain of a steel beam. The proposed microfiber sensor is able to measure a compression strain on a steel beam up to the elastic limit of the beam at 130 kN. The elastic limit of a steel beam is the last load value under which the beam deforms elastically and then returns to its original dimension or shape when the load is removed. When subjected to a load beyond its elastic limit, the beam will have a permanent deform and it is marked as a complete failure (E.E.H.Love, 1906; Reiner, 2017).

### **5.2.1 Experimental Arrangement**

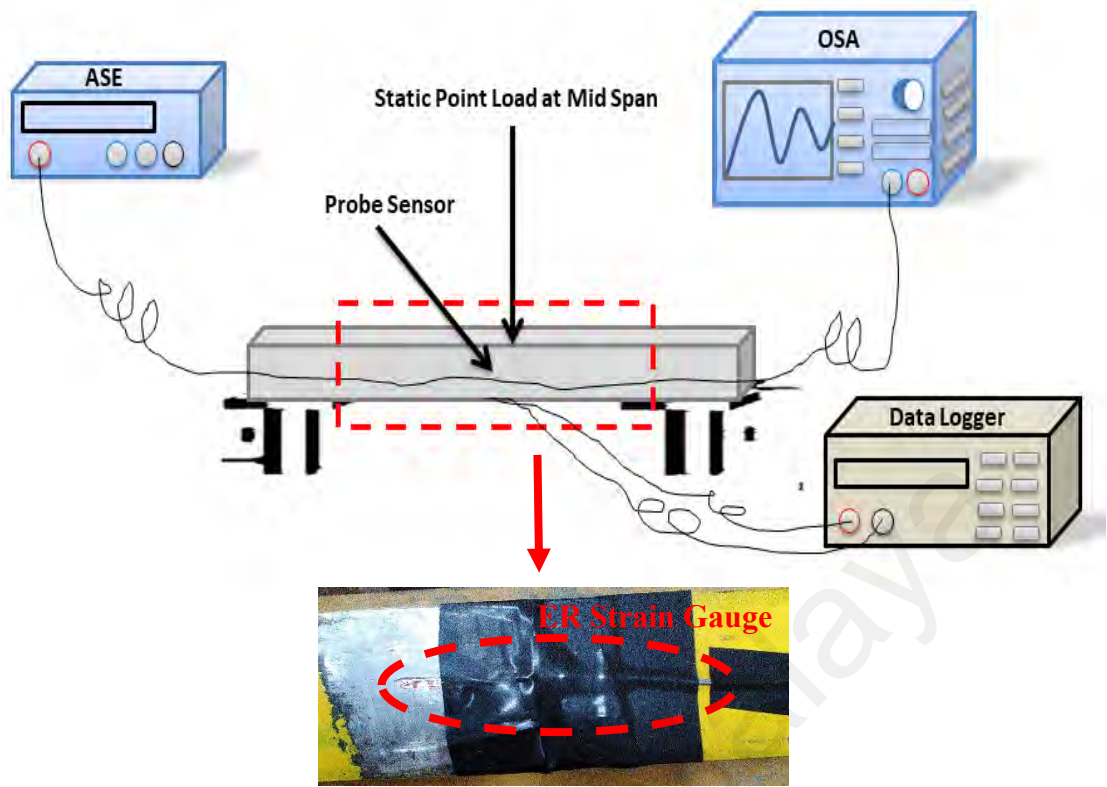
The experimental setup for measuring the steel beam elastic limit using the proposed compressive strain sensor is shown in Figure 5.1 (a). An Instron universal testing machine with a 600kN static load capacity is used to apply the compressive load at the center of the 0.85 m long steel beam (Universal Beam 150). The lower ends of the beam are supported by two fixed roller bearings, as shown in Figure 5.1(b). The distance between the two bearings is around 0.8 m. The strain sensor is placed on the top surface of the lower flange of the mid-span steel beam using a superglue or cyanoacrylate adhesive as shows in Figure 5.1(a). An adhesive tape is used to cover the top part of the sensor. An ER strain gauge is also placed close to the fiber sensor and a data logger is connected to the ER strain gauge to read and record the strain values.

The optical strain sensor was constructed from a standard single mode fiber (SMF) normally used for telecommunication as described in Chapter 3 in detail. A fused non-adiabatic microfiber was fabricated from a bare SMF with a diameter of 125  $\mu\text{m}$ . A small section of the SMF was heated and stretched to reduce its diameter. Computer-controlled stepper motor stages were used to stretch the target section while brushing it with heat from a butane-oxy flame.

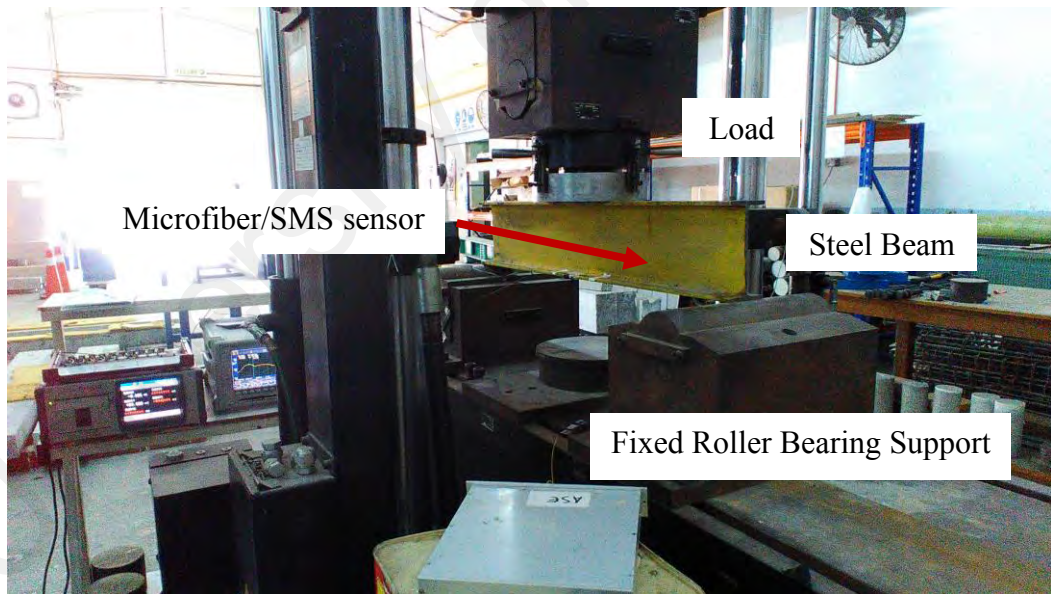
The resulting microfiber had a final diameter of around 8  $\mu\text{m}$  over a length of about 40 mm and was connected to the un-tapered fiber via non-adiabatic, conical transition regions at both ends. The non-adiabatic silica microfiber structure was then attached to the flange steel beam in a similar fashion. The sensor is aligned to be perpendicular with the position of the load cell, as shown in the Figure 5.1(b). An amplified spontaneous emission (ASE) source operating at 1550 nm wavelength was used as a light source while an optical spectrum analyzer (OSA, Aritsu MS9710C) was used to capture the spectral change at the output of the sensor as shown in Figure 5.1(a). A force of 20kN was initially applied on the beam and the load was gradually increased at the Instron speed rate of 1.5 kN/min until it reached the elastic limit of the beam. The ER strain gauge and the microfiber sensor measurements were simultaneously recorded for comparison. The experiment was conducted at room temperature (at around 26 °C) in an enclosed building. Readings were taken after each 5kN compressive load increment. The elastic limit of the steel beam can be estimated by

$$P = \frac{4M_{max}}{L} \quad (5.1)$$

where P is the yield load,  $M_{max}$  is the maximum bending moment and L is the distance between supports. Since the steel beam has the estimated maximum bending moment,  $M_{max}$  of 31625 Nm and the distance between the two fixed bearings is 0.8 m, it is expected to reach its elastic limit at a compressive load of around 158 kN. The steel beam is a mild steel beam with  $2.1 \times 10^{10}$  kg/m of modulus of elasticity and Poisson's ratio 0.2. Figure 5.1(c) shows the image of the steel beam after failure test.



(a)



(b)



(c)

**Figure 5.1: Schematic diagram of the compressive test (a) Schematic illustration (b) Image (c) Image of the steel beam after failure test.**

### **5.2.2 Non-Adiabatic Silica Microfiber Sensor Performance with Steel Beam**

The output comb spectrum from the non-adiabatic microfiber structure at 20 kN load is shown in Figure 5.2. As the ASE light is launched into the microfiber, it splits into two portions at the input conical region, which are the guided and unguided modes. The guided mode keeps travelling in the core and the unguided mode propagates through the cladding. Interference between the multiple modes of the microfiber's waist region produces a comb spectrum at the output end of the conical region. As shown in Figure 5.2, the microfiber structure has a bandpass spectral response with its peak to peak spacing of around 3.5 nm. This shape characteristic of the spectrum depends highly on the interference between the light modes that propagate along the tapered area. In this experiment, the length of the tapered section is about 40 mm. The steel beam is bent along the tapered section of the microfiber device when the compressive load is applied.

As a consequence, the relative phase difference between the propagation modes changes due to the non-symmetrical refractive index distribution of the tapered area when the fiber is bent. This causes shift in the interference position and the change in the output spectrum from the microfiber.

The length and diameter of the microfiber significantly influence the interference characteristic of the microfiber. As the length of microfiber increases, the number of spatial mode beating in the MMF increases and thus the transmission spectrum comb pattern will become more prominent. However, from our observation, this does not significantly influence the sensitivity of the sensor. The thermal stability of the sensor is high since the temperature sensitivity of the sensor is measured to be around 12.1 pm/°C.

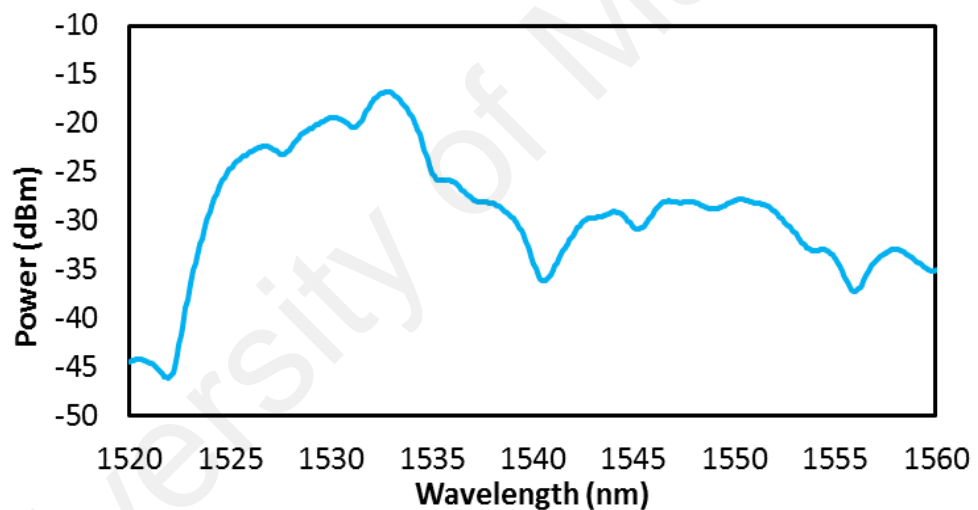


**Figure 5.2: Non-adiabatic silica microfiber bandpass output spectrum at 20kN compressive load.**

Figure 5.3 shows the peak spectral change at different loading measured at OSA resolution of 0.05 nm and span of 3.5 nm. Inset of Figure 5.3 shows a spectral change at a bigger span from 1520 to 1560 nm. The bend in the tapered section has a significant influence on the mode distribution in the microfiber structure, which in return will have a profound effect on the overall transmission characteristics of the microfiber structure.

It can be inferred from the figure that the peak wavelength of the interference comb spectrum shifts to a longer wavelength as the load grows from 20 kN to 130 kN as shown in Figure 5.3. This is attributed to the applied strain which change both of the refractive index of the core as well as the interaction length along the microfiber. This in return changes the fringe spacing of the output spectral and shifts the peak spectrum towards a longer wavelength region as shown in Figure 5.3. When the strain is removed from the sensor, the peak returns to its original position. It is observed that the pattern of the interference spectrum completely changes as the load increases from 20 to 130 kN as shown in the inset figure.

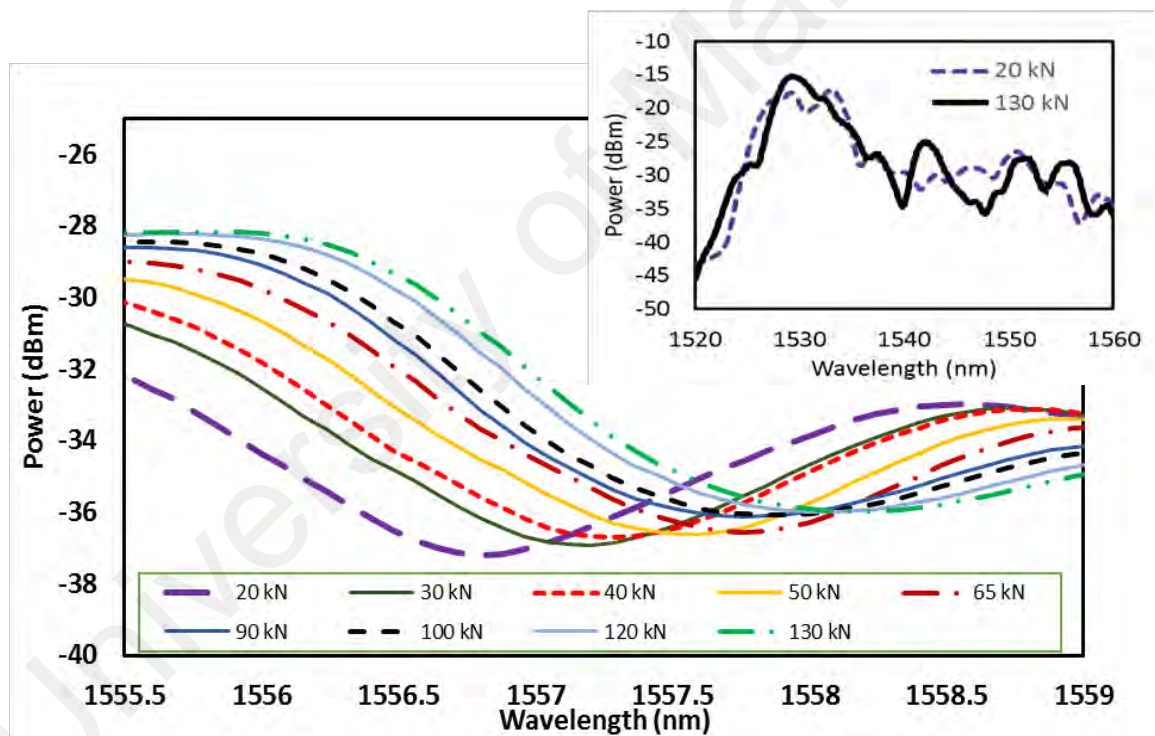


**Figure 5.3: Spectral response output from the non-adiabatic silica microfiber structure at different compressive load within a span of 3.5 nm. Inset shows the spectra within a larger span of 30 nm.**

The ER based compression strain and the peak of interference wavelength were also measured using a data logger and OSA, respectively for various loads and the results are summarized in Figure 5.4. At the initial load of 20 kN, the ER strain gauge and OSA show a compressive strain of 1.567 mm/mm and peak center wavelength of 1570.00 nm, respectively. As the load is increased, the compression strain linearly increases and the peak wavelength shifts to a longer wavelength. A total wavelength shift of 1.04 nm is obtained with a sensitivity of 0.0094 nm/kN as the load is increased from 20 to 130 kN. Above the 130 kN loading, the compressive strain shows a radical change to a higher value with a compressive strain of 9.839 mm/mm that is obtained from the maximum load of 143 kN. The peak center wavelength curve has also a radical change to a shorter wavelength as the compression load is increased above 130 kN. The increased change in compressive strain slope and the wavelength shift pattern above 130 kN indicates the radical change in the mechanical property of the steel beam. This elastic mode limit is close to the predicted load amount of 158 kN.

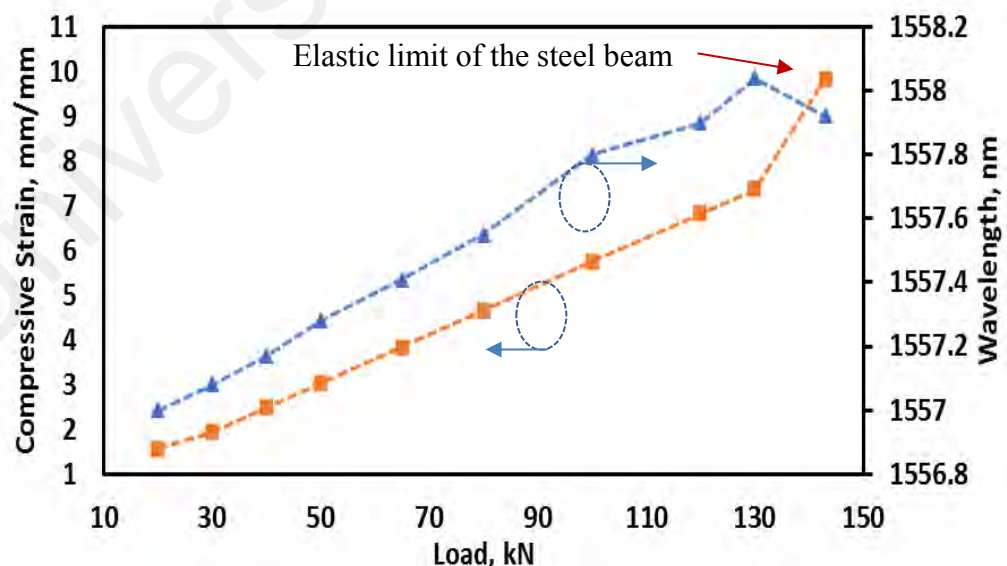


**Figure 5.4: Compressive strain and peak center wavelength at different amount of compressive load.**

Figure 5.5 shows the relationship between the spectral wavelength and the compressive strain. It exhibits a linear curve with a slope of 0.1766 nm/(mm/mm) and linearity of more than 99% before the elastic limit of the steel beam is achieved. From 130 kN to 143 kN of compressive load, the beam experiences a significant increase of the compressive strain from 7.370 to 9.839 mm/mm. The large change in the strain as compared to any other transition of loading, is due to the weakened strength and rigidity of the beam. Beyond this load, the beam exceeds its linear characteristic of modulus of elasticity, hence a drastic change of strain was experienced by the beam. This is in good agreement with the observation in Figure 5.4, where the large change of strain is reflected by the large change of wavelength shift. Below the elastic limit, the wavelength shift is well matched to the applied load which prove that the non-adiabatic sensor is able to measure the steel beam compressive strain with good sensitivity and linearity.

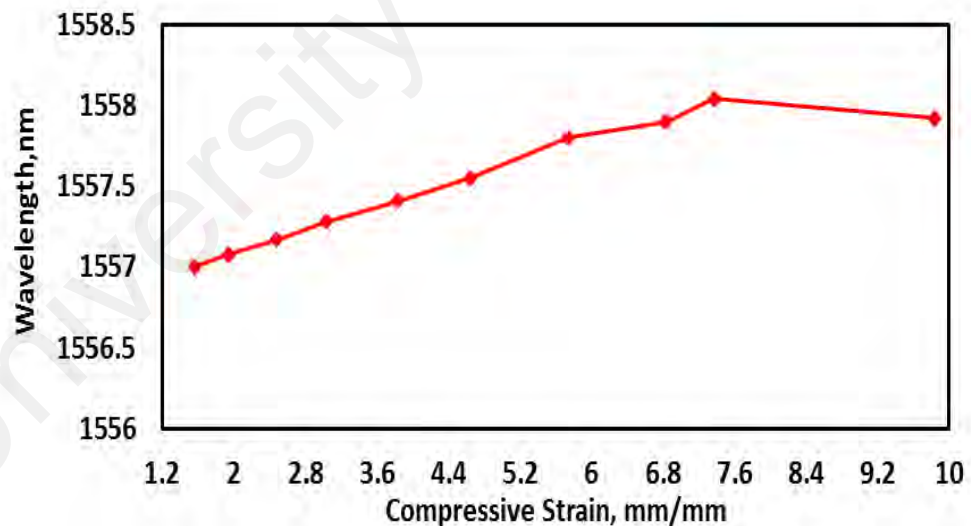


**Figure 5.5: Spectral wavelength shift with the compressive strain.**

### 5.3 SMS Sensor for Steel Beam Compressive Strain Measurement

As discussed earlier, fiber inline interferometric sensors have gained attention in recent years due to their ease of fabrication, compactness, and high sensitivity for the measurement of various physical parameters such as temperature and strain. In the previous chapter, the single-mode-multimode-single-mode fiber (SMS) structure was demonstrated for temperature sensing. Many works have also been reported in literatures on the SMS structure-based sensors (Ian et al., 2017; Ruiz-Pérez, Basurto-Pensado, LiKamWa, Sánchez-Mondragón, & May-Arrijoja, 2011; Xiang et al., 2018; Zhang et al., 2014). For instance, Zhang et al. reported a theoretical and experimental results on refractive index (RI) sensing based on the multimode interference in SMS structure (Zhang et al., 2014). In this section, an SMS fiber structure is proposed and demonstrated to measure compressive strain of a steel beam.

The compressive strain measurement on a steel beam using the proposed SMS fiber sensor was conducted using the similar setup as Figure 5.1. In this work, a 0.83 m long steel beam with a section depth of 150 mm and a flange width of 75 mm (Universal Beam 150) was used. The compressive load from an Instron universal testing machine was placed at the center of the beam. The distance between the two bearings was also fixed at around 0.8 m. The SMS fiber structure was fabricated by splicing both sides of a multimode fiber (MMF) with two standard single mode fibers (SMFs) using a commercial fusion splicer. The length of the MMF was about 7 cm and it has a step index profile with a core/cladding diameter of 105/125  $\mu\text{m}$ . The SMF has a core diameter of 9  $\mu\text{m}$ . The light infused into the MMF will energize numerous modes while a single mode fiber will only excite one mode. Therefore, the SMS structure will produce a multimode interference, which can be used for measuring the strain. The SMS structure and ER gauge were fixed to the flange steel beam with a similar location and approach as described in the previous section.

An ASE source operating at 1550 nm wavelength band was utilized as a light source while an OSA was used to capture the output spectral change of the sensor. Initially, a load cell of 10 kN is applied on the steel beam. Then the load is gradually increased at the rate of 1.5 kN/min until it reaches the elastic limit. The ER strain gauge and the SMS sensor measurements are simultaneously recorded for comparison. The experiment was conducted in an encased building while the temperature was controlled at 27°C. The compressive load was increased in step of 5 kN and the output for each load level was measured accordingly.

Figure 5.6 shows the output comb spectrum from the SMS fiber structure at 40 kN compressive load. The output spectrum indicates that the SMS fiber structure has a bandpass spectral response with its peak at around 1532 nm wavelength range. The bandpass reaction is a response of multimode interference and recoupling inside the SMS fiber structure. As monitored, the comb spectrum range has a top to-crest dispersing of around 5 nm. This profile characteristic build upon highly on the interference between the light modes that circulate in the MMF section of the SMS. The steel beam is bent along the MMF section of the SMS device once the compressive load is enforced. Significantly, when the fiber is bent, due to the non-symmetrical refractive index dispersed in the MMF, the relative phase difference between the propagation modes is changed. This causes impedance shifts and the change of the output spectrum from the SMS.

In the experiment, the length of MMF was fixed at 7 cm because of its advantageous to be joined with the SMF-28 fibers. Hence, the transmission spectrum comb pattern will turn out to be more noticeable as the length of MMF builds up, because this increases the quantity of spatial mode beating in the MMF. Notwithstanding, from our perception, this does not fundamentally impact the affectability of the sensor.

The thermal stability of the sensor is high since the temperature sensitivity of the sensor is measured to be around  $-0.098667 \text{ nm}/^\circ\text{C}$ .

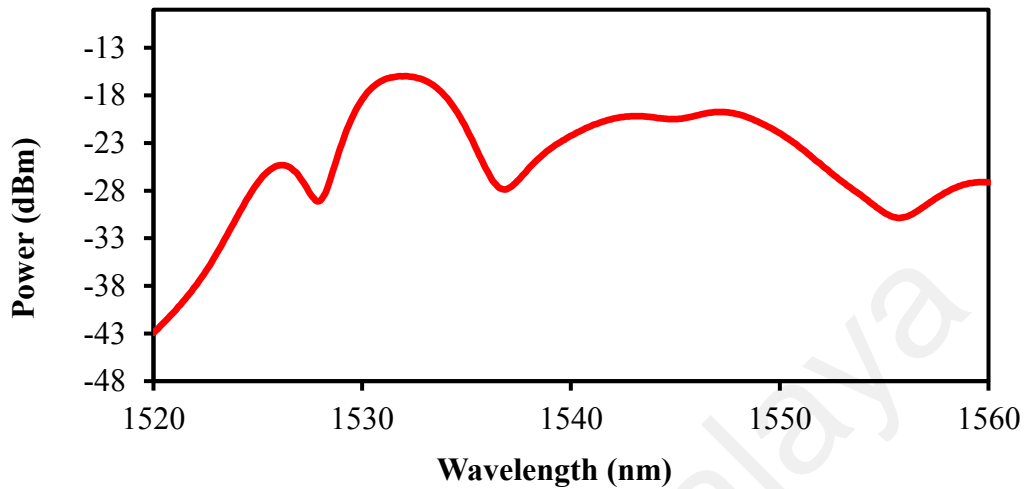


**Figure 5.6: SMS bandpass output spectrum at 40 kN compressive load.**

Figure 5.7 shows the peak spectral change at different loading measured at OSA resolution of 0.05 nm and span of 12 nm. Inset shows a spectral change at a bigger span from 1520 to 1560 nm. The bend in the MMF section has a significant influence on the mode distribution in the SMS structure, which in return will have a profound effect on the overall transmission characteristics of the SMS structure. It can be inferred from the figure that the peak wavelength of the interference comb spectrum shifts to a shorter wavelength as the load grows from 40 kN to 130 kN as shown in Figure 5.7.

This is attributed to the applied strain which change both of the refractive index of the core as well as the interaction length along the SMS. This in return changes the fringe spacing of the output spectral and shifts the peak spectrum towards a shorter wavelength region as shown in Figure 5.7. When the strain is removed from the sensor, the peak returned to its original position. It is observed that the pattern of interference spectrum completely changes as the load increases from 40 to 130 kN as shown in the inset figure.

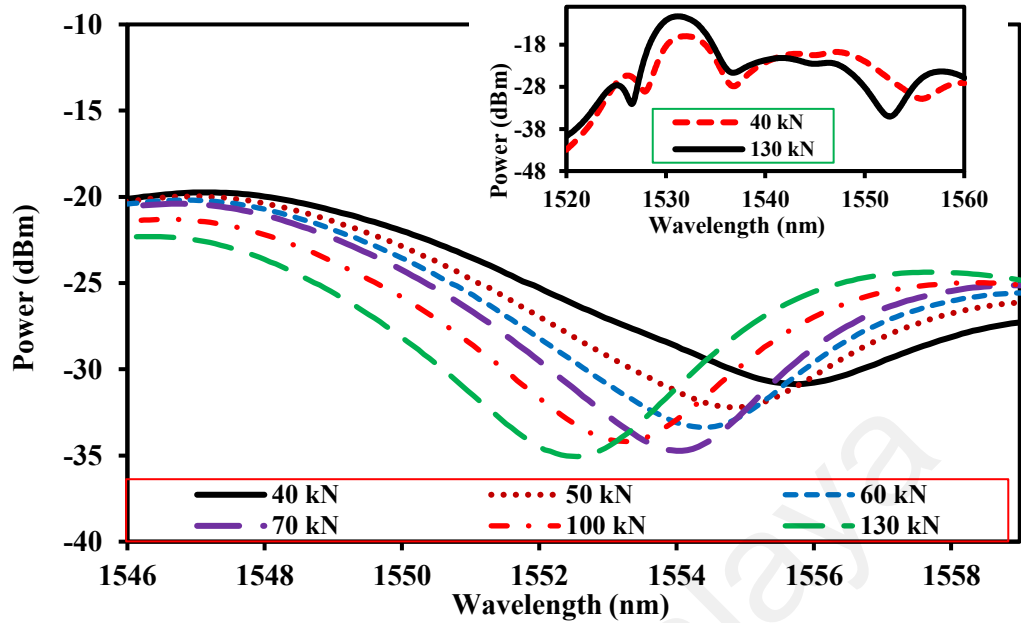


**Figure 5.7: Transmission spectra at different compressive loads within a span of 14 nm. The inset shows the spectra within a larger span of 40 nm.**

The ER-based compression strain and the peak of interference wavelength were also measured using a data logger and OSA, respectively for different amount of load and the result is illustrated in Figure 5.8. At the initial load of 40 kN, the ER strain gauge and OSA show a compressive strain of 2.050 mm/mm and peak centre wavelength of 1555.44 nm, respectively. As the load is increased, the compression strain linearly increases and the peak wavelength shifts to a shorter wavelength.

A total wavelength shift of 2.96 nm is obtained with a sensitivity of 0.0323 nm/kN as the load is increased from 40 to 130 kN. Above the 130 kN loading, the compressive strain shows a radical change to a higher value with a compressive strain of 7.658 mm/mm that is obtained from the maximum load of 145 kN. The peak centre wavelength curve has also a radical change to a shorter wavelength as the compression load is increased above 130 kN.

The increased change of compressive strain slope and the wavelength shift pattern above 130 kN explain the radical change in the mechanical property of the steel beam. This indicates the elastic mode limit has reached at this load, which is close to the predicted load amount of 158 kN as calculated based on Equation (5.1).

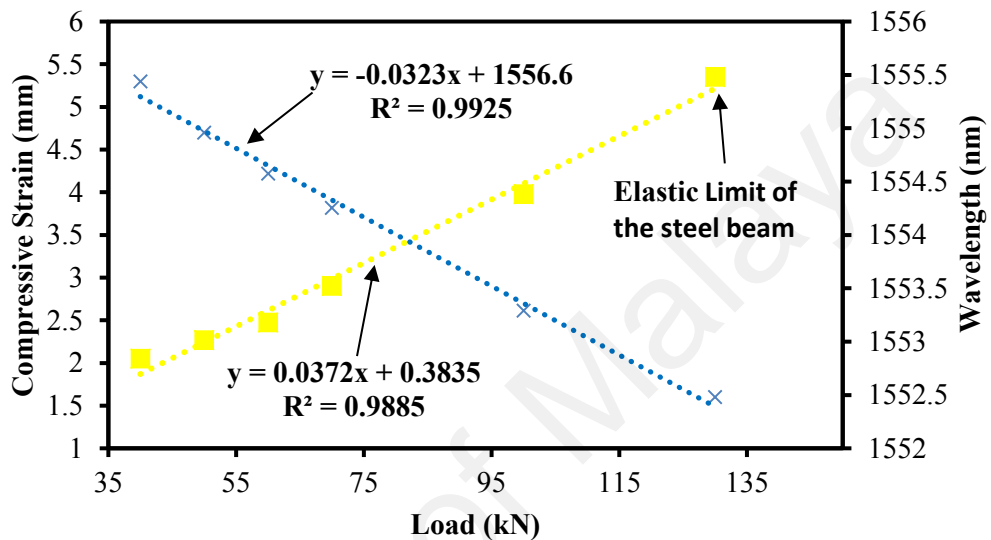


**Figure 5.8: Compressive strain and transmission dip wavelength at different amount of compressive load.**

Figure 5.9 shows the relation between the spectral wavelength and the compressive strain. It exhibits a linear curve with a slope of  $-0.7742 \text{ nm}/(\text{mm}/\text{mm})$  and linearity of more than 99% until the elastic limit of the steel beam. As the yield load is changed from 130 kN to 145 kN, the beam experiences the significant increase of the compressive strain from 5.351 to 7.658 mm/mm. The large change of strain as compared to any other transition of loading, is due to the beam strength and rigidity that have weakened. Beyond this applied load, the beam has exceeded its linear characteristic of modulus of elasticity, hence greater change of strain can be experienced by the beam. This is good agreement by the observation in Figure 5.9, where the large change of the strain is reflected as well by the large change of wavelength shift.

Below the elastic limit, the wavelength shift is well matched to the applied load which proves that the non-adiabatic sensor is able to measure the steel beam compressive strain with good sensitivity and linearity.

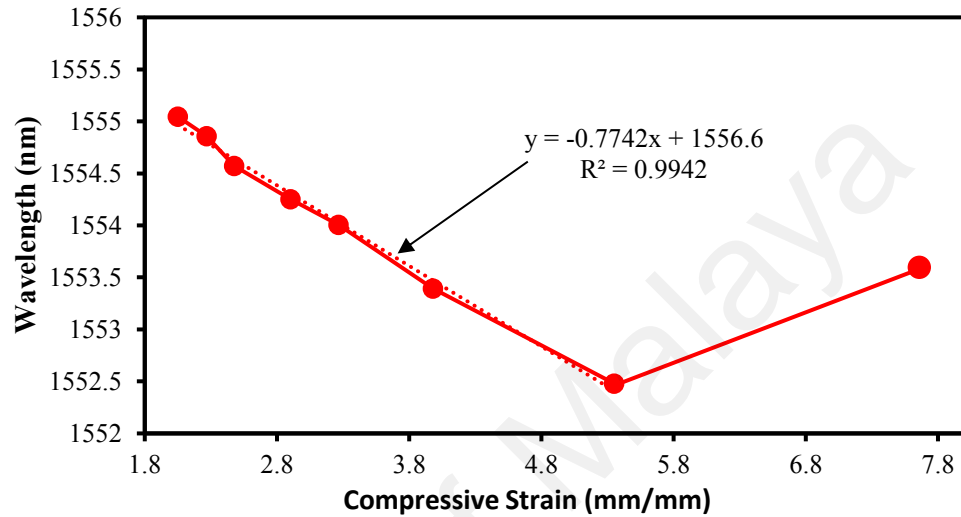


**Figure 5.9: Spectral wavelength shift with the compressive strain.**

#### **5.4 Optical Non-Adiabatic Silica Microfiber for Concrete Beam Compressive Strain Measurement**

In this section, we propose to use the non-adiabatic microfiber structure to measure compressive strain of a concrete beam. The proposed microfiber sensor is also able to measure a compression strain up to the modulus of rupture of the concrete beam at 8.67 kN. Modulus of rupture also known as flexural strength or bending strength, which identify the amount of stress and force for an unreinforced concrete slab, beam or other structure can withstand and to resists any bending failures (Bažant & Novák, 2001). This technique offers the advantages of a much simpler configuration, ease of fabrication and wide measurement range compared to the conventional optical sensors such as fiber Bragg grating (FBG).

Furthermore, the similar with steel beam strain measurement experiment, a parallel measurement is also made along the beam with an ER strain gauge method to measure the compressive strain sensitivity in order to validate the experimental data.

#### **5.4.1 Experimental Arrangement for Concrete Beam Strain Measurement**

The experimental setup for the compressive strain sensor to measure the concrete beam is illustrated in Figure 5.10 (a). The beam has a length of 500 mm length, width of 100 mm and depth of 100 mm. The beam was placed 25 mm from the end of support and the center ( $L/2$ ) of the beam was marked. The Instron universal testing machine with a 600kN static load capacity was applied at the center of the specimen. The aluminum bar with the diameter of 10 mm was employed between the load cell and the concrete beam to enhance the point load, as shown in Figure 5.10 (b). Then, the beam was loaded continuously without applying any shocks. The applied force shall be enforced at a constant rate until meeting the breaking point. The electrical resistance (ER) strain gauge was placed on the mid concrete beam of top surface of the bottom span using a superglue or cyanoacrylate adhesive. An adhesive tape was then used to cover the top part of the gauge. A data logger was connected to the ER strain gauge to read and record the strain values. A fused non-adiabatic microfiber was fabricated from a bare standard silica 125  $\mu\text{m}$  thick telecommunication fiber by brushing heat from a butane-oxy flame across a narrow region of the fiber, using computer-controlled stepper motor stages as described in Chapter 3.

The fabricated microfiber has a waist diameter of around 19  $\mu\text{m}$  over a length of about 40 mm and was connected to un-tapered fiber via non-adiabatic, conical transitions at both ends. The non-adiabatic silica microfiber structure was then attached to the concrete beam in a similar fashion as the previous experiments while vertically aligned with the position of the load cell, as shown in the Figures. 10 (a) and (b).

Amplified spontaneous emission (ASE) source operating at 1550 nm wavelength band was used as a light source while optical spectrum analyzer (OSA, Aritsu MS9710C) was used to capture the spectral change at the output of the sensor as shown in Figure 10 (a).

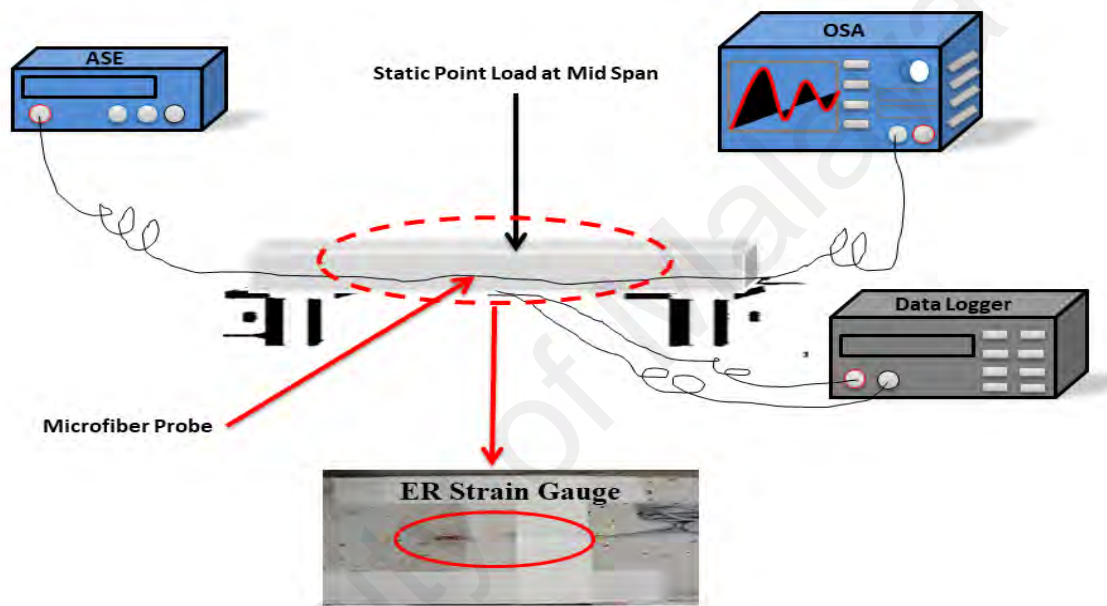
0.5kN was applied as an initial load and gradually increased at the Instron speed rate of 0.3 kN/min until several cracks appeared as shown in Figure 5.10 (c). The ER strain gauge and the SMS sensor measurements were simultaneously recorded for comparison. The experiment was conducted at room temperature in an enclosed building while the temperature was regulated to be around 27°C. The reading was measured for each 0.5kN compressive load increment. According ASTM (Astm C293-02, 2002), the flexural strength for center-point loading of the concrete beam can be estimated as;

$$R = \frac{3PL}{2bd^2} \quad (5.2)$$

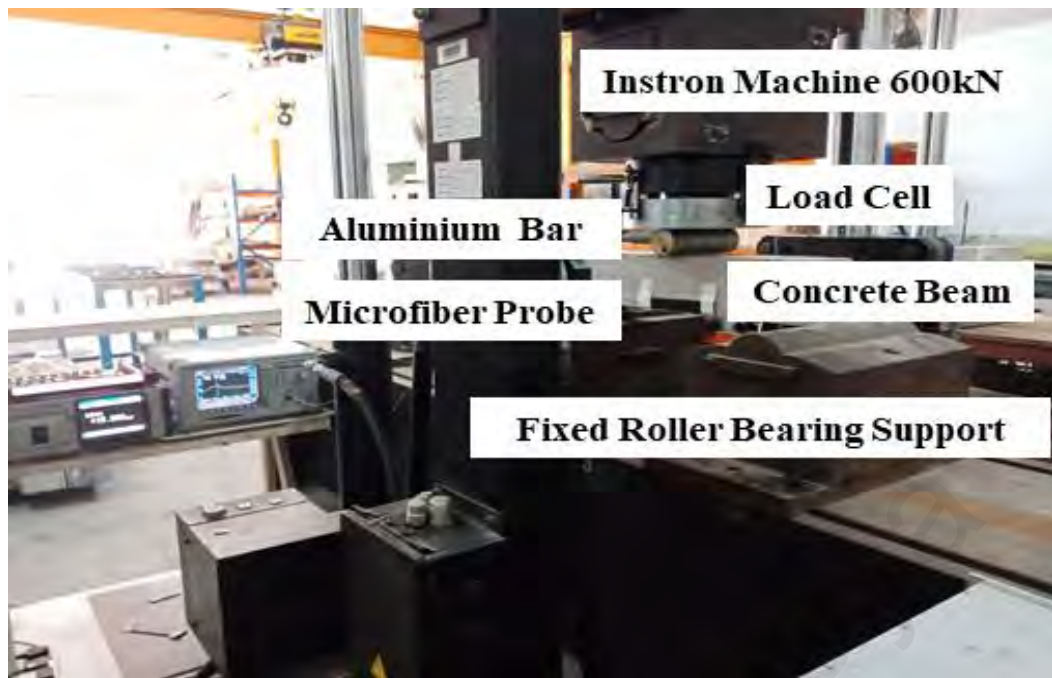
where R is the modulus of rupture (in a unit of MPa), P is the maximum applied load, which was obtained from the testing machine (N), L is the span length (mm), b is the average width of specimen at the fracture (mm) and d is the average depth of specimen (mm) at the fracture. National Ready Mixed Concrete Association (NRMCA) stated that the flexural strength is about 10 to 20 percent of compressive strength depending on the type, size and volume of the coarse aggregate used.

Flexural strength is one of the methods to measure the tensile strength of an unreinforced concrete beam to resist failure in concrete deformation. However, compressive strength will be used compared to flexural strength because compressive strength more convenient and reliable to judge the quality of the concrete as being delivered.

Since the concrete beam has the compressive load of 8.0 kN and the length of the specimen is 500 mm while both width and depth of the beam are 100mm, it is expected to reach its modulus of rupture at 1.8 MPa. As expected, the flexural strength was felt around 20 percent of compressive strength. Figure 5.10 (c) shows the crack of the concrete beam at breaking point.



(a)



(b)



(c)

**Figure 5.10: Schematic diagram of the compressive strain's testing setup (a) Schematic illustration (b) Image of laboratory setup (c) Left and right view of the crack comb of concrete beam at breaking point.**

#### 5.4.2 Result and Discussion

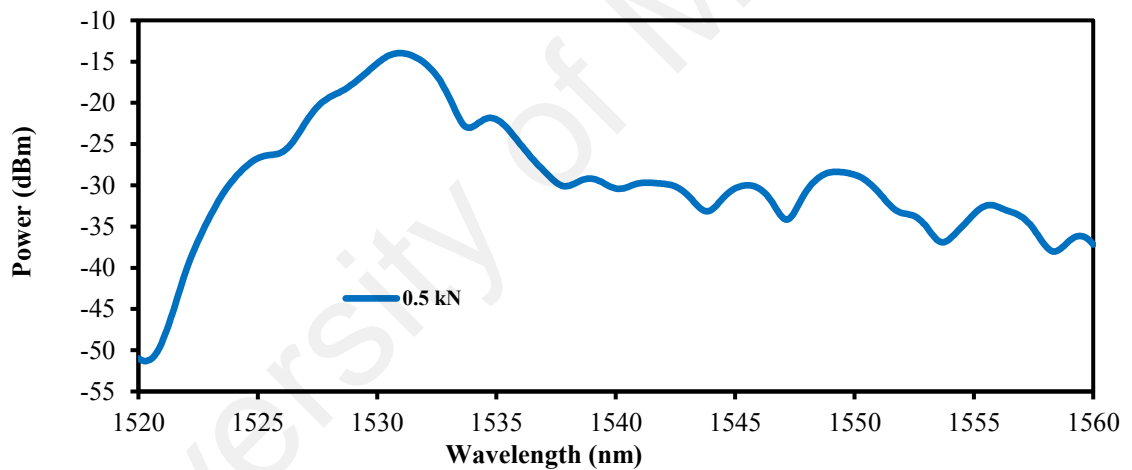
The output comb spectrum from the non-adiabatic microfiber structure at 0.5 kN load is shown in Figure 5.11. As the ASE light is launched into the microfiber, it is split into two portions at the input conical region; guided and unguided modes.

The guided mode kept travelling in the core and the unguided mode propagated through the cladding. Interference between the multiple modes of the microfiber's waist region produces a comb spectrum at the output end of the conical region. As shown in Figure 5.11, the microfiber structure has a bandpass spectral response with its peak to peak spacing of around 5.0 nm. This shape characteristic depends highly on the interference between the light modes that propagate along the tapered area. In this experiment, the tapered area was about 5 mm. In the experiment, the applied load was increased until the appearance of lines of fracture as the concrete beam meets its failure point.

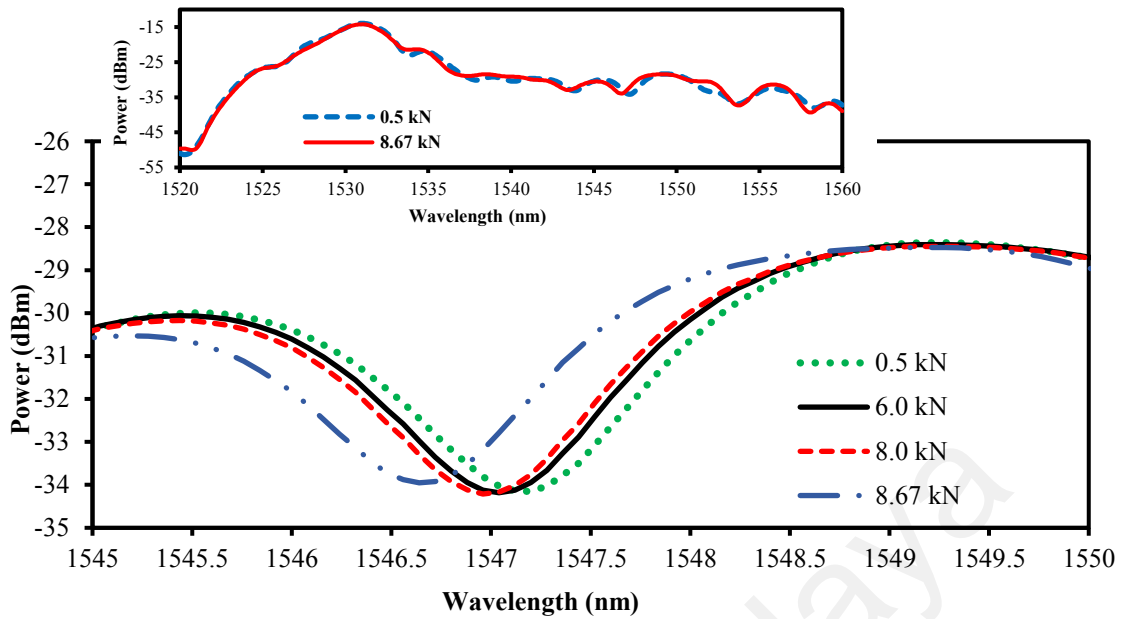
The structure of the non-adiabatic microfiber slightly changes as the compressive load increases. In consequence, the relative phase difference between the propagation modes is also changed due to the non-symmetrical refractive index distribution in the microfiber waist when the fiber is bent. This affects the interference of these modes, which in return changes the output spectrum from the microfiber. The length and diameter of the microfiber has significantly influenced the interference characteristic of the microfiber. As the length of microfiber increases, the number of spatial modes beating in the air cladding also increases and thus the transmission spectrum comb pattern will become more prominent. However, from our observation, this does not significantly influence the sensitivity of the sensor. The proposed microfiber sensor is also able to measure a compression strain up to the 3822  $\mu\epsilon$ .

Figure 5.12 shows the peak spectral change at different loading pressure measured at OSA resolution of 0.05 nm and span of 15 nm. Inset shows a spectral change at a bigger span from 1520 to 1560 nm. The bend in the tapered section has a significant influence on the mode distribution in the microfiber structure, which in return will have a profound effect on the overall transmission characteristics of the microfiber structure.

It can be inferred from the figure that the peak wavelength of the interference comb spectrum shifts to a shorter wavelength as the load grows from 0.5 kN to 8.0 kN as shown in Figure 5.12. This is attributed to the applied strain which change both of the refractive index of the core as well as the interaction length along the microfiber. This in return changes the fringe spacing of the output spectral and shifts the peak spectrum towards a shorter wavelength region as shown in Figure 5.12. When the strain is removed from the sensor, the peak returned to its original position. It is observed that the pattern of interference spectrum significantly changes as the load increases from 0.5 to 8.0 kN as shown in the inset figure.



**Figure 5.11: Non-adiabatic silica microfiber bandpass output spectrum at 0.5kN compressive load.**



**Figure 5.12: Spectral response output from the non-adiabatic silica microfiber structure at different compressive load within a span of 5.0 nm. Inset shows the spectra within a larger span of 40 nm.**

The electrical resistance-based compression strain and the peak of interference wavelength were also measured using a data logger and OSA, respectively for different amount of loads and the result is illustrated in Figure 5.13. At the initial load of 0.50 kN, the ER strain gauge and OSA show a compressive strain of 0.095 mm/mm and peak center wavelength of 1547.12 nm, respectively.

As the load increased, the compression strain linearly increases and the peak wavelength shifts to a shorter wavelength. A total wavelength shift of 0.16 nm is obtained with a sensitivity of 3.902 nm/kN as the load is increased from 0.5 kN to 8.00 kN. Above the 8.0 kN loading, the compressive strain shows a radical change to a higher value with a compressive strain of 0.68 mm/mm obtained at the maximum load of 8.67 kN. The peak center wavelength curve has also a radical change to a shorter wavelength as the compression load is increased above 8.0 kN.

The increased change of compressive strain slope and the wavelength shift pattern above 8.0 kN explains the radical change in the mechanical property of the concrete beam. This indicates the modulus fracture has reached at this load, which is close to the predicted load amount of 8.67 kN.

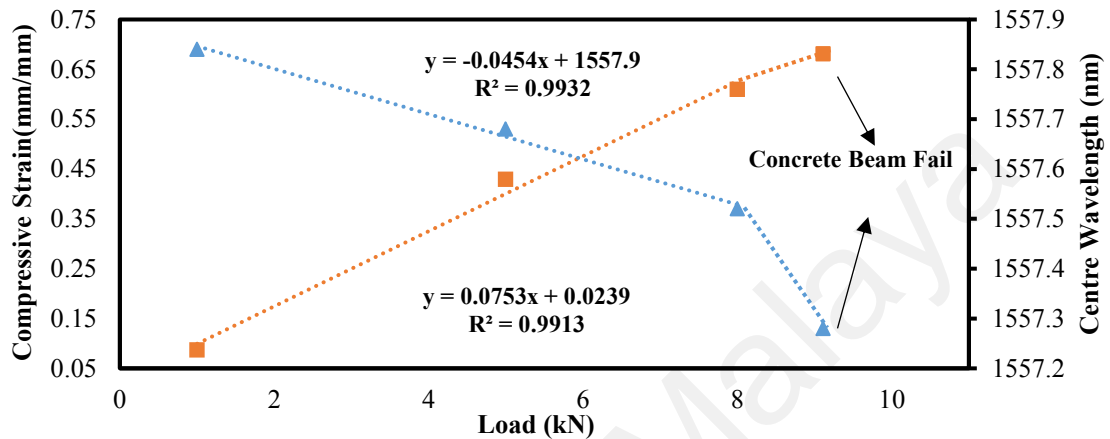


**Figure 5.13: Compressive strain and peak center wavelength at different amount of compressive load.**

Figure 5.14 shows the relation between the spectral wavelength and the compressive strain. It exhibits a linear curve with a slope of 0.0454 nm/(mm/mm) and linearity of more than 99% until the breaking point of the concrete beam. As the yield load is changed from 8.0 kN to 8.67 kN, the beam experiences the significant increase of the compressive strain from 0.639 to 0.68 mm/mm. The large change of strain as compared to any other transition of loading, is due to the beam strength and rigidity that have weakened.

Beyond this applied load, the beam has exceeded its linear characteristic, hence greater change of strain can be experienced by the beam. This is good agreement by the observation in Figure 5.13, where the large change of the strain is reflected as well by the large change of wavelength shift. Before failure, the wavelength shift is well matched to the applied load which prove that the non-adiabatic sensor is able to measure the concrete beam compressive strain with good sensitivity and linearity.

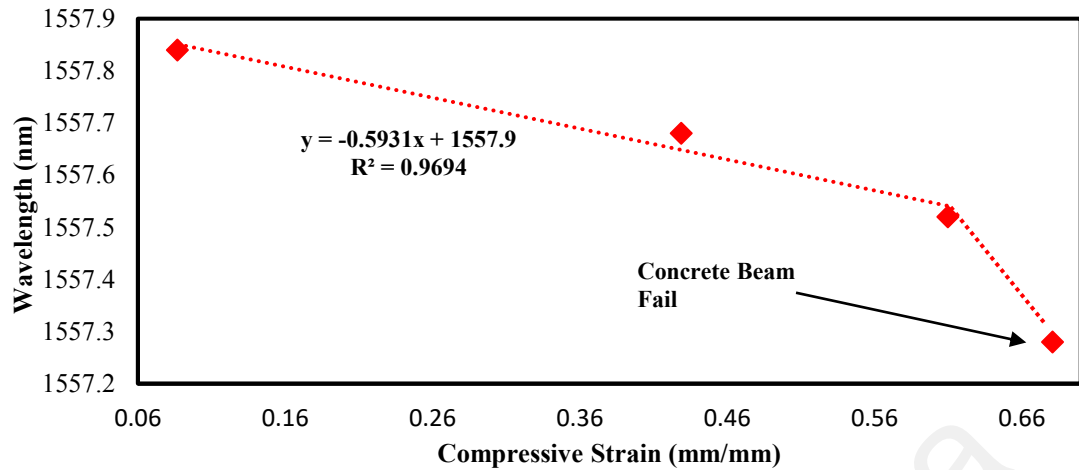


**Figure 5.14: Spectral wavelength shift with the compressive strain.**

### 5.5 SMS Sensor for Concrete Beam Compressive Strain Measurement

SMS based sensor has much simpler configuration as its structure consisting of two SMF spliced at both ends of the MMF. When a broadband light source is injected into the SMS structure, a modulated transmission spectrum is produced by multimode excitation, multimode interference, and light recoupling from the MMF into the SMF. The multimode interference pattern can be changed when a strain is applied to the MMF. This allows the SMS structure to serve as a strain sensor in which shift in peak transmission wavelength are observed as described in the previous section. In this section, the SMS fiber structure is investigated and demonstrated to measure the compressive strain on a reinforced concrete beam.

In this work, an SMS was used to verify the optical fiber sensor performance to measure different strains on the concrete beam. The SMS fiber structure was formed by fusion splicing as described in Chapter 3. The experimental setup for the compressive strain measurement is same as Figure 5.10 (a), where the non-adiabatic microfiber probe was changed to SMS sensor probe. The similar concrete beam with a length of 500 mm length, width of 100 mm and depth of 100 mm was used in the experiment.

The SMS was properly aligned in a straight manner at the mid-span position on the top surface of the reinforced concrete beam using a tape meter to ensure accurate measurement. The SMS is fixed on the beam using epoxy adhesive to provide strong adhesion based on the same arrangement with the previous experiment. The similar measurement was also carried out as the beam was loaded continuously until it meets the breaking point.

The measured spectral response of the SMS fiber structure, which was measured at the same OSA settings for various compressive loads, is shown in Figure 5.15. As shown in the figure, both the peak wavelength and the power of the spectra changed as the load increased. The dip of the bandpass transmission spectrum shifted to a shorter wavelength as the load increased. Moreover, as the load was increased, the measured power at the dip region was observed to decrease as shown in Figure 5.15.

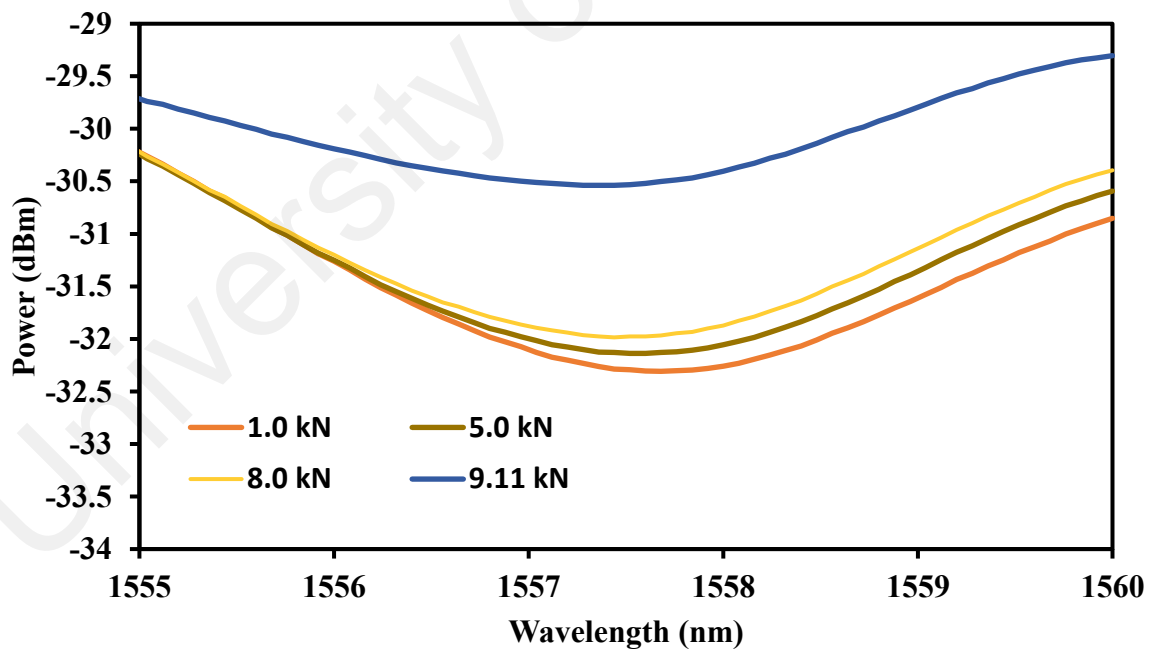


**Figure 5.15: Spectral response output from the SMS structure at different compressive loads.**

A transmission dip linearly shifted from 1557.68 nm to 1557.52 nm (a total wavelength shift of 0.16 nm) as the load is increased from 1 kN to 8.00 kN. 1 kN to 8.00 kN. Above the 8.0 kN loading, the dip center wavelength curve showed a radical change to a shorter wavelength as shown in Figure 5.15. This is attributed to the radical change of the compression strain as the compression load is increased above 8.0 kN. The result is in good agreement with the previous sensor based on the nonadiabatic microfiber as described in the previous section.

## 5.6 Summary

The silica microfiber was shown to be able to measure a steel beam compressive strain from an initial value of 1.567 mm/mm to the final value of 7.370 mm/mm, which achieved its elastic limit at a compressive load of 130 kN and 143 kN for plastic limit. The non-adiabatic microfiber sensor exhibits linear sensitivity of 0.0094 nm/kN for the compression strain measurement.

While, the SMSF was being able to measure a steel beam compressive strain from an initial value of 2.05 mm/mm to the final value of 5.351 mm/mm. The steel beam also achieved its elastic mode limit at compressive load of 130 kN. The SMS sensor exhibits linear sensitivity of 0.0323 nm/kN for the compression strain measurement.

The simple non-adiabatic microfiber sensor was also successfully demonstrated for measuring compression strain and to the breaking point of a concrete beam. It was found that the sensor was able to measure a concrete beam compressive strain from an initial value of 0.095 mm/mm to the final value of 0.68 mm/mm. The concrete beam achieved its modulus of rupture limit at compressive load of 8.0 kN and linear sensitivity is 0.0454 nm/kN. On the other hand, the SMS sensor also exhibited that the rupture limit of the concrete beam was at compressive load of 8.0 kN.

Table 5.1 shown the comparison between SMS and microfiber output for steel and concrete beam. From the table it shown that the microfiber is better than SMSF.

**Table 5.1: Comparison result between SMS and microfiber.**

Type of Structure	Type of Sensor	Compressive Strain (mm/mm)		Failure		Linear Sensitivity (nm/kN)
		Initial	Final	Elastic Limit (kN)	Plastic Limit (kN)	
Steel beam	Microfiber	1.567	7.370	130	143	0.0094
	SMS	2.05	5.351	130	143	0.0323
Concrete beam	Microfiber	0.095	0.68	8.0		0.0454
	SMS			8.0		

## CHAPTER 6

### CONCLUSION AND FUTURE OUTLOOK

#### 6.1 Conclusion

Optical fiber sensors have drawn great interest in recent years especially for application in the areas of structural health monitoring (SHM). Up to date, a number of optical fiber sensor has been proposed and demonstrated for monitoring the safety and health of composite materials, vast structural designing structures and quantitative substance process. These sensors were mostly in the forms of Mach–Zehnder interferometers (MZIs), fiber Bragg gratings and long-period gratings. In this thesis, simple, affordable and feasible temperature and strain sensors were successfully proposed and demonstrated for SHM purposes based on optical approaches.

In this work, two types of optical sensor probes; microfiber and single mode-multimode-single mode fiber (SMS) structure were successfully fabricated and characterized using a silica optical fiber using a flame brushing and fusion splicing respectively. The non-adiabatic type of microfiber produced a periodic behavior at the output spectrum due to the oscillations as a result of back and forth coupling between core and cladding modes. On the other hand, the SMS structure generates a sufficient bandpass spectral response for a given wavelength range. Both non-adiabatic microfiber and SMS device are capable to be used to demonstrate various sensing applications. For instance, a load sensor was successfully demonstrated by using the fabricated SMS structure, which was clamped onto a stage. The device is fabricated by splicing a section of multimode optical fiber (MMF) in between single-mode fibers (SMFs). The modal interference inside the structure produces a strong resonant transmission notch, which is sensitive to external perturbation.

It was found that the position of the notch changed with strain at various sensitivity depending on MMF length. The device introduced here is simply to fabricate, robust and suitable for high temperature operation; hence, it is adequate for diverse sensing applications

Temperature and strain sensors were successfully demonstrated using non-adiabatic microfiber and SMS structure as a probe. The fiber-based temperature sensors are capable to operate at high temperature using multimode interference effect. Interference fringes of the output red-shifted as the temperature increased due to the change in the effective refractive index of the multiple modes inside both structures. The proposed microfiber and SMS sensors were shown to be able to measure temperature stably up to 400°C with sensitivities of 6.0 pm/°C and 11.1 pm/°C, respectively. The non-adiabatic microfiber and the SMS optical fiber probes were also established for strain measurements. The strain sensitivities originate from the difference of the effective refractive index of the core and the cladding modes, which induces resonant wavelength shift against the strain. A total wavelength shift for a non-adiabatic silica microfiber and a SMS fiber device were 1.08 nm and 9.6 nm respectively. Therefore, the strain sensitivity of the microfiber measured to be -1.36 nm/n while the SMS optical fiber was -2.06 nm/n with a linearity of more than 0.99 and 0.97. Both sensor designs are simple and thus they can be mass-produced with a relatively low cost.

Finally, both non-adiabatic silica microfiber and SMS based optical sensors were successfully employed for measurements of compression strain in both steel and concrete beam structures. Both sensors were capable in measuring the elastic limit of both steel and concrete beams. The silica microfiber was shown to be able to measure a steel beam compressive strain from an initial value of 1.567 mm/mm to the final value of 7.370 mm/mm.

The optical sensor was also able to detect the elastic limit of the steel beam by its significant change of the peak center wavelength. The steel beam achieved its elastic mode limit at a compressive load of 130 kN, which agrees well with the conventional electrical resistance (ER) strain gauge measurement. While at 143 kN, the beam experienced plastic limit condition, which means the beam cannot going back to its original shape. The non-adiabatic microfiber sensor exhibits linear sensitivity of 0.0094 nm/kN for the compression strain measurement.

On the other hand, the SMS probe was being able to measure a steel beam compressive strain from an initial value of 2.05 mm/mm to the final value of 5.351 mm/mm. The optical sensor also was being able to detect the elastic limit of the steel beam by its significant change of the center wavelength of the transmission dip. The steel beam also achieved its elastic mode limit at compressive load of 130 kN. The SMS sensor exhibits linear sensitivity of 0.0323 nm/kN for the compression strain measurement.

The simple non-adiabatic microfiber sensor was also successfully demonstrated for measuring compression strain and to the breaking point of a concrete beam. It was found that the sensor was able to measure a concrete beam compressive strain from an initial value of 0.095 mm/mm to the final value of 0.68 mm/mm. The optical sensor was being able to detect the modulus rupture of the concrete beam by its significant change of the center wavelength of the transmission dip too. The concrete beam achieved its modulus of rupture limit at compressive load of 8.0 kN, which agrees well with the conventional ER strain gauge measurement. The non-adiabatic microfiber sensor exhibits linear sensitivity of 0.0454 nm/kN for the compression strain measurement. On the other hand, the SMS sensor also exhibited that the rupture limit of the concrete beam was at compressive load of 8.0 kN.

In summary, both non-adiabatic microfiber and SMS device are capable to be used to demonstrate a simple, affordable and feasible temperature and strain sensors for SHM purposes. Both microfiber and SMS structure were fabricated using a flame brushing and splicing approach, respectively. They have excellent characteristics to function as a probe for temperature. Both non-adiabatic silica microfiber and SMS based on optical sensors were successfully employed for measurements of compression strain in both steel and concrete beam structures.

## **6.2 Future Outlook**

From the results and analysis, there are still rooms for improvement in the design and the installation method of the sensor either to improve its sensitivity or practical aspect. Overall, the results show promising potential for a real-time monitoring application such as in bridge and other giant structures. The results show that both non-adiabatic microfiber and SMS sensors have a great potential to be applied in a real-time SHM applications. However, there are some caveats that must be addressed in future work. First, the sensitivity of both sensors should be improved by optimizing its sensor structure, packaging and assembly. Second, new ways of installing the package must be identified, so that the whole microfiber and SMS technologies are all well streamlined. The following works are also recommended for future study;

- Preparing simulation software in order to compare the actual result with the simulated result.

- The proposed strain measurement method is simple and practical to measure the strain of both steel and concrete structures. These methods can be used for developing fully automatic, real time for SHM. Since the signal is optical, raw data can be directly transfer using optical fiber cable. Hence, the data can be analyzed remotely and the result can be monitored in real time.
- The future work should be concentrated on trying both probes inside concrete beam or more complex structure since both of them were applied outside the steel and concrete structures in the current work.

University of Malaysia

## REFERENCES

- Ahmad, M., & Hench, L. L. (2005). Effect of taper geometries and launch angle on evanescent wave penetration depth in optical fibers. *Biosensors and Bioelectronics*, 20(7), 1312–1319. <https://doi.org/10.1016/j.bios.2004.04.026>
- Aktan, A. E., & Tsikos, F. N. C. K. A. G. and C. J. (2000). Issues in Infrastructure Health Monitoring for Management. *Journal of Engineering Mechanics*, (126), 711–724.
- Ansari, F. (1997). State-of-the-art in the applications of fiber-optic sensors to cementitious composites. *Cement and Concrete Composites*, 19(1), 3–19. [https://doi.org/10.1016/S0958-9465\(96\)00038-8](https://doi.org/10.1016/S0958-9465(96)00038-8)
- Antonio-Lopez, J. E., Castillo-Guzman, a, May-Arrijoja, D. a., Selvas-Aguilar, R., & Likamwa, P. (2010). Tunable multimode-interference bandpass fiber filter. *Optics Letters*, 35(3), 324–326. <https://doi.org/10.1364/OL.35.000324>
- Antunes, P., Domingues, F., Granada, M., & André, P. (2012). Mechanical Properties of Optical Fibers. *INTECH Open Access Publisher*, 1–15. <https://doi.org/10.5772/26515>
- Ascorbe, J., Corres, J., Arregui, F., & Matias, I. (2017). Recent Developments in Fiber Optics Humidity Sensors. *Sensors*, 17(4), 893. <https://doi.org/10.3390/s17040893>
- Astm C293-02. (2002). Standard Test Method for Flexural Strength of Concrete (Using Simple Beam With Center-Point Loading). *Annual Book of ASTM Standards*, 1–3. <https://doi.org/10.1520/D1635>
- Barrera, D., Finazzi, V., Villatoro, J., Sales, S., & Pruneri, V. (2012). Packaged optical sensors based on regenerated fiber bragg gratings for high temperature applications. *IEEE Sensors Journal*, 12(1), 107–112. <https://doi.org/10.1109/JSEN.2011.2122254>
- Bažant, Z. P., & Novák, D. (2001). Proposal for standard test of modulus of rupture of concrete with its size dependence. *ACI Materials Journal*, 98(1), 79–87.
- Belal, M., Song, Z., Jung, Y., Brambilla, G., & Newson, T. P. (2010). Optical fiber microwire current sensor. *Optics Letters*, 35(18), 3045. <https://doi.org/10.1364/OL.35.003045>
- Bernini, R., Minardo, A., Testa, G., & Zeni, L. (2010). Dynamic strain measurements on a cantilever beam using stimulated Brillouin scattering. *Smart Materials and Structures*, 19(4). <https://doi.org/10.1088/0964-1726/19/4/045024>

- Bertelli, D., Lolli, M., Papotti, G., Bortolotti, L., Serra, G., & Plessi, M. (2010). Detection of honey adulteration by sugar syrups using one-dimensional and two-dimensional high-resolution nuclear magnetic resonance. *Journal of Agricultural and Food Chemistry*, 58(15), 8495–8501. <https://doi.org/10.1021/jf101460t>
- Bidin, N., Zainuddin, N. H., Islam, S., Abdullah, M., Marsin, F. M., & Yasin, M. (2016). Sugar Detection in Adulterated Honey via Fiber Optic Displacement Sensor for Food Industrial Applications. *IEEE Sensors Journal*, 16(2), 299–305. <https://doi.org/10.1109/JSEN.2015.2479413>
- Bilodeau, F., Hill, K. O., Faucher, S., & Johnson, D. C. (1988). Low-Loss Highly Overcoupled Fused Couplers: Fabrication and Sensitivity to External Pressure. *Journal of Lightwave Technology*, 6(10), 1476–1482. <https://doi.org/10.1109/50.7904>
- Birks, T. A., & Li, Y. W. (1992). The Shape of Fiber Tapers. *Journal of Lightwave Technology*, 10(4), 432–438. <https://doi.org/10.1109/50.134196>
- Black, R. J., Lacroix, S., Gonthier, F., & Love, J. D. (1991). Tapered single-mode fibers and devices Part 2 : Experimental and theoretical quantification. *IEE Proceedings- Journal of Optoelectronics*, 138(5), 355–364. <https://doi.org/10.1049/ip-j.1991.0061>
- Brambilla, G. (2010). Optical fibre nanowires and microwires: A review. *Journal of Optics A: Pure and Applied Optics*, 12(4). <https://doi.org/10.1088/2040-8978/12/4/043001>
- Brambilla, G. (2010). Optical fibre nanotaper sensors. *Optical Fiber Technology*, 16(6), 331–342. <https://doi.org/10.1016/j.yofte.2010.08.009>
- Brambilla, G., Finazzi, V., & Richardson, D. J. (2004). Ultra-low-loss optical fiber nanotapers. *Optics Express*, 12(10), 2258. <https://doi.org/10.1364/OPEX.12.002258>
- Brambilla, G., Koizumi, F., Feng, X., Richardson, D. J., & A. (2005). Compound-glass optical nanowires G. *ELECTRONICS LETTERS*, 41(7). <https://doi.org/10.1049/el>
- Brambilla, G., Xu, F., Horak, P., Jung, Y., Koizumi, F., Sessions, N. P., ... Richardson, D. J. (2009). Optical fiber nanowires and microwires: fabrication and applications. *Advances in Optics and Photonics*, 1(1), 107. <https://doi.org/10.1364/AOP.1.000107>
- Bremer, K., Wollweber, M., Weigand, F., Rahlves, M., Kuhne, M., Helbig, R., & Roth, B. (2016). Fibre Optic Sensors for the Structural Health Monitoring of Building Structures. *Procedia Technology*, 26, 524–529. <https://doi.org/10.1016/j.protec.2016.08.065>

- Brownjohn, J. M. W. (2007). Structural health monitoring of civil infrastructure. *Philosophical Transactions of the Royal Society A: Mathematical, Physical and Engineering Sciences*, 365(1851), 589–622. <https://doi.org/10.1098/rsta.2006.1925>
- Brownjohn, J., Tjin, S., Tan, G., Tan, B., & Chakraboorty, S. (2004). A structural health monitoring paradigm for civil infrastructure. In *1st FIG International Symposium on Engineering Surveys for Construction Works and Structural Engineering Nottingham, United Kingdom* (pp. 1–15).
- Chang, C., & Mehta, R. (2009). *Fiber optic sensors for transportation infrastructural health monitoring. IFAC Proceedings Volumes (IFAC-PapersOnline)* (Vol. 42). IFAC. <https://doi.org/10.3182/20090902-3-US-2007.0060>
- Chen, J., Reed, M. A., Rawlett, A. M., & Tour, J. M. (1999). Large on-off ratios and negative differential resistance in a molecular electronic device. *Science*, 286(5444), 1550–1552. <https://doi.org/10.1126/science.286.5444.1550>
- Chen, Y., Han, Q., Liu, T., & Lü, X. (2015a). Self-temperature-compensative refractometer based on singlemode-multimode-singlemode fiber structure. *Sensors and Actuators, B: Chemical*, 212, 107–111. <https://doi.org/10.1016/j.snb.2015.01.080>
- Chen, Y., Han, Q., Liu, T., & Lü, X. (2015b). Sensors and Actuators B: Chemical Self-temperature-compensative refractometer based on singlemode – multimode – singlemode fiber structure. *Sensors & Actuators: B. Chemical*, 212, 107–111. <https://doi.org/10.1016/j.snb.2015.01.080>
- Chew, S. P., Zulkifli, A. Z., Hamad, H., Harun, S. W., Lee, L. Y., Razak, H. A., & Adikan, F. R. M. (2018). Singlemode-multimode-singlemode fiber structure as compressive strain sensor on a reinforced concrete beam. *Optik - International Journal for Light and Electron Optics*, 154, 705–710. <https://doi.org/10.1016/J.IJLEO.2017.10.033>
- Chiam, Y. S., Lim, K. S., Harun, S. W., Gan, S. N., & Phang, S. W. (2014). Conducting polymer coated optical microfiber sensor for alcohol detection. *Sensors and Actuators, A: Physical*, 205, 58–62. <https://doi.org/10.1016/j.sna.2013.10.025>
- Childers, B. A., Froggatt, M. E., Allison, S. G., Moore, Sr., T. C., Hare, D. A., Batten, C. F., & Jegley, D. C. (2001). Use of 3000 Bragg grating strain sensors distributed on four 8-m optical fibers during static load tests of a composite structure. *Proceedings of SPIE*, 4332, 133–142. <https://doi.org/10.1117/12.429650>
- Clohessy, A. M., Healy, N., Murphy, D. F., & Hussey, C. D. (2005). Short low-loss nanowire tapers on singlemode fibre. *Electronics Letters*, 41(17). <https://doi.org/10.1049/el>
- Coillet, A., & Grelu, P. (2012). Third-harmonic generation in optical microfibers: From silica experiments to highly nonlinear glass prospects. *Optics Communications*, 285(16), 3493–3497. <https://doi.org/10.1016/j.optcom.2012.04.020>

- Crane, R. M., Macander, A. B., & Gagorik, J. (1983). Fiber Optics for a Damage Assessment System for Fiber Reinforced Plastic Composite Structures. In D. O. Thompson & D. E. Chimenti (Eds.), *Review of Progress in Quantitative Nondestructive Evaluation: Volume 2A* (pp. 1419–1430). Boston, MA: Springer US. [https://doi.org/10.1007/978-1-4613-3706-5\\_94](https://doi.org/10.1007/978-1-4613-3706-5_94)
- Das, M., Shirasaki, a., Nayak, K. P., Morinaga, M., Le Kien, F., & Hakuta, K. (2010). Measurement of fluorescence emission spectrum of few strongly driven atoms using an optical nanofiber. *Optics Express*, *18*(16), 17154–17164. <https://doi.org/10.1364/OE.18.017154>
- Dass, S., & Jha, R. (2016). Microfiber-Wrapped Bi-Conical-Tapered SMF for Curvature Sensing. *IEEE Sensors Journal*, *16*(10), 3649–3652. <https://doi.org/10.1109/JSEN.2016.2531748>
- Degradpre, M. D., & Burgess, L. W. (1990). Fiber-optic FT-NIR evanescent field absorbance sensor. *Applied Spectroscopy*, *44*(2), 273–279. <https://doi.org/10.1366/0003702904085453>
- Deng, L., & Cai, C. S. (2007). Applications of fiber optic sensors in civil engineering. *Structural Engineering and Mechanics*, *25*(5), 577–596. <https://doi.org/10.12989/sem.2007.25.5.577>
- Di Sante, R. (2015). Fibre Optic Sensors for Structural Health Monitoring of Aircraft Composite Structures: Recent Advances and Applications. *Sensors*, *15*(8), 18666–18713. <https://doi.org/10.3390/s150818666>
- Dong, B., Wei, L., Zhou, D., Liu, W., & Lit, J. W. Y. (2009). Temperature-independent strain sensor based on a core-offset multi-mode fiber interferometer, *7316*, 1–7. <https://doi.org/10.1117/12.818903>
- Drake, D., Sullivan, R., & Wilson, J. (2018). Distributed Strain Sensing from Different Optical Fiber Configurations. *Inventions*, *3*(4), 67. <https://doi.org/10.3390/inventions3040067>
- Duan, D.-W., Rao, Y., Hou, Y.-S., & Zhu, T. (2012). Microbubble based fiber-optic Fabry–Perot interferometer formed by fusion splicing single-mode fibers for strain measurement. *Applied Optics*, *51*(8), 1033. <https://doi.org/10.1364/AO.51.001033>
- Dybko, A. (2006). Fundamentals Of Optoelectronics. In *Optical Chemical Sensors* (pp. 47–58). Springer US. [https://doi.org/10.1007/1-4020-4611-1\\_3](https://doi.org/10.1007/1-4020-4611-1_3)
- E.E.H.Love. (1906). *A Treatise on the mathematical theory of elasticity* (2nd ed.). Cambridge University Press.
- Emami, M., & Goodarzi, R. (2018). Optoelectronic correlations for gold thin films in different annealing temperature. *Optik*, *171*(June), 397–403. <https://doi.org/10.1016/j.ijleo.2018.06.075>

- Ericsson Cables AB. (1999). User's manual for the FSU 975 single fiber fusion splicer by. Sweden. Retrieved from [papers://5e91a182-ae2c-4430-b0c0-e247c26dfcb2/Paper/p102](https://papers://5e91a182-ae2c-4430-b0c0-e247c26dfcb2/Paper/p102)
- Farrar, C. R., & Worden, K. (2007). An introduction to structural health monitoring. *Philosophical Transactions of the Royal Society A: Mathematical, Physical and Engineering Sciences*, 365(1851), 303–315. <https://doi.org/10.1098/rsta.2006.1928>
- Feng, X., Tam, H., Chung, W., & Wai, P. K. A. (2006). Multiwavelength fiber lasers based on multimode fiber Bragg gratings using offset launch technique. *Optics Communications*, 263, 295–299. <https://doi.org/10.1016/j.optcom.2006.02.006>
- Ferdinand, P. (2014). The Evolution of Optical Fiber Sensors Technologies During the 35 Last Years and Their Applications in Structure Health Monitoring. In *EWSHM-7th European Workshop on Structural Health Monitoring*.
- Fernandez-Valdivielso, Matias, I. R., & Arregui, F. J. (2002). Simultaneous measurement of strain and temperature using a fiber Bragg grating and a thermochromic material. *Sensors and Actuators A: Physical*, 101, 107–116. <https://doi.org/10.1109/OFS.2002.1000537>
- Fernandez-Vallejo, M., & Lopez-Amo, M. (2012). Optical fiber networks for remote fiber optic sensors. *Sensors*, 12(4), 3929–3951. <https://doi.org/10.3390/s120403929>
- Ferreras, A., Rodríguez, F., Gómez-Salas, E., De Miguel, J. L., & Hernández-Gil, F. (1993). Useful Formulas for Multimode Interference Power Splitter/Combiner Design. *IEEE Photonics Technology Letters*, 5(10), 1224–1227. <https://doi.org/10.1109/68.248435>
- Franco, M. A. R., & Serrão, V. A. (2017). Specialty Optical Fibers for Sensors. *Revista de La Facultad de Ingenieria*, 2(December 2016), 3–8.
- Frazao, O., Silva, S. O., Viegas, J., Ferreira, L. a., Araujo, F. M., & Santos, J. L. (2011). Optical fiber refractometry based on multimode interference. *Applied Optics*, 50(25), E184. <https://doi.org/10.1364/AO.50.00E184>
- G.Brambilla, F.Xu, & X.Feng. (2006). Fabrication of optical fibre nanowires and their optical and mechanical characterisation. *Electronics Letters*, 42(9). <https://doi.org/10.1049/el>
- Gao, R. X., Wang, Q., Zhao, F., Meng, B., & Qu, S. L. (2010). Optimal design and fabrication of SMS fiber temperature sensor for liquid. *Optics Communications*, 283(16), 3149–3152. <https://doi.org/10.1016/j.optcom.2010.04.027>
- Ghasemi, M., Choudhury, P. K., Baqir, M. A., Mohamed, M. A., Zain, A. R. M., & Majlis, B. Y. (2017). Metamaterial absorber comprising chromium–gold nanorods-based columnar thin films. *Journal of Nanophotonics*, 11(4), 043505. <https://doi.org/10.1117/1.JNP.11.043505>

- Glisic, B., Inaudi, D., & Casanova, N. (2010). SHM process as perceived through 350 projects, 7648, 76480P. <https://doi.org/10.1117/12.852340>
- Glossop, N. D. W., Dubois, S., Tsaw, W., Leblanc, M., Lymer, J., Measures, R. M., & Tennyson, R. C. (1990). Optical fibre damage detection for an aircraft composite leading edge. *Composites*, 21(1), 71–80. [https://doi.org/10.1016/0010-4361\(90\)90100-B](https://doi.org/10.1016/0010-4361(90)90100-B)
- Gong, Y., Zhao, T., Rao, Y. J., & Wu, Y. (2011). All-fiber curvature sensor based on multimode interference. *IEEE Photonics Technology Letters*, 23(11), 679–681. <https://doi.org/10.1109/LPT.2011.2123086>
- Guan, B. O., Li, J., Jin, L., & Ran, Y. (2013). Fiber Bragg gratings in optical microfibers. *Optical Fiber Technology*, 19(6 PART B), 793–801. <https://doi.org/10.1016/j.yofte.2013.07.007>
- Guemes, A., Fernandez-Lopez, A., Díaz-Maroto, P., Lozano, A., & Sierra-Perez, J. (2018). Structural Health Monitoring in Composite Structures by Fiber-Optic Sensors. *Sensors*, 18(4), 1094. <https://doi.org/10.3390/s18041094>
- Gunawardena, D. S. (2016). *Photosensitivity, Grating Strength and Thermal Endurance of Fibre Bragg Gratings*. Universiti Malaya.
- Gunawardena, D. S., Lai, M. H., Lim, K. S., Malekmohammadi, A., & Ahmad, H. (2016). Fabrication of thermal enduring FBG sensor based on thermal induced reversible effect. *Sensors and Actuators, A: Physical*, 242, 111–115. <https://doi.org/10.1016/j.sna.2016.03.001>
- Gunawardena, D. S., Mat-Sharif, K. A., Lai, M. H., Lim, K. S., Tamchek, N., Omar, N. Y. M., ... Ahmad, H. (2016). Thermal Activation of Regenerated Grating in Hydrogenated Gallosilicate Fiber. *IEEE Sensors Journal*, 16(6), 1659–1664. <https://doi.org/10.1109/JSEN.2015.2503438>
- Guo, Y., Liu, W., Li, X., Kuang, Y., Wu, H., & Liu, H. (2018). Fiber Bragg Grating Displacement Sensor with High Abrasion Resistance for a Steel Spring Floating Slab Damping Track. *Sensors*, 18(6), 1899. <https://doi.org/http://dx.doi.org/10.3390/s18061899>
- Gysling, D. L., & Bostick, F. X. T. (2002). Changing Paradigms in Oil and Gas Reservoir Monitoring - The Introduction and Commercialization of In-Well Optical Sensing Systems. In *15th Optical Fiber Sensors Conference Technical Digest*. (pp. 43–46). Portland, OR, USA, USA: IEEE. <https://doi.org/https://doi.org/10.1109/OFS.2002.1000498>
- Haddock, H. S., Shankar, P. M., & Mutharasan, R. (2003). Fabrication of biconical tapered optical fibers using hydrofluoric acid. *Materials Science and Engineering B: Solid-State Materials for Advanced Technology*, 97(1), 87–93. [https://doi.org/10.1016/S0921-5107\(02\)00434-8](https://doi.org/10.1016/S0921-5107(02)00434-8)

- Han, C., Ding, H., & Lv, F. (2014). Demonstration of a refractometric sensor based on an optical micro-fiber three-beam interferometer. *Scientific Reports*, 4, 1–7. <https://doi.org/10.1038/srep07504>
- Harun, S. W., Lim, K. S., Damanhuri, S. S. A., & Ahmad, H. (2011). Microfiber loop resonator based temperature sensor. *Journal of the European Optical Society: Rapid Publications*, 6, 11026. <https://doi.org/10.2971/jeos.2011.11026>
- Hatta, A. M., Semenova, Y., Wu, Q., & Farrell, G. (2010). Strain sensor based on a pair of single-mode-multimode-single-mode fiber structures in a ratiometric power measurement scheme. *Applied Optics*, 49(3), 536. <https://doi.org/10.1364/AO.49.000536>
- Hertz, E. C. M., Van Roijen, R., de Waard, P. J., Koumans, R. G. M. P., Van Stralen, M. J. N., & Verbeek, B. H. (1994). Reflection Properties of Multimode Interference Devices. *IEEE Photonics Technology Letters*, 6(6), 715–718. <https://doi.org/10.1109/68.300172>
- Huang, X., Li, X., Yang, J., Tao, C., Guo, X., Bao, H., ... Zhu, Y. (2017). An in-line Mach-Zehnder Interferometer Using Thin-core Fiber for Ammonia Gas Sensing with High Sensitivity. *Scientific Reports*, 7(February), 1–8. <https://doi.org/10.1038/srep44994>
- Ian, K. E. T., Arrell, G. E. F., Ang, X. I. W., Ang, W. E. Y., Ifan, Y., In, X., ... Ang, P. E. W. (2017). Strain sensor based on gourd-shaped single-mode-multimode-single-mode hybrid optical fibre structure. *Optics Express* 18885, 25(16), 2197–2199. <https://doi.org/10.1364/OE.25.018885>
- Irawati, N., Yusuf, N. A. M., Rahman, H. A., Yasin, M., Ahmad, H., & Harun, S. W. (2017). Potassium permanganate (KMnO<sub>4</sub>) sensing based on microfiber sensors. *Applied Optics*, 56(2), 224. <https://doi.org/10.1364/AO.56.000224>
- Irigoyen, M., Sánchez-Martin, J. A., Bernabeu, E., & Zamora, A. (2017). Tapered optical fiber sensor for chemical pollutants detection in seawater. *Measurement Science and Technology*, 28(4), 045802. <https://doi.org/10.1088/1361-6501/aa5dc5>
- Jasim, A. a., Harun, S. W., Arof, H., & Ahmad, H. (2012). Inline Microfiber Mach-Zehnder Interferometer for High Temperature Sensing. *IEEE Sensors Journal*, 13(2), 1–1. <https://doi.org/10.1109/JSEN.2012.2224106>
- Ji, W. Bin, Yap, S. H. K., Panwar, N., Zhang, L. L., Lin, B., Yong, K. T., ... Majid, M. B. A. (2016). Detection of low-concentration heavy metal ions using optical microfiber sensor. *Sensors and Actuators, B: Chemical*, 237, 142–149. <https://doi.org/10.1016/j.snb.2016.06.053>
- Jo, B. W., Lee, Y. S., Jo, J. H., & Khan, R. M. A. (2018). Computer vision-based bridge displacement measurements using rotation-invariant image processing technique. *Sustainability (Switzerland)*, 10(6). <https://doi.org/10.3390/su10061785>

- Khijwania, S. K., & Gupta, B. D. (1999). Fiber optic evanescent field absorption sensor: effect of fiber parameters and geometry of the probe. *Optical and Quantum Electronics*, 31(8), 625–636. <https://doi.org/10.1023/A:1006956824722>
- Ko, J. M., & Ni, Y. Q. (2005). Technology developments in structural health monitoring of large-scale bridges. *Engineering Structures*, 27(12 SPEC. ISS.), 1715–1725. <https://doi.org/10.1016/j.engstruct.2005.02.021>
- Kou, J.-L., Ding, M., Feng, J., Lu, Y.-Q., Xu, F., & Brambilla, G. (2012). Microfiber-Based Bragg Gratings for Sensing Applications: A Review. *Sensors*, 12(12), 8861–8876. <https://doi.org/10.3390/s120708861>
- Kumar, A., & Kumar, N. (2018). Simultaneous measurement of current and temperature by using an all-fiber interferometric cost-effective and non-destructive sensing scheme. *Optik - International Journal for Light and Electron Optics* 171, 171(February), 1–8. <https://doi.org/10.1016/j.ijleo.2018.05.134>
- Lakshmi, B. B., Patrissi, C. J., & Martin, C. R. (1997). Sol-Gel Template Synthesis of Semiconductor Oxide Micro- and Nanostructures. *Chemistry of Materials*, 9(11), 2544–2550. <https://doi.org/10.1021/cm970268y>
- Lee, B. (2003). Review of the present status of optical fiber sensors. *Optical Fiber Technology*, 9(2), 57–79. [https://doi.org/10.1016/S1068-5200\(02\)00527-8](https://doi.org/10.1016/S1068-5200(02)00527-8)
- Lee, B. H., Kim, Y. H., Park, K. S., Eom, J. B., Kim, M. J., Rho, B. S., & Choi, H. Y. (2012). Interferometric fiber optic sensors. *Sensors*, 12(3), 2467–2486. <https://doi.org/10.3390/s120302467>
- Lee, C. E., Gibler, W. N., Atkins, R. A., & Taylor, H. F. (1992). In-Line Fiber Fabry-Perot Interferometer with High-Reflectance Internal Mirrors. *Journal of Lightwave Technology*, 10(10), 1376–1379. <https://doi.org/10.1109/50.166779>
- Leng, J., & Asundi, A. (2003). Structural health monitoring of smart composite materials by using EFPI and FBG sensors. *Sensors and Actuators, A: Physical*, 103(3), 330–340. [https://doi.org/10.1016/S0924-4247\(02\)00429-6](https://doi.org/10.1016/S0924-4247(02)00429-6)
- Leung, A., Shankar, P. M., & Mutharasan, R. (2007). A review of fiber-optic biosensors. *Sensors and Actuators, B: Chemical*, 125(2), 688–703. <https://doi.org/10.1016/j.snb.2007.03.010>
- Li, B., Jiang, L., Wang, S., Mengmeng Wang, Q. C., & Yang, J. (2012). A new Mach-Zehnder interferometer in a thinned-cladding fiber fabricated by electric arc for high sensitivity refractive index sensing. *Optics and Lasers in Engineering*, 50(6), 829–832. <https://doi.org/10.1016/j.optlaseng.2012.01.024>

- Li, B., Jiang, L., Wang, S., Yang, J., Wang, M., & Chen, Q. (2012). High sensitivity MachZehnder interferometer sensors based on concatenated ultra-abrupt tapers on thinned fibers. *Optics and Laser Technology*, 44(3), 640–645. <https://doi.org/10.1016/j.optlastec.2011.09.013>
- Li, H.-N., Yi, T.-H., Ren, L., Li, D.-S., & Huo, L.-S. (2014). Reviews on innovations and applications in structural health monitoring for infrastructures. *Structural Monitoring and Maintenance*, 1(1), 1–45. <https://doi.org/10.12989/smm.2014.1.1.001>
- Li, H. N., Li, D. S., & Song, G. B. (2004). Recent applications of fiber optic sensors to health monitoring in civil engineering. *Engineering Structures*, 26(11), 1647–1657. <https://doi.org/10.1016/j.engstruct.2004.05.018>
- Lim, K. S., Harun, S. W., Arof, H., & Ahmad, H. (2012). Selected Topics on Optical Fiber Technology Edited. In D. M. Yasin (Ed.), *Fabrication and Applications of Microfiber, Selected Topics on Optical Fiber Technology* (pp. 474–506). InTech. <https://doi.org/http://dx.doi.org/10.5772/46845>
- Littlejohn, D., Lucas, D., & Han, L. (1999). Bent silica fiber evanescent absorption sensors for near-infrared spectroscopy. *Applied Spectroscopy*, 53(7), 845–849. <https://doi.org/10.1366/0003702991947423>
- Liu, Y., Zhao, D., Floreani, F., Zhang, L., & Bennion, I. (2002). Fiber grating type dependence of temperature and strain coefficients and application to simultaneous temperature and strain measurement. In *15th Optical Fiber Sensors Conference Technical Digest. OFS 2002* (pp. 83–86). Portland, OR, USA, USA: IEEE. <https://doi.org/https://doi.org/10.1109/OFS.2002.1000507>
- Lopez-higuera, Jose MiguelCobo, L. R., Incera, A. Q., & Cobo, A. (2011). Fiber Optic Sensors in Structural Health Monitoring. *Journal of Lightwave Technology*, 29(4), 587–608.
- Lou, J., Wang, Y., & Tong, L. (2014). Microfiber optical sensors: A review. *Sensors (Switzerland)*, 14(4), 5823–5844. <https://doi.org/10.3390/s140405823>
- Love, J. D. (1987). Spot size, adiabaticity and diffraction in tapered fibres. *Electronics Letters*, 23(19), 993. <https://doi.org/10.1049/el:19870697>
- Ma, G. M., Li, C. R., Mu, R. D., Jiang, J., & Luo, Y. T. (2014). Fiber bragg grating sensor for hydrogen detection in power transformers. *IEEE Transactions on Dielectrics and Electrical Insulation*, 21(1), 380–385. <https://doi.org/10.1109/TDEI.2013.004381>
- Machavaram, V. R., Badcock, R. A., & Fernando, G. F. (2007). Fabrication of intrinsic fibre Fabry-Perot sensors in silica fibres using hydrofluoric acid etching. *Sensors and Actuators, A: Physical*, 138(1), 248–260. <https://doi.org/10.1016/j.sna.2007.04.007>

- Malekzadeh, M., Gul, M., Kwon, I.-B., & Catbas, N. (2014). An integrated approach for structural health monitoring using an in-house built fiber optic system and non-parametric data analysis. *Smart Structures and Systems*, 14(5), 917–942. <https://doi.org/10.12989/sss.2014.14.5.917>
- Martin, A., Badcock, R., Nightingale, C., & Fernando, G. F. (1997). A novel optical fiber-based strain sensor. *IEEE Photonics Technology Letters*, 9(7), 982–984. <https://doi.org/10.1109/68.593373>
- Mehryar, L., & Esmaili, M. (2011). Honey & Honey Adulteration Detection : A Review. *International Congress on Engineering and Food 11th*, 1–6.
- Mehta, A., Mohammed, W., & Johnson, E. G. (2003). Multimode interference-based fiber-optic displacement sensor. *IEEE Photonics Technology Letters*, 15(8), 1129–1131. <https://doi.org/10.1109/LPT.2003.815338>
- Metje, N., Chapman, D. N., Rogers, C. D. F., Henderson, P., & Beth, M. (2008). An Optical Fiber Sensor System for Remote Displacement Monitoring of Structures -- Prototype Tests in the Laboratory. *Structural Health Monitoring*, 7(1), 51–63. <https://doi.org/10.1177/1475921707081972>
- Miao, Z., Xu, D., Ouyang, J., Guo, G., Zhao, X., & Tang, Y. (2002). Electrochemically Induced Sol–Gel Preparation of Single-Crystalline TiO<sub>2</sub> Nanowires. *Nano Letters*, 2(7), 717–720.
- Mignani, A. G., Falciai, R., & Ciaccheri, L. (1998). Evanescent wave absorption spectroscopy by means of bi-tapered multimode optical fibers. *Applied Spectroscopy*, 52(4), 546–551. Retrieved from <http://www.scopus.com/inward/record.url?eid=2-s2.0-0032048482&partnerID=40&md5=db2dba731604d3cad5190910351a515a>
- Minakuchi, S., Takeda, N., Takeda, S. I., Nagao, Y., Franceschetti, A., & Liu, X. (2011). Life cycle monitoring of large-scale CFRP VARTM structure by fiber-optic-based distributed sensing. *Composites Part A: Applied Science and Manufacturing*, 42(6), 669–676. <https://doi.org/10.1016/j.compositesa.2011.02.006>
- Mita, A. (1999). Emerging Needs in Japan for Health Monitoring Technologies in Civil and Building Structures. In *2nd International Journal on Structural Health Monitoring* (pp. 1–12).
- Moar, P. N., Huntington, S. T., Katsifolis, J., Cahill, L. W., Roberts, A., & Nugent, K. A. (1999). Fabrication, modeling, and direct evanescent field measurement of tapered optical fiber sensors. *Journal of Applied Physics*, 85(7), 3395–3398. <https://doi.org/10.1063/1.369695>
- Mohammed, W. S., Mehta, A., & Johnson, E. G. (2004a). Wavelength tunable fiber lens based on multimode interference. *Journal of Lightwave Technology*, 22(2), 469–477. <https://doi.org/10.1109/JLT.2004.824379>

- Mohammed, W. S., Mehta, A., & Johnson, E. G. (2004b). Wavelength Tunable Fiber Lens Based on Multimode Interference. *Journal of Lightwave Technology*, 22(2), 469–477.
- Mohammed, W. S., Mehta, A., & Johnson, E. G. (2004c). Wavelength Tunable Fiber Lens Based on Multimode Interference. *J. Lightwave Technol.*, 22(2), 469. Retrieved from <http://jlt.osa.org/abstract.cfm?URI=jlt-22-2-469>
- Mohammed, W. S., Smith, P. W. E., & Gu, X. (2006). All-fiber multimode interference bandpass filter. *Optics Letters*, 31(17), 2547–2549. <https://doi.org/10.1364/OL.31.002547>
- Morales, A. M., & Lieber, C. M. (1998). A Laser Ablation Method for the Synthesis of Crystalline Semiconductor Nanowires. *Science (New York, N.Y.)*, 279(5348), 208. <https://doi.org/10.1126/science.279.5348.208>
- Mosavi Khandan Haghighi, A. A. (2010). *Vibration-based Damage Detection and Health Monitoring of Bridges*. North Carolina State University.
- Muhammad, M. Z., Jasim, A. A., Ahmad, H., Arof, H., & Harun, S. W. (2013a). Non-adiabatic silica microfiber for strain and temperature sensors. *Sensors and Actuators, A: Physical*, 192, 130–132. <https://doi.org/10.1016/j.sna.2012.12.036>
- Muhammad, M. Z., Jasim, A. A., Ahmad, H., Arof, H., & Harun, S. W. (2013b). Non-adiabatic silica microfiber for strain and temperature sensors. *Sensors and Actuators, A: Physical*, 192, 130–132. <https://doi.org/10.1016/j.sna.2012.12.036>
- N.Hida, N.Bidin, M.Abdullah, & M.Yasin. (2013). Fiber optic displacement sensor for honey purity detection in distilled water. *Optoelectronics and Advanced Materials – Rapid Communication*, 7(July-August), 565–568.
- Nosenzo, G., Whelan, B. E., Brunton, M., Kay, D., & Buys, H. (2013). Continuous monitoring of mining induced strain in a road pavement using fiber Bragg grating sensors. *Photonic Sensors*, 3(2), 144–158. <https://doi.org/10.1007/s13320-012-0077-0>
- O’Connell, H., & Dexter, R. J. (2001). Response and Analysis of Steel TRusses for Fatigue Truck Loading. *Journal Bridge Engineering*, 6(6), 628–638.
- O’Keeffe, S., Fitzpatrick, C., & Lewis, E. (2007). An optical fibre based ultra violet and visible absorption spectroscopy system for ozone concentration monitoring. *Sensors and Actuators, B: Chemical*, 125(2), 372–378. <https://doi.org/10.1016/j.snb.2007.02.023>

- Oliveira, R., Osório, J. H., Aristilde, S., Bilro, L., Nogueira, R. N., & Cordeiro, C. M. B. (2016). Simultaneous measurement of strain, temperature and refractive index based on multimode interference, fiber tapering and fiber Bragg gratings. *Measurement Science and Technology*, 27(7), 075107. <https://doi.org/10.1088/0957-0233/27/7/075107>
- Othonos, A., & Kalli, K. (1999). *Fiber Bragg gratings: fundamentals and applications in telecommunications and sensing*. Boston (Mass.): Artech house. Retrieved from <http://lib.ugent.be/catalog/rug01:000800781>
- Pack, D., March, I., & Lvdt, T. (1997). Linear variable differential transformer displacement transducers Data Sheet (LVDTs) and instrumentation. RS Components, PO Box 99, Corby, Northants, NN17 9RS.
- Paian, M. R., & Macdonald, R. I. (1997). Design of phased-array wavelength division multiplexers using multimode interference couplers. *Applied Optics*, 36(21), 5097–5108. <https://doi.org/10.1364/AO.36.005097>
- Pal, S. S., Mondal, S. K., Tiwari, U., Swamy, P. V. G., Kumar, M., Singh, N., ... Kapur, P. (2011). Etched multimode microfiber knot-type loop interferometer refractive index sensor. *Review of Scientific Instruments*, 82(9). <https://doi.org/10.1063/1.3633955>
- Pandey, N. K., & Yadav, B. C. (2006). Embedded fibre optic microbend sensor for measurement of high pressure and crack detection. *Sensors and Actuators, A: Physical*, 128(1), 33–36. <https://doi.org/10.1016/j.sna.2006.01.010>
- Perry, M., Yan, Z., Sun, Z., Zhang, L., Niewczas, P., & Johnston, M. (2014). High stress monitoring of prestressing tendons in nuclear concrete vessels using fibre-optic sensors. *Nuclear Engineering and Design*, 268, 35–40. <https://doi.org/10.1016/j.nucengdes.2013.12.038>
- Rahman, B. M. a., Somasiri, N., Themistos, C., & Grattan, K. T. V. (2001). Design of optical polarization splitters in a single-section deeply etched MMI waveguide. *Applied Physics B*, 73(5), 613–618. <https://doi.org/10.1007/s003400100680>
- Rao, Y.-J., Deng, M., Duan, D.-W., Yang, X.-C., Zhu, T., & Cheng, G.-H. (2007). Micro Fabry-Perot interferometers in silica fibers machined by femtosecond laser. *Optics Express*, 15(21), 14123–14128. <https://doi.org/10.1364/OE.15.014123>
- Rao, Y. J. (2007). In-line fiber-optic etalon formed by hollow-core photonic crystal fiber. *2007 Asia Optical Fiber Communication and Optoelectronic Exposition and Conference, AOE, 1*, 124–126. <https://doi.org/10.1109/AOE.2007.4410725>
- Rao, Y. J., Deng, M., Duan, D. W., & Zhu, T. (2008). In-line fiber Fabry-Perot refractive-index tip sensor based on endlessly photonic crystal fiber. *Sensors and Actuators, A: Physical*, 148(1), 33–38. <https://doi.org/10.1016/j.sna.2008.06.030>

- Reiner, M. . (2017). Elasticity Beyond the Elastic Limit. *American Journal of Mathematics*, 70(2), 433–446.
- Rivero, P. J., Goicoechea, J., & Arregui, F. J. (2018). Optical fiber sensors based on polymeric sensitive coatings. *Polymers*, 10(3), 1–26. <https://doi.org/10.3390/polym10030280>
- Roriz, P., Frazão, O., Lobo-Ribeiro, A. B., Santos, J. L., & Simões, J. A. (2013). Review of fiber-optic pressure sensors for biomedical and biomechanical applications. *Journal of Biomedical Optics*, 18(5), 050903. <https://doi.org/10.1117/1.JBO.18.5.050903>
- Ruiz-Pérez, V. I., Basurto-Pensado, M. A., LiKamWa, P., Sánchez-Mondragón, J. J., & May-Arrijoja, D. A. (2011a). Fiber optic pressure sensor using multimode interference. *Journal of Physics: Conference Series*, 274(1), 0–7. <https://doi.org/10.1088/1742-6596/274/1/012025>
- Ruiz-Pérez, V. I., Basurto-Pensado, M. A., LiKamWa, P., Sánchez-Mondragón, J. J., & May-Arrijoja, D. A. (2011b). Fiber Optic Pressure Sensor using Multimode Interference. *Journal of Physics: Conference Series*, 274, 012025. <https://doi.org/10.1088/1742-6596/274/1/012025>
- S. W. Doebling C. R. Farrar M. B. Prime. (1998). A Review of Damage Identification Methods that Examine Changes in Dynamic Properties. *The Shock and Vibration Digest*, 30(March), 91–105.
- Schermer, R. T., & Cole, J. H. (2007). Improved bend loss formula verified for optical fiber by simulation and experiment. *IEEE Journal of Quantum Electronics*, 43(10), 899–909. <https://doi.org/10.1109/JQE.2007.903364>
- Shao, M., Qiao, X., Fu, H., Li, H., Jia, Z., & Zhou, H. (2014). Refractive Index sensing of STMS fiber structure based Mach-Zehnder Interferometer, 26(5), 437–439.
- Silva, S., Frazao, O., Santos, J. L., & Malcata, F. X. (2012). A reflective optical fiber refractometer based on multimode interference. *Sensors and Actuators, B: Chemical*, 161(1), 88–92. <https://doi.org/10.1016/j.snb.2011.09.045>
- Silva, S., Pachon, E. G. P., Franco, M. A. R., Hayashi, J. G., Malcata, F. X., Frazão, O., ... Cordeiro, C. M. B. (2012). Ultrahigh-sensitivity temperature fiber sensor based on multimode interference. *Applied Optics*, 51(16), 3236–3242. <https://doi.org/10.1364/AO.51.003236>
- Sivakesava, S., & Irudayaraj, J. (2001). A rapid spectroscopic technique for determining honey adulteration with corn syrup. *Journal of Food Science*, 66(6), 787–792. <https://doi.org/10.1111/j.1365-2621.2001.tb15173.x>

- Smietana, M., Brabant, D., Bock, W. J., Mikulic, P., & Eftimov, T. (2012). Refractive-Index Sensing With Inline Core-Cladding Intermodal Interferometer Based on Silicon Nitride Nano-Coated Photonic Crystal Fiber. *Journal of Lightwave Technology*, 30(8), 1185–1189. <https://doi.org/10.1109/JLT.2011.2175201>
- Soga, K., & Luo, L. (2018). Distributed fiber optics sensors for civil engineering infrastructure sensing. *Journal of Structural Integrity and Maintenance*, 3(1), 1–21. <https://doi.org/10.1080/24705314.2018.1426138>
- Sohn, H., Farrar, C. R., Hemez, F. M., & Czarnecki, J. J. (2004). *A Review of Structural Health Monitoring Literature : 1996-2001*. Los Alamos, New Mexico: Los Alamos National Laboratory (Vol. LA-13976-M). <https://doi.org/LA-13976-MS>
- Soldano, L. B., & Pennings, E. C. M. (1995). Optical Multi-Mode Interference Devices Based on Self-Imaging: Principles and Applications. *Journal of Lightwave Technology*, 13(4), 615–627. <https://doi.org/10.1109/50.372474>
- Sulaiman Wadi Harun et al. (2016). *Fibre Optic Technologies and Techniques - Research Collection* (Vol. 798). InTech Janeza Trdine 9, 51000 Rijeka, Croatia.
- Sumetsky, M. (2004). Optical fiber microcoil resonator. *Optics Express*, 12(10), 2303–2316. <https://doi.org/10.1364/opex.12.002303>
- Sung, Y. C., Lin, T. K., Chiu, Y. T., Chang, K. C., Chen, K. L., & Chang, C. C. (2016). A bridge safety monitoring system for prestressed composite box-girder bridges with corrugated steel webs based on in-situ loading experiments and a long-term monitoring database. *Engineering Structures*, 126, 571–585. <https://doi.org/10.1016/j.engstruct.2016.08.006>
- Talataisong, W., Ismaeel, R., & Brambilla, G. (2018). A review of microfiber-based temperature sensors. *Sensors (Switzerland)*, 18(2). <https://doi.org/10.3390/s18020461>
- Tan, Y., Sun, L.-P., Jin, L., Li, J., & Guan, B.-O. (2013). Microfiber Mach-Zehnder interferometer based on long period grating for sensing applications. *Optics Express*, 21(1), 154–64. <https://doi.org/10.1364/OE.21.000154>
- Tennyson, R. C., Coroy, T., Duck, G., Manuelpillai, G., Mulvihill, P., Cooper, D. J. F., ... Jalali, S. J. (2000). Fibre optic sensors in civil engineering structures. *Canadian Journal of Civil Engineering*, 27(5), 880–889. <https://doi.org/10.1139/cjce-27-5-880>
- Tong, L. (2010). Brief introduction to optical microfibers and nanofibers. *Frontiers of Optoelectronics in China*, 3(1), 54–60. <https://doi.org/10.1007/s12200-009-0073-1>
- Tong, L., Gattass, R. R., Ashcom, J. B., He, S., Lou, J., Shen, M., ... Mazur, E. (2003). Subwavelength-diameter silica wires for low-loss optical wave guiding. *Nature*, 426(6968), 816–819. <https://doi.org/10.1038/nature02193>

- Tong, L., Hu, L., Zhang, J., Qiu, J., Yang, Q., Lou, J., ... Ye, Z. (2006). Photonic nanowires directly drawn from bulk glasses. *Optics Express*, 14(1), 82–87. <https://doi.org/10.1364/OPEX.14.000082>
- Tong, L., Lou, J., Ye, Z., Svacha, G. T., & Mazur, E. (2005). Self-modulated taper drawing of silica nanowires. *Nanotechnology*, 16(9), 1445–1448. <https://doi.org/10.1088/0957-4484/16/9/004>
- Tong, L., & Sumetsky, M. (2011). *Subwavelength and nanometer diameter optical fibers*. Springer US.
- Torres, B., Payá-Zaforteza Ignacio, I., Calderón, P. A., & Adam, J. M. (2011). Analysis of the strain transfer in a new FBG sensor for Structural Health Monitoring. *Engineering Structures*, 33(2), 539–548. <https://doi.org/10.1016/j.engstruct.2010.11.012>
- Tripathi, S. M., Kumar, A., Varshney, R. K., Kumar, Y. B. P., Marin, E., & Meunier, J. P. (2009). Strain and temperature sensing characteristics of single-mode-multimode-single-mode structures. *Journal of Lightwave Technology*, 27(13), 2348–2356. <https://doi.org/10.1109/JLT.2008.2008820>
- Udd, E., Black, K., Schulz, W., Kreger, S., Kunzler, M., & Heider, D. (2002). In-Situ Evaluation of Composite Structural Performance in Presence of High Stress/Strain Gradients Using Multi-axis Fiber Grating Strain Sensors. In *15th Optical Fiber Sensors Conference Technical Digest. OFS 2002*. Portland, OR, USA, USA: IEEE. <https://doi.org/https://doi.org/10.1109/OFS.2002.1000501>
- Ukil, A., Braendle, H., & Krippner, P. (2012). Distributed temperature sensing: Review of technology and applications. *Ieee Sensors Journal*, 12(5), 885–892. <https://doi.org/10.1109/JSEN.2011.2162060>
- Venkatesan, V. N., & Ramalingam, R. (2017). Numerical and experimental investigation of FBG strain response at cryogenic temperatures. In *IOP Conf. Series: Materials Science and Engineering* (Vol. 171, pp. 1–10). <https://doi.org/10.1088/1742-6596/755/1/011001>
- W. Housner, G., A. Bergman, L., K. Caughey, T., G. Chassiakos, A., O. Claus, R., Masri, S., ... T. P. Yao, J. (1997). Structural Control: Past, Present, and Future. *Journal of Engineering Mechanics-Asce - J ENG MECH-ASCE*, 123.
- W.Schofield, & M.Breach. (2007). *Engineering Surveying* (6th ed.). Oxford,UK: Elsevier Ltd.
- Wang, P., Zhao, H., Wang, X., Farrell, G., & Brambilla, G. (2018). A Review of Multimode Interference in Tapered Optical Fibers and Related Applications. *Sensors*, 18(3), 858. <https://doi.org/10.3390/s18030858>

- Wang, Q., & Farrell, G. (2006a). All-fiber multimode-interference-based refractometer sensor: proposal and design. *Optics Letters*, 31(3), 317–319. <https://doi.org/10.1364/OL.31.000317>
- Wang, Q., & Farrell, G. (2006b). Multimode-Fiber-Based Edge Filter for Optical Wavelength Measurement Application and Its Design. *Microwave and Optical Technology Letters*, 48(5), 900–902. <https://doi.org/10.1002/mop>
- Wang, Q., Farrell, G., & Yan, W. (2008). Investigation on single-mode-multimode-single-mode fiber structure. *Journal of Lightwave Technology*, 26(5), 512–519. <https://doi.org/10.1109/JLT.2007.915205>
- Wang, Q. W. Q., Farrell, G., & Yan, W. Y. W. (2008). Investigation on Single-Mode-Multimode Single-Mode Fiber Structure. *Journal of Lightwave Technology*, 26(5), 512–519. <https://doi.org/10.1109/JLT.2007.915205>
- Watanabe, M., Fujiki, H., & Mukai, S. (1994). Quantum Electronics Letters. ... *Electronics*, 48(4), 443–446. Retrieved from [http://staff.aist.go.jp/oguram/List/Bistability\\_Watanabe.pdf](http://staff.aist.go.jp/oguram/List/Bistability_Watanabe.pdf)
- Wei, T., Han, Y., Li, Y., Tsai, H.-L., & Xiao, H. (2008). Temperature-insensitive miniaturized fiber inline Fabry-Perot interferometer for highly sensitive refractive index measurement. *Optics Express*, 16(8), 5764. <https://doi.org/10.1364/OE.16.005764>
- Westwater, J. (1997). Growth of silicon nanowires via gold/silane vapor–liquid–solid reaction. *Journal of Vacuum Science & Technology B: Microelectronics and Nanometer Structures*, 15(3), 554. <https://doi.org/10.1116/1.589291>
- Willsch, R., Ecke, W., & Bartelt, H. (2002). Optical fiber grating sensor networks and their application in electric power facilities, aerospace and geotechnical engineering. *15th Optical Fiber Sensors Conference Technical Digest.*, 1, 49–54. <https://doi.org/10.1109/OFS.2002.1000499>
- Wo, J., Sun, Q., Liu, H., Li, X., Zhang, J., Liu, D., & Shum, P. P. (2013). Sensitivity-enhanced fiber optic temperature sensor with strain response suppression. *Optical Fiber Technology*, 19(4), 289–292. <https://doi.org/10.1016/j.yofte.2013.03.001>
- Wolfbeis, O. S., & Wang, X.-D. (2000). Fiber-optic chemical sensors and biosensors. *Analytical Chemistry*, 85(2), 81–89. <https://doi.org/10.1021/ac303159b>
- Wu, Q., Muhammad Hatta, A., Semenova, Y., & Farrell, G. (2009). Use of a single-multiple-single-mode fiber filter for interrogating fiber Bragg grating strain sensors with dynamic temperature compensation. *Applied Optics*, 48(29), 5451–5458. <https://doi.org/10.1364/AO.48.005451>

- Wu, Q., Semenova, Y., Hatta, A. M., Wang, P., & Farrell, G. (2010). Bent SMS fibre structure for temperature measurement. *Electronics Letters*, 46(16), 1129. <https://doi.org/10.1049/el.2010.1769>
- Wu, Q., Semenova, Y., Wang, P., & Farrell, G. (2011a). High sensitivity SMS fiber structure based refractometer – analysis and experiment, *19(9)*, 5451–5458.
- Wu, Q., Semenova, Y., Wang, P., & Farrell, G. (2011b). High sensitivity SMS fiber structure based refractometer – analysis and experiment. *Optics Express*, 19(9), 7937. <https://doi.org/10.1364/OE.19.007937>
- Wu, Q., Semenova, Y., Wang, P., Hatta, A. M., & Farrell, G. (2011). Experimental demonstration of a simple displacement sensor based on a bent single-mode-multimode-single-mode fiber structure. *Measurement Science and Technology*, 22(2). <https://doi.org/10.1088/0957-0233/22/2/025203>
- Wu, Q., Wang, P., Farrell, G., Wu, Q., Hatta, A. M., Wang, P., ... Farrell, G. (2010). Use of a Bent Single SMS Fiber Structure for Simultaneous Measurement of Displacement and Temperature Sensing Use of a Bent Single SMS Fiber Structure for Simultaneous Measurement of Displacement and Temperature Sensing, 23(2), 0–3.
- Wu, X., & Tong, L. (2013). Optical microfibers and nanofibers: A tutorial. *Nanophotonics*, 2(5–6), 407–428. <https://doi.org/10.1515/nanoph-2013-0033>
- Xiang, Y., Luo, Y., Li, Y., Li, Y., Yan, Z., Liu, D., & Sun, Q. (2018). Quasi-Distributed Dual-Parameter Optical Fiber Sensor Based on Cascaded Microfiber Fabry-Perot Interferometers. *IEEE Photonics Journal*, 10(2). <https://doi.org/10.1109/JPHOT.2018.2817573>
- Xie, W.-G., Zhang, Y.-N., Wang, P.-Z., & Wang, J.-Z. (2018). Optical Fiber Sensors Based on Fiber Ring Laser Demodulation Technology. *Sensors*, 18(2), 505. <https://doi.org/10.3390/s18020505>
- Xu, B., Li, Y., Sun, M., Zhang, Z.-W., Dong, X., Zhang, Z., & Jin, S. (2012). Acoustic vibration sensor based on nonadiabatic tapered fibers. *Optics Letters*, 37(22), 4768–70. <https://doi.org/10.1364/OL.37.004768>
- Xu, F., Chen, D., Peng, B., Xu, J., & Wu, G. (2012). All-fiber refractometer based on core mismatch structure. *Laser Physics*, 22(10), 1577–1580. <https://doi.org/10.1134/S1054660X12100271>
- Xu, F., Kou, J.-L., Luo, W., & Lu, Y. (2012). Surface-corrugated microfiber Bragg grating. *Optoelectronic Devices and Integration*, 8555, 855523. <https://doi.org/10.1117/12.999530>
- Xu, Y., Lu, P., Chen, L., & Bao, X. (2017). Recent Developments in Micro-Structured Fiber Optic Sensors. *Fibers*, 5(1), 3. <https://doi.org/10.3390/fib5010003>

- Xu, Z., Luo, Y., Liu, D., Shum, P. P., & Sun, Q. (2017). Sensitivity-controllable refractive index sensor based on reflective  $\theta$ -shaped microfiber resonator cooperated with Vernier effect. *Scientific Reports*, 7(1), 1–8. <https://doi.org/10.1038/s41598-017-10163-x>
- Yadav, T. K., Narayanaswamy, R., Abu Bakar, M. H., Kamil, Y. M., & Mahdi, M. A. (2014). Single mode tapered fiber-optic interferometer based refractive index sensor and its application to protein sensing. *Optics Express*, 22(19), 22802. <https://doi.org/10.1364/OE.22.022802>
- Yao, C., Bach, H.-G., Zhang, R., Zhou, G., Choi, J. H., Jiang, C., & Kunkel, R. (2012). An ultracompact multimode interference wavelength splitter employing asymmetrical multi-section structures. *Optics Express*, 20(16), 18248. <https://doi.org/10.1364/OE.20.018248>
- Yasin, M., Irawati, N., Isa, N. M., Harun, S. W., & Ahmad, F. (2018). MWCNTs coated silica microfiber sensor for detecting Mg<sup>2+</sup> in de-ionized water. *Optik*, 171(March), 65–70. <https://doi.org/10.1016/j.ijleo.2018.05.132>
- Yazdizadeh, Z., Marzouk, H., & Hadianfard, M. A. (2017). Monitoring of concrete shrinkage and creep using Fiber Bragg Grating sensors. *Construction and Building Materials*, 137, 505–512. <https://doi.org/10.1016/j.conbuildmat.2017.01.084>
- Ye, X. W., Su, Y. H., & Han, J. P. (2014). Structural Health Monitoring of Civil Infrastructure Using Optical Fiber Sensing Technology: A Comprehensive Review. *The Scientific World Journal*, 2014, 652329. <https://doi.org/10.1155/2014/652329>
- Yeom, D.-I., Mägi, E. C., Lamont, M. R. E., Roelens, M. A. F., Fu, L., & Eggleton, B. J. (2008). Low-threshold supercontinuum generation in highly nonlinear chalcogenide nanowires. *Optics Letters*, 33(7), 660. <https://doi.org/10.1364/OL.33.000660>
- Yin, B., Li, Y., Liu, Z. B., Feng, S., Bai, Y., Xu, Y., & Jian, S. (2016). Investigation on a compact in-line multimode-single-mode-multimode fiber structure. *Optics and Laser Technology*, 80, 16–21. <https://doi.org/10.1016/j.optlastec.2015.12.018>
- Zeng, X., Bao, X., Chhoa, C. Y., Bremner, T. W., Brown, A. W., DeMerchant, M. D., ... Georgiades, A. V. (2002). Strain measurement in a concrete beam by use of the Brillouin-scattering-based distributed fiber sensor with single-mode fibers embedded in glass fiber reinforced polymer rods and bonded to steel reinforcing bars. *Applied Optics*, 41(24), 5105–5114. <https://doi.org/10.1364/AO.41.005105>
- Zhang, Y., Tian, X., Xue, L., Zhang, Q., Yang, L., & Zhu, B. (2013). Super-high sensitivity of fiber temperature sensor based on leaky-mode bent SMS structure. *IEEE Photonics Technology Letters*, 25(6), 560–563. <https://doi.org/10.1109/LPT.2013.2245644>

- Zhang, Y., Zhang, Q., Li, Y., Wang, N., & Zhu, J. (2000). Coating of carbon nanotubes with tungsten by physical vapor deposition. *Solid State Communications*, 115(1), 51–55. [https://doi.org/10.1016/S0038-1098\(00\)00125-3](https://doi.org/10.1016/S0038-1098(00)00125-3)
- Zhang, Y., Zhou, A., Qin, B., Deng, H., Liu, Z., Yang, J., & Yuan, L. (2014). Refractive Index Sensing Characteristics of Single-Mode Fiber-Based Modal Interferometers. *Journal of Lightwave Technology*, 32(9), 1734–1740.
- Zhao, J. R., Huang, X. G., He, W. X., & Chen, J. H. (2010). High-resolution and temperature-insensitive fiber optic refractive index sensor based on fresnel reflection modulated by Fabry-Perot interference. *Journal of Lightwave Technology*, 28(19), 2799–2803. <https://doi.org/10.1109/JLT.2010.2065215>
- Zhao, Y., Jin, Y., Liang, H., & Dong, X. (2011). All-Fiber-Optic Sensor for Relative Humidity Measurement V2-84. In *2011 International Conference on Electronics and Optoelectronics (ICEOE 2011) All-Fiber-Optic* (pp. 83–86).
- Zhao, Y., Li, X. G., Meng, F. C., & Zhao, Z. (2014). A vibration-sensing system based on SMS fiber structure. *Sensors and Actuators, A: Physical*, 214, 163–167. <https://doi.org/10.1016/j.sna.2014.04.044>
- Zhu, T., Wu, D., Liu, M., & Duan, D. W. (2012). In-line fiber optic interferometric sensors in single-mode fibers. *Sensors (Switzerland)*, 12(8), 10430–10449. <https://doi.org/10.3390/s120810430>
- Zibaii, M. I., Latifi, H., Karami, M., Gholami, M., Hosseini, S. M., & Ghezelayagh, M. H. (2010). Non-adiabatic tapered optical fiber sensor for measuring the interaction between  $\alpha$ -amino acids in aqueous carbohydrate solution. *Measurement Science and Technology*, 21(10), 105801. <https://doi.org/10.1088/0957-0233/21/10/105801>
- Zulkifli, A. Z., Masnan, S. E. F., Azmi, N. M., Akib, S. M., Arof, H., & Harun, S. W. (2016). A simple load sensor based on a bent single-mode-multimode-single-mode fiber structure. *Sensors and Actuators, A: Physical*, 242, 106–110. <https://doi.org/10.1016/j.sna.2016.02.025>